1-1-2016

Experimental-Computational Analysis of Woodpeckers' Beaks/ Hyoid Apparatus for Damping of Stress Waves

Na Yeon Lee

Experimental-computational analysis of woodpeckers' beaks/hyoid apparatus for damping of stress waves

By

Na Yeon Lee

A Dissertation
Submitted to the Faculty of
Mississippi State University
in Partial Fulfillment of the Requirements
for the Degree of Doctor of Philosophy
in Biological Engineering
in the Department of Agricultural and Biological Engineering

Mississippi State, Mississippi

August 2016

Experimental-computational analysis of woodpeckers' beaks/hyoid apparatus for damping of stress waves

By

Na Yeon Lee

Approved:

Lakiehsa N. Williams
(Major Professor)

Mark F. Horstemeyer
(Co-Major Professor)

Hongjoo Rhee
(Committee Member)

Jun Liao
(Committee Member)

Rajkumar Prabhu
(Committee Member)

Fei Yu
(Graduate Coordinator)

Jason Keith
Dean
Bagley College of Engineering

Name: Na Yeon Lee

Date of Degree: August 12, 2016

Institution: Mississippi State University

Major Field: Biological Engineering

Major Professors: Dr. Lakiesha N. Williams, Dr. Mark F. Horstemeyer

Title of Study: Experimental-computational analysis of woodpeckers' beaks/hyoid apparatus for damping of stress waves

Pages in Study 100

Candidate for Degree of Doctor of Philosophy

This dissertation proposes engineering principles for stress wave dissipation found in woodpeckers. From the experimental study of a woodpecker's beaks via electron microscopy and mechanical testing, the three main design factors were pointed out. First, a woodpecker's beak has wavy lines inside of the beak for local shearing. The waviness of wavy lines found in the woodpecker's beaks was 1 while chicken's was 0.3, and toucan's was 0.05. Second, the woodpecker showed elongated the keratin scales to the pecking direction with a dimension ratio of 3.67 (width/height) while chicken's and toucan's were 3 and 1, respectively. Third, a woodpecker's beak bone was less porous for structural strength. The porosity of a woodpecker's beak bone was about 9.9 % while chicken's and toucan's were 42.3 % and 61.5 %, respectively. Also, by using computational simulations, unique geometries including hyoid apparatus and suture interfaces found in woodpeckers were investigated to assess their damping capabilities. Surrounding a woodpecker's head, the hyoid apparatus composed of core cartilage and muscle encasing a core cartilage. The spiral and thinning geometry of the hyoid apparatus converted the normal waves into shear waves. Then shear waves generated lateral

displacement of the hyoid bone, and lateral displacement brought strain energy into surrounding muscle, in which energy loss occurred by viscoelastic behavior of the muscle. Quantitatively, as the stress wave traveled from the anterior to the posterior end of the hyoid apparatus, its pressure decreased 75 % and the impulse decreased 84 %. Suture interfaces, which is another unique feature observed from woodpecker's beak, was investigated for their geometrical effects on the dynamic impact mitigation. A sinusoidal pattern of suture interfaces induced wave scattering at its boundary causing conversion of longitudinal waves into shear waves. The suture gap also brought pressure decay by storing strain energy in its viscoelastic material. As a result, a bar with a suture interface attenuated stress waves about 37 % more than a bar with a flat interface. Based on the results and ideas presented herein, one can develop bio-inspired material for energy absorbing.

DEDICATION

I want to express my sincere gratitude and appreciation to Jesus Christ, who designed woodpeckers elegantly in engineering perspective to protect their head from repeated blast impact and allow me to discover His engineering ideas from woodpeckers.

ACKNOWLEDGEMENTS

I gratefully acknowledge all those who assisted me throughout this long journey. The person to whom I owe the most gratitude is Dr. Mark Horstemeyer and Dr. Lakiesha Willams. I am extremely fortunate to have been their student. Dr. Horstemeyer initiated me to pursue PhD in MSU and guided to equip as an individual researcher. He served not only as my academic advisor, but also as a role model of entire life. Dr. Williams encouraged me greatly and helped to find talent from inside of me. I am also appreciative of my committee members: Dr. Hongjoo Rhee, Dr. Raj Prabhu, and Dr. Jun Liao, each of whom provided encouraging and thought provoking discussion. Their advice and counsel greatly contributed to the completion of this work.

Also, I thankfully acknowledge the Center for Advanced Vehicular Systems (CAVS) to provide great work environment for mechanical experiments and running computational simulations by helps of staffs of Mr. Stephen Horstemeyer, Ms. Melissa Mott, Ms. Rose Mary Dill, and many others. Mason C. Cline supported the research greatly by helping experimental research.

Financial support from the Center for Advanced Vehicular Systems in Mississippi State University is gratefully acknowledged. This work was also supported by the Department of Energy and ERDC bio-inspired project. Also, I would like to acknowledge the Department of Agricultural and Biological Engineering for the financial support and the James Worth Bagley College of Engineering for the fellowship funding.

Last, but most I recognize my family: my parents, husband, and my son for their never-ending love and tremendous support. I wish to express my highest gratitude to my husband, Sungkwang Mun. Without him, I would not have made it this far. He is not only my emotional and spiritual supporter but also a great advisor for research. My son, Peter Banseok Mun, has brought new level of surprise and joyfulness into my life.

TABLE OF CONTENTS

LIST OF TABLES

LIST OF FIGURES

CHAPTER I

INTRODUCTION

1.1 Bio-inspired design material

Bio-inspired design, also called biomimetics or biomimicry, is the study of living species for the purpose of creating new engineering systems by copying species' unique traits. Compared to Biology that studies the genetics and molecular responses occurring in living creatures, bio-inspired design proposes new engineering ideas based on biological traits (1).

To date, several cases of bio-inspiration have been applied in many engineering fields such as chemical engineering, fluid dynamics, or aerodynamics. For example, a gecko's foot inspired researchers to use Vander-Walls interactions between two objects rather than chemical glue and motivated the manufacture of new types of adhesion (2-4). Also, a frog's foot inspired another new adhesion working even in watery environments (5, 6). The exterior shape of a box fish inspired the shape of a moving vehicle that resists air flow and greatly increased fuel efficiency (7, 8). In addition, mimicking the grooved shape of a humpback whale's flipper (*Megaptera novaeangliae*), researchers designed an air conditioning fan manufactured by LG that reduced energy consumption 10% and noise by 2dB (9). These are only a few examples of how Bio-inspiration is a promising field of study, though the field is still relatively young and largely unexploited.

In this study we have investigated biological material to aid developing novel materials and machine designs. Compared to man-made materials, biological materials have distinctive characteristics with significant complexities, hierarchical structures being most notable, and with suitably and efficiently designed functions. In particular, we observed several micro-structural characteristics in biological materials: fibrous, helical, gradient, layered, tubular, cellular, suture, and overlapping structures are a few of these characteristics (10). For example, a ram's horn has a complex hierarchical structure of keratin and bone, and it absorbs shock efficiently without causing an injury to the ram's head. In subscale, the keratin constituting of the ram's horn forms a tubular structure. This keratin is composed of fibrils that has a helical microstructure (11). Researchers found both the material properties and the geometry of the ram's horn are responsible for shock absorption (11). Turtle shells have a multiscale hierarchical structure. These sandwich composite structure consisting of keratin and bony material (12). The layered composite material of turtle shells absorbs energy better than any of the individual layers. These characteristics of biological materials can be applied to new materials to develop new armor or efficient energy absorbing materials.

1.2 Woodpecker

The focus of this study was to examine woodpeckers to inspire engineering ideas specifically for energy mitigation. Woodpeckers show amazingly efficient shock absorption without any recorded damage to their beaks or brains while pecking trees. When a woodpecker makes a blow into the tree trunk, its bill repeatedly strikes at a speed of 6~7 m/s, and the impact deceleration is on the order of 1000 g's (13). For the Pileated Woodpecker, the resulting deceleration impact force has been measured from 600 to

1500 g's while the deceleration impact in a survivable car crash rarely exceeds 100 g's. The Yellow-Bellied Sapsucker (a type of woodpecker) can strike 100 to 300 times per minute on a tree during excavating nest cavities, and they may spend many hours drilling for food or constructing cavities (14). In spite of the continuous shock, the woodpecker's beak remains intact by efficiently dissipating the impact energy.

Figure 1.1 Woodpecker head sample used for research.

The head of the Red-bellied woodpecker (*Melanerps calolinus*) used for the research. The length of the beak is about 3 - 3.5 cm, and that of the head is about 2.5 - 3 cm.

1.3 Anatomy of birds' beaks

Bird beaks are entire mouth structure of a bird. Although avian beaks vary in their shapes, colors, and sizes, they share common features. The bird's beaks have two bony projections. The upper part is called maxilla or upper mandible, and the lower part of bony projection is called lower mandible. Those bony parts are composed of trabecular bone, which is porous bone, and they are covered with a thin keratin layer known as the rhamphotheca.

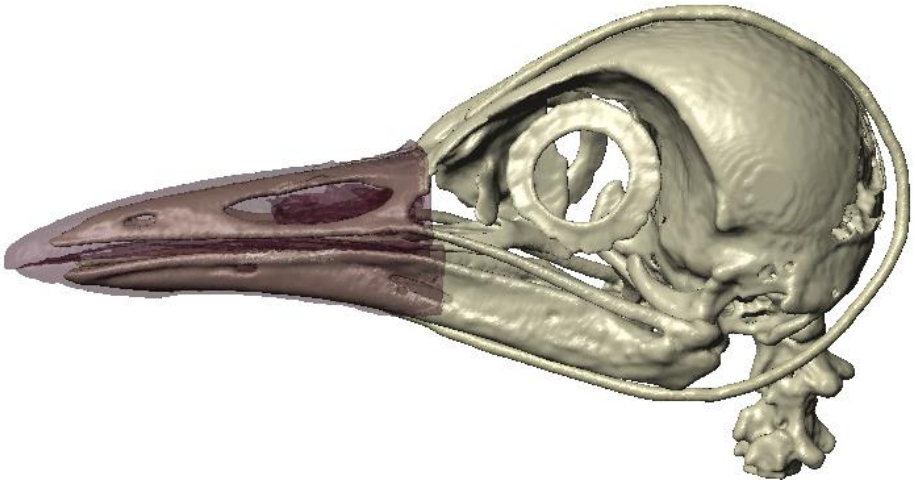

Figure 1.2 Woodpecker's head model.

Three-dimensional reconstructed woodpecker head model to show the bone structure(white) and rhamphotheca(brown) of the beak.

Figure 1.2 shows the bone structure of a woodpecker's head and beaks and rhamphotheca covering the beaks' bone. Compared to other species of birds, a woodpecker's beaks are straight and tapered to the tip. Generally, the color of woodpecker's beak is black.

1.4 Multiscale study for hierarchical architecture of a woodpecker's beaks

The concept of a multiscale study for metal or polymer can be applied to the research of woodpecker's beak. A study a multiple length scales allows for one to pick up essential information from one scale and bridge it to another upper scale in an effort to incorporate the role of microstructure in the mechanical response of the full structure. Figure 1.3 shows the multiscale research of a woodpecker's beak. One is able to quantify elasticity at the electronic or atomistic scale and bridge that information to nanoscale. At nanoscale, the anisotropiy of beaks' keratin due to fiber arrangement can be quantified, and at microscale the wavy structure could be assessed. At the mesoscale, the damage

and crack propagation in a beak could be investigated. Finally, all the information can be incorporated into a model the woodpecker's beak. Thus, this is our motivation for this experimental study. The hierarchical nature of biological material will be incorporated into a full woodpecker head-beak complex using a multiscale scheme.

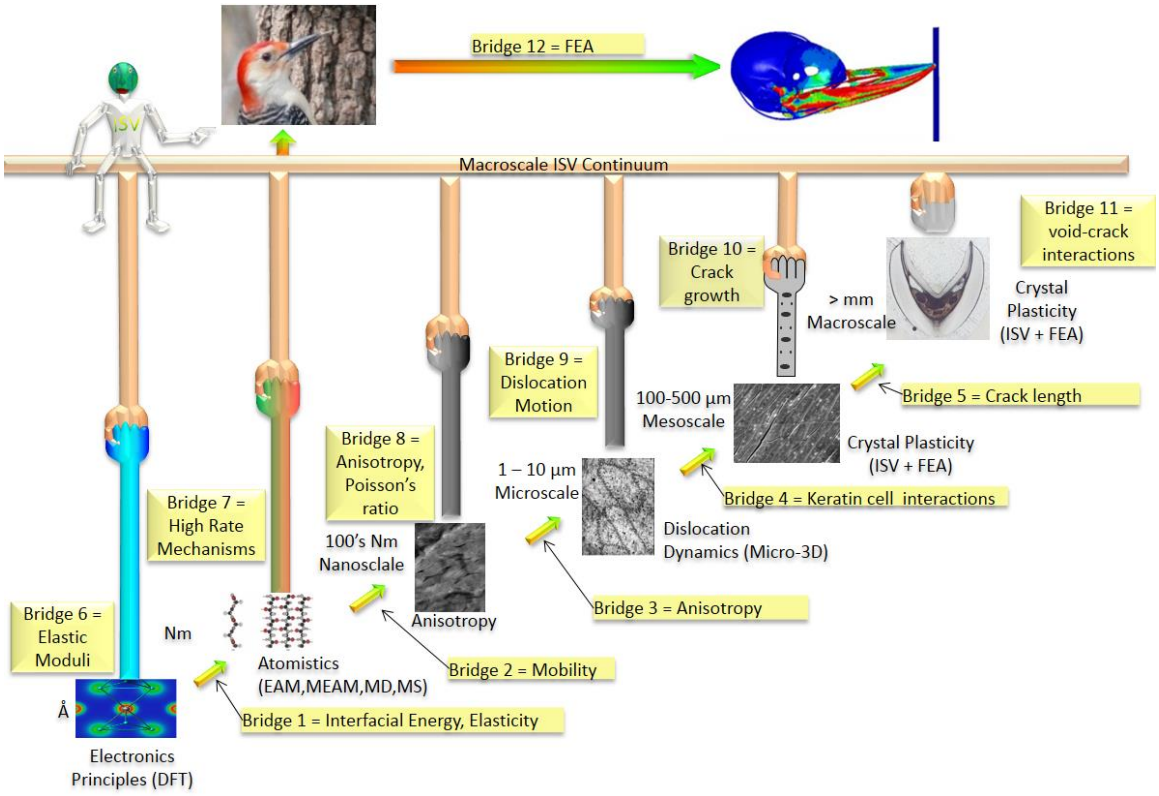

Figure 1.3 Multiscale study of keratin from a woodpecker's beaks

The multiscale diagram shows that one can pick up essential information from each scale and bridge to the next length scale.

1.5 Dissertation overview

Three separate studies were completed to learn new engineering principles inspired by woodpeckers. In Study 1, the structure-property relationships of the beak of Red-bellied woodpeckers in multiscale were studied. The beaks were observed using an

optical microscope, SEM (scanning electron microscope), and TEM (transmission electron microscope), and then mechanical tests were carried out. Compared to other birds' beaks such as toucans and chickens, woodpeckers' beaks have three engineering principles that allow for dissipation of energy: (1) elongated keratin scales, (2) wavy suture lines, and (3) a less porous innermost layer. In Study 2, a hyoid bone, one of the woodpecker's unique features, were analyzed for its damping capacity using ABAQUS/Explicit 6.14 (15). The spiral and thinning structure of the hyoid bone transferred the compressional and longitudinal impact to the shear stress wave, and eventually the shear stresses induced the displacement in a lateral direction. The lateral displacement led to much greater strain energy of the adjacent muscle so that the hyoid bone reduced the impulse of the initial impact by about 84%. In Study 3, suture interfaces were examined for its energy absorbing capacity. Stress waves mitigated through two mechanisms in the structure containing suture lines. First, wave scattering occurred at a sinusoidal patterned boundary, in which compressive longitudinal stress waves converted into flexural and shear stress waves. Second, the viscoelastic suture gap stored strain energy so that energy loss occurred. Additionally, a 3D model of a woodpecker head was generated using micro-CT and software ScanIP (Simpleware Ltd, United Kingdom). Finally, the mesh of the whole head of the woodpecker was then imported into Abaqus/Explicit to simulate a real pecking situation and to investigate shock mitigation occurring across the whole engineering system.

1.6 References

1. Whitesides GM. Bioinspiration: something for everyone. Interface Focus. 2015;5(4):20150031.

2. Geim A, Grigorieva SVDIV, Novoselov K, Zhukov A, Shapoval SY. Microfabricated adhesive mimicking gecko foot-hair. Nature Materials. 2003;2(7):461-3.

3. Sitti M, Fearing RS. Synthetic gecko foot-hair micro/nano-structures as dry adhesives. Journal of Adhesion Science and Technology. 2003;17(8):1055-73.

4. Autumn K, Liang YA, Hsieh ST, Zesch W, Chan WP, Kenny TW, et al. Adhesive force of a single gecko foot-hair. Nature. 2000;405(6787):681-5.

5. Drotlef DM, Appel E, Peisker H, Dening K, del Campo A, Gorb SN, et al. Morphological studies of the toe pads of the rock frog, Staurois parvus (family: Ranidae) and their relevance to the development of new biomimetically inspired reversible adhesives. Interface focus. 2015;5(1):20140036.

6. Federle W, Barnes W, Baumgartner W, Drechsler P, Smith J. Wet but not slippery: boundary friction in tree frog adhesive toe pads. Journal of the Royal Society Interface. 2006;3(10):689-97.

7. Bartol IK, Gharib M, Webb PW, Weihs D, Gordon MS. Body-induced vortical flows: a common mechanism for self-corrective trimming control in boxfishes. Journal of Experimental Biology. 2005;208(2):327-44.

8. Gordon MS, Hove JR, Webb PW, Weihs D. Boxfishes as Unusually Well-Controlled Autonomous Underwater Vehicles*. Physiological and Biochemical Zoology. 2000;73(6):663-71.

9. Choi H, Park H, Sagong W. Biomimetic flow control based on morphological features of living creatures a). Physics of Fluids (1994-present). 2012;24(12):121302.

10. Naleway SE, Porter MM, McKittrick J, Meyers MA. Structural Design Elements in Biological Materials: Application to Bioinspiration. Advanced Materials. 2015;27(37):5455-76.

11. Trim MW, Horstemeyer MF, Rhee H, El Kadiri H, Williams LN, Liao J, et al. The effects of water and microstructure on the mechanical properties of bighorn sheep (Ovis canadensis) horn keratin. Acta Biomaterialia. 2011;7(3):1228-40.

12. Rhee H, Horstemeyer M, Hwang Y, Lim H, El Kadiri H, Trim W. A study on the structure and mechanical behavior of the Terrapene carolina carapace: A pathway to design bio-inspired synthetic composites. Materials Science and Engineering: C. 2009;29(8):2333-9.

13. May PRA, Fuster JM, Haber J, Hirschman A. Woodpecker drilling behavior. An endorsement of the rotational theory of impact brain injury. Archives of neurology. 1979;36(6):370.

14. Backhouse F. Woodpeckers of North America: Firefly Books Ltd; 2005.

15. Simulia D. ABAQUS 6.11 Analysis User's Manual. Abaqus 611 Documentation. 2011:22.2.

CHAPTER II

HIERARCHICAL MULTISCALE STRUCTURE-PROPERTY RELATIONSHIPS OF THE RED-BELLIED WOODPECKER (MELANERPES CAROLINUS) BEAK

2.1 Introduction

Woodpeckers show amazingly efficient shock absorption capabilities without any recorded damage to their beaks or brains while pecking trees. When a woodpecker makes a blow into the tree trunk, its beak repeatedly strikes at a speed of 6~7 m/s, and the impact deceleration is on the order of 1000 g's (1). The Yellow-Bellied Sapsucker (a type of woodpecker) can strike 100 to 300 times per minute on the tree, and they may spend many hours pecking for food or constructing cavities (2). The woodpecker's capability of withstanding high impact has been studied by several researchers. Unique anatomical features of woodpeckers have been reported such as stiff tail feathers to resist gravity for working on vertical trees, wider ribs to relieve neck stress, zygodactyl feet to climb trees, and an ocular system to protect their eyes (2-6). The physical characteristics of the head include spongy bone on the upper beak, an extended hyoid bone, a tightly enclosed small brain within the skull, and a plate-like high strength cranial bone (7-11). Also, numerical studies of the woodpecker's head reported by Wang et al., and Zhu et al. showed that the cranial bone and beak play an important role in energy dissipation (12-14). Yoon et al. used physiological arguments from woodpeckers to develop shock absorbers for micro devices, which can resist high-frequency excitation and high-g forces by absorbing

energy (15, 16). Some additional examples of specific biomimetic applications include employment of spiral and wavy structures found in nature, and possibly utilizing the woodpecker's geometrical advantages in car bumpers and athletic helmets (17).

Although some physiological and numerical studies have been conducted on woodpeckers, many studies have not focused on woodpeckers' beaks from the perspective as a biological material. Avian beaks are structural biocomposite materials. Generally, structural biological materials comprise a brittle mineral and ductile protein interacting in a complex structure that is organized in a hierarchical manner (18-20). Likewise, birds' beaks are mainly composed of β-keratin layer, which is called the rhamphotheca, bony core, and cellular interface between rhamphotheca and bony core (21-24). At the microscale, the rhamphotheca comprises keratin scales with a diameter of approximately 50 μm with the core part of the beak being a closed-cell trabecular-like bone (25-28). At the nanoscale level, keratin scales comprise β–keratin filaments and have a small gap between them (26). For the multiscale mechanical properties, the Young's modulus of the rhamphotheca was reported as ~1 GPa for toucans and hornbills with its anisotropy depending on the geometry of the keratin scales (26). Under compression, the stress plateau occurs at 0.3 MPa for the toucan beak and at 2 MPa for the hornbill beak (26). At the microscale, the reported value of microhardness for the rhamphotheca was ~200 MPa for the toucan, hornbill, and European starling (26, 29). Contrary to the rhamphotheca layer, the core part of the beak had a wide range of microhardness values with respect to the species; 0.27 GPa for toucan beak and 0.39 GPa for hornbill beaks (26). Seki et al. (26) also reported the nanohardness of the toucan beaks were 0.5 GPa and 0.55 GPa for the rhamphotheca and the foam trabecular,

respectively. The nanohardness of the hornbill beaks were 0.85 GPa and 0.94 GPa for the rhamphotheca and the trabecular, respectively (Table 2.1). Also, the elastic moduli of the woodpecker, toucan, hornbill, and Java finch are represented in Table 1. The elastic moduli of the beaks of woodpeckers, toucans, and hornbills were obtained from the nanoindentation testing while the result of that of Java finch was obtained from a double indentation technique. The different mechanical properties of the birds reveal different functions and uses of each beak.

Table 2.1 Summary of the micro/nano hardness and elastic modulus of beaks of birds for comparison

	Microhardness (GPa)		Nanohardness (GPa)	
	Rhamphotheca	Bony layer	Rhamphotheca	Bony layer
Woodpecker	0.32 ± 0.01	0.64 ± 0.07	0.40 ± 0.08	1.16 ± 0.19
Toucan	0.22 ± 0.012	0.27 ± 0.03	0.5 ± 0.06	0.55 ± 0.12
Hornbill	0.21 ± 0.015	0.39 ± 0.014	0.85 ± 0.27	0.94 ± 0.21

Woodpecker (n=6), toucan (26), hornbill (26), and Java finch (41).

Our study focuses on the multiscale structure-property relationships of the woodpeckers' beaks. By studying woodpeckers' beaks, we can learn clues in solving human engineering problems related to energy absorption and shock mitigation.

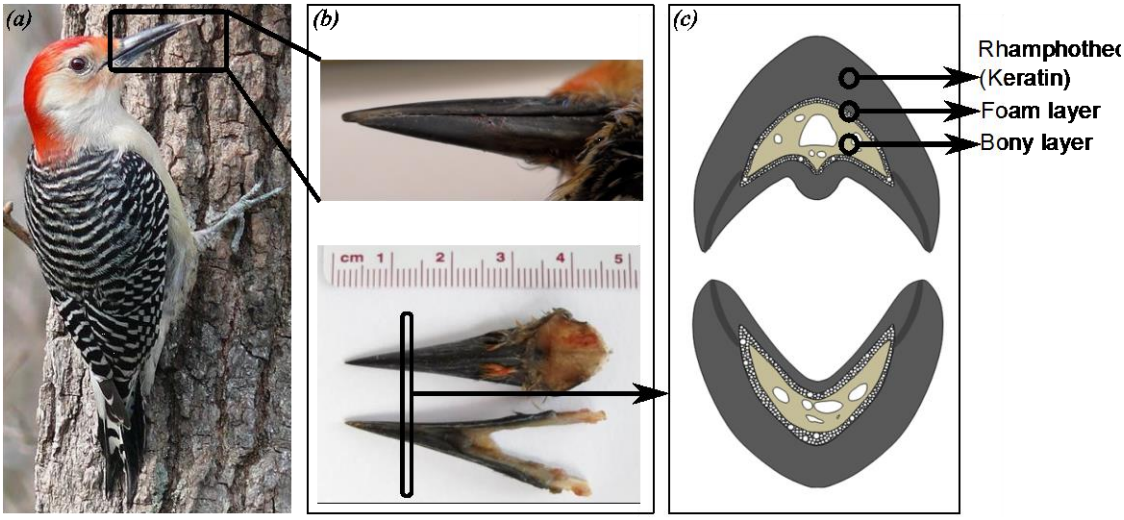

Figure 2.1 Overview of the woodpecker's beak.

(a) A male Red-Bellied Woodpecker, (b) upper and lower beaks of the woodpecker, and (c) a schematic of the cross-sectional view of the woodpecker beak comprising three layers; outer rhamphotheca, middle foam, and inner bony layers.

2.2 Materials and methods

The beak of an adult Red-Bellied Woodpecker (*Melanerpes carolinus*), which is a medium sized bird living in the southern United States, was studied using various microscopy techniques and mechanical testing methods. One non-living Red-Bellied Woodpecker was obtained from the Department of Wildlife, Fisheries and Aquaculture (Mississippi State University), and two others were obtained from road-kill. The woodpeckers obtained had body lengths of 24~25 cm. The upper and lower beaks were separated from the body as shown in Figure 2.1(b), and all tests were carried out at ambient conditions.

The structure of the woodpeckers' beaks was characterized by scanning electron microscopy (SEM) and transmission electron microscopy (TEM). In order to observe the polished cross-section of the beak, samples of the upper and lower beaks were cut into

four parts from the tip to the root with length of 5 mm using a diamond saw. Each sample was mounted into epoxy using a cold mount technique and then thoroughly polished. For preparing the fractured sample and TEM sample, the beaks were fixed in 2.5 % glutaraldehyde and post fixed in 2% osmium tetraoxide. Samples were then rinsed and dehydrated in a graded ethanol series. Following processing the upper beak microstructure was observed by preparing fractured surface samples using a cryo-fracture technique then sputter coating with gold palladium. SEM micrographs were taken using a JEOL JSM-6500F field emission gun (FEG)-SEM. The energy dispersive x-ray spectroscopy (EDS) on the FEG-SEM was also used to carry out chemical analysis of the beaks. In preparation for TEM, samples of the lower beak were taken from the beak, fixed, and then embedded in Spurr's resin. Thin sections (60~80 nm) were cut on a Reichert-Jung Ultra cut E ultramicrotome, and stained with uranyl acetate and lead citrate. Stained sections were examined by using a JEOL JEM-100CX II TEM at an acceleration voltage of 80 kV. The porosity and area fraction in the beak were measured via analysing two-dimensional images using Image J software (National Institutes of Health, Bethesda, MD).

Microindentation and nanoindentation tests were conducted on the lower beak in order to evaluate the mechanical properties. A Vickers hardness tester (LECO Corporation, St. Joseph, MI) with a pyramidal diamond tip was used to examine the beak's microhardness. The applied maximum load was 100 gram-force. Nanoindentation tests were carried out on the beaks mounted into epoxy by a Hysitron Triboindenter® with a Berkovich type diamond tip. The loading condition was controlled as follows: 9000 μN maximum load with a 20 s loading segment and a 40 s unloading segment. This

procedure was employed due to the creep behavior of viscoelastic materials. The hardness was defined by following Eq. (2.1):

$$H = \frac{P}{A} \tag{2.1}$$

where P is the maximum applied load [N], and A the resultant projected contact area. For a Berkovich tip, A is calculated from the ideal tip area function, 25.4h2, and h is the maximum displacement. The reduced elastic modulus was derived from the initial unloading contact stiffness (Eq. (2.2)),

$$S = \frac{dP}{dh} = \frac{2}{\pi} E_r \sqrt{A} \tag{2.2}$$

where the reduced modulus, Er, is derived from the displacement from both the specimen and the indenter. The reduced elastic modulus is given by:

$$\frac{1}{\mathrm{E_r}} = \frac{(1-\nu^2_{specimen})}{E_{specimen}} + \frac{(1-\nu^2_{indenter})}{E_{indenter}} \tag{2.3}$$

where E and ν are the elastic modulus and Poisson's ratio of the specimen and the indenter, respectively.

2.3 Results

2.3.1 Structure of the woodpecker beaks

2.3.1.1 Macrostructure

One of the notable characteristics of biological materials is the hierarchical structure (20). Woodpeckers' beaks also have a unique hierarchical structure from the macroscale down to nanoscale. At the macroscale, the full length of the beak is about 4 cm, and the cross-section of the woodpecker beak is composed of the outer rhamphotheca layer, the middle foam layer, and the inner bony layer as the schematic of Figure 2.1(c)

illustrates. The upper beak has a cavity in the centre of the beak, which decreases the weight while still keeping the bending resistance fairly high. The curvature of the tip of the upper beak was measured at 19.07 mm-1, and that of the lower beak was approximately 12.01 mm-1. The density of the upper beak was 1.1 g/cm3, and that of the lower beak was 1.348 g/cm3 measured using the Archimedes method (30). The lower density of the upper beak is due to the cavity and more porous area at the root part of the upper beak (2).

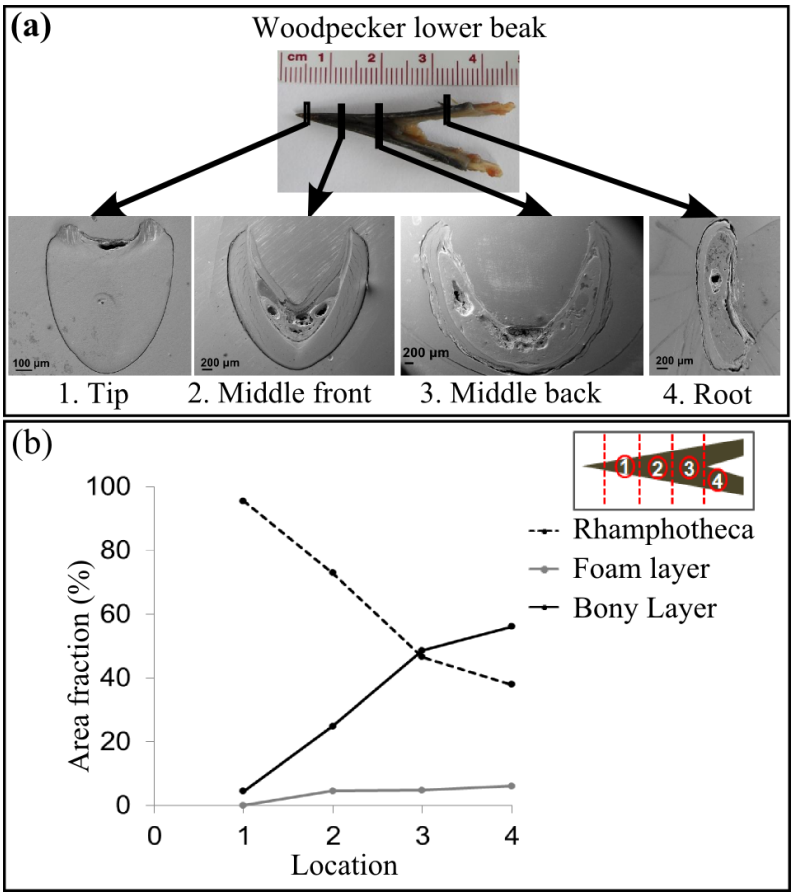

Figure 2.2 Cross-sectional area of the woodpecker's beaks.

(a) Cross-sectional views throughout the length of the woodpeckers' beaks taken by scanning electron microscope illustrating the change in the geometries with differing ratio of keratin and bone. (b) The area fraction of the rhamphotheca, the foam, and the bony layers along the length of the lower woodpeckers' beaks.

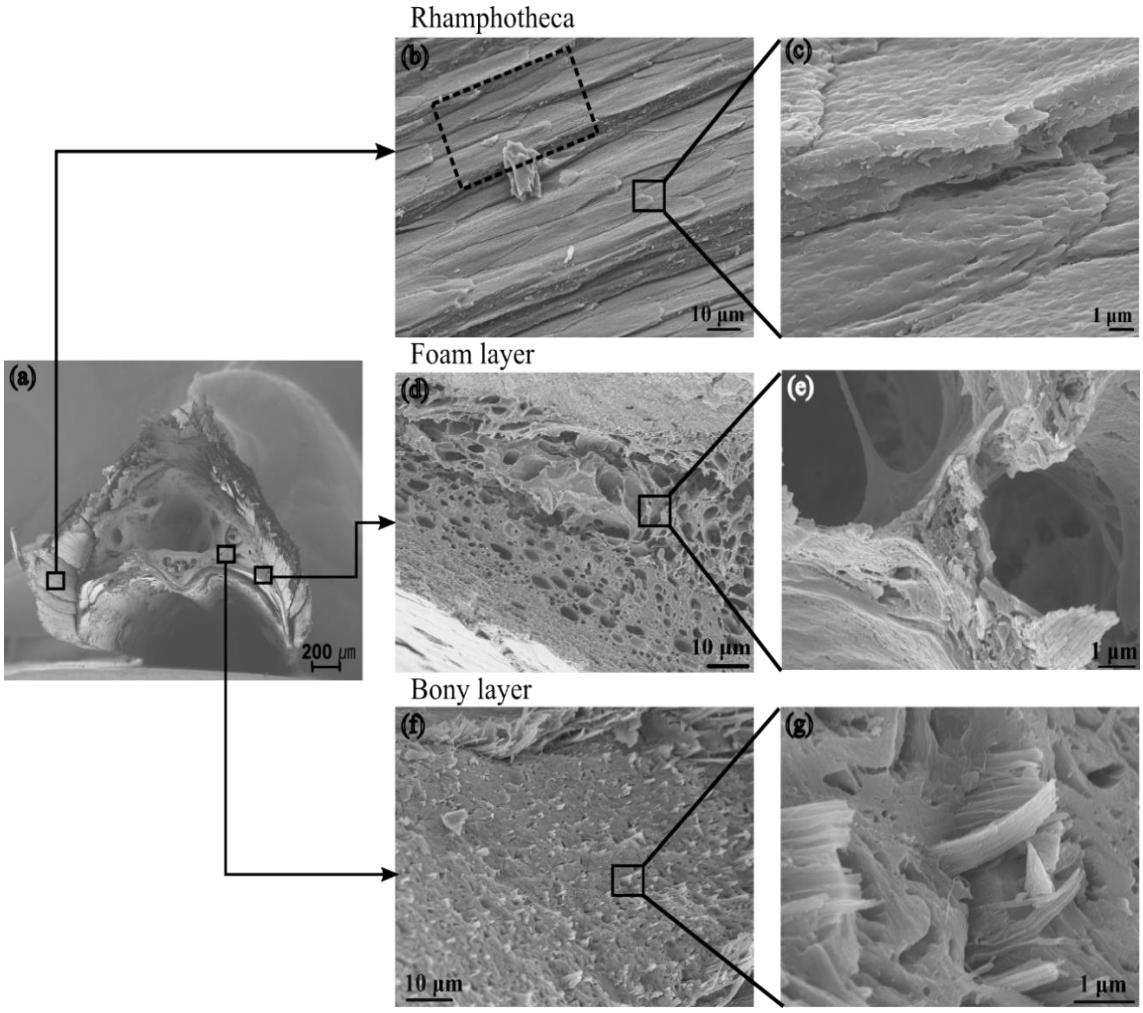

Figure 2.3 Microstructure of the woodpeckers' beaks

Microstructure of the woodpeckers' beaks garnered from scanning electron microscope showing (a) the fractured cross-section through the upper beak of the woodpecker with the three distinctive structural layers, (b) the outer rhamphotheca layer containing overlapping scale-like features indicated by the dotted box, (c) keratin scales showing the rough surface of the rhamphotheca, (d) the middle foam layer with a porous structure with a porosity of 30~65%, (e) the thickness of the cell wall is 0.1~2 μm, (f) the inner bony layer, and (g) bundles of the fibers in the matrix.

Figure 2.2(a) provides a series of cross-sectional views of the lower beak from the tip to the root. Along the beak, the geometry of the cross-section changed as well as the area fraction of each layer. Figure 2.2(b) shows that the area fraction of the rhamphotheca decreased while that of the bony part increased from the tip to the root of the beak.

2.3.1.2 Microstructure

The SEM images on the fractured surface of the woodpeckers' beaks reveal the microstructure of each layer (Figure 2.3). Figure 2.3(a) shows the entire fractured surface of the upper beak having a big cavity in the center. Figure 2.3(b) shows that the rhamphotheca layer has a thickness of 500 μm, consisting of overlapping scales. The size of the scales varies with respect to the location on the beak. At the ventral surface of the beak (mouth), the scales are more equiaxed and thicker with a dimension of 25 10 1 μm, whereas at the outside of beak the scales are more elongated and thinner with a dimension of 55 15 0.2 μm. Figure 2.3(c) shows the rough surface of the keratin scales.

The foam layer located between the rhamphotheca and the innermost bony layer is closed-cell type foam with a thickness of 100 μm and is graded between the rhamphotheca and bony layer. The foam layer is composed of dermis and epidermis. The dermis includes keratin filaments to provide mechanical resilience, and the epidermis includes dense bundles of collagen fibers to anchor to the inner bony layer (31, 32). Our results agree with literature as bundles of fibers were observed in the microscopic images of the woodpecker's beak. At the interface, which is particularly important due to high stresses and contact failure, the foam layer joins the dissimilar materials of keratin and bone. Figure 2.3(d) depicts the middle foam layer exhibiting a porous structure having the porosity of 27~30% near the rhamphotheca or the bony layer and 50~65% at the middle of the foam layer. At the contact region, the foam material provides flexibility. As shown in Figure 2.3(e), the thickness of the cell wall is 0.1~ 2 μm and the fibrils comprise the interior structure of the foam layer.

The bony layer located in the inner part of the beak has randomly distributed various-sized voids and a large cavity. Figure 2.3(f) shows that the bony layer of the woodpecker's beak is not spongy-like trabecular bone and also shows that the composite bony layer is comprised of fibers in the longitudinal direction, which is a common structure of bone (33).

2.3.1.3 Nanostructure

The nanostructure of each layer of woodpeckers' beaks was investigated by TEM. Cross-sectional and lateral perspective images in Figure 2.4 show the nanostructure of the rhamphotheca. The cross-sectional view revealed that the keratin scales are tightly packed (Figure 2.4(a)), and the size of the keratin grain varies from 10 to 15 μm across the diameter. By increasing the magnification, it is shown that the grain boundary has a wavy structure (Figure 2.4(b)). The waviness of the keratin grain boundary (i.e., the ratio of height to width) was calculated with the mean value being 1.0 ± 0.32. Also, Figure 2.4(c) shows that there is a narrow gap along the wavy line measured as 44.2 ± 19.2 nm. Figures. 4(d)-(f) depict the lateral views of the rhamphotheca. One can observe the side view of the keratin scales in Figure 2.4(d) and the boundary where two keratin scales meet in Figure 2.4(e). The fibers run parallel to the transverse orientation and zooming in on the contact surface of the two scales, Figure 2.4(f) shows the gap within the wavy line.

Figure 2.5, taken by SEM, shows the nanostructure of the foam layer. Figure 2.5(a) shows the cell wall of the foam layer, in which part of it is composed of fibers as shown in Figure 2.5(b). From the image of Figure 2.5(c), the length the D-period in the fibers was measured to be in the range of 60-70 nm. The measured period falls into the range of collagen fibril D-period although it is not the exact 67 - 69 nm band that is often

reported in soft connective tissues (34). The stereological effect might explain this variation of D-period estimation (e.g., a slight tilt can change the period estimation). The morphology of the banded fibers under SEM and the periodic length all point to the likelihood that the fibers contained in the foam layer are collagen fibers.

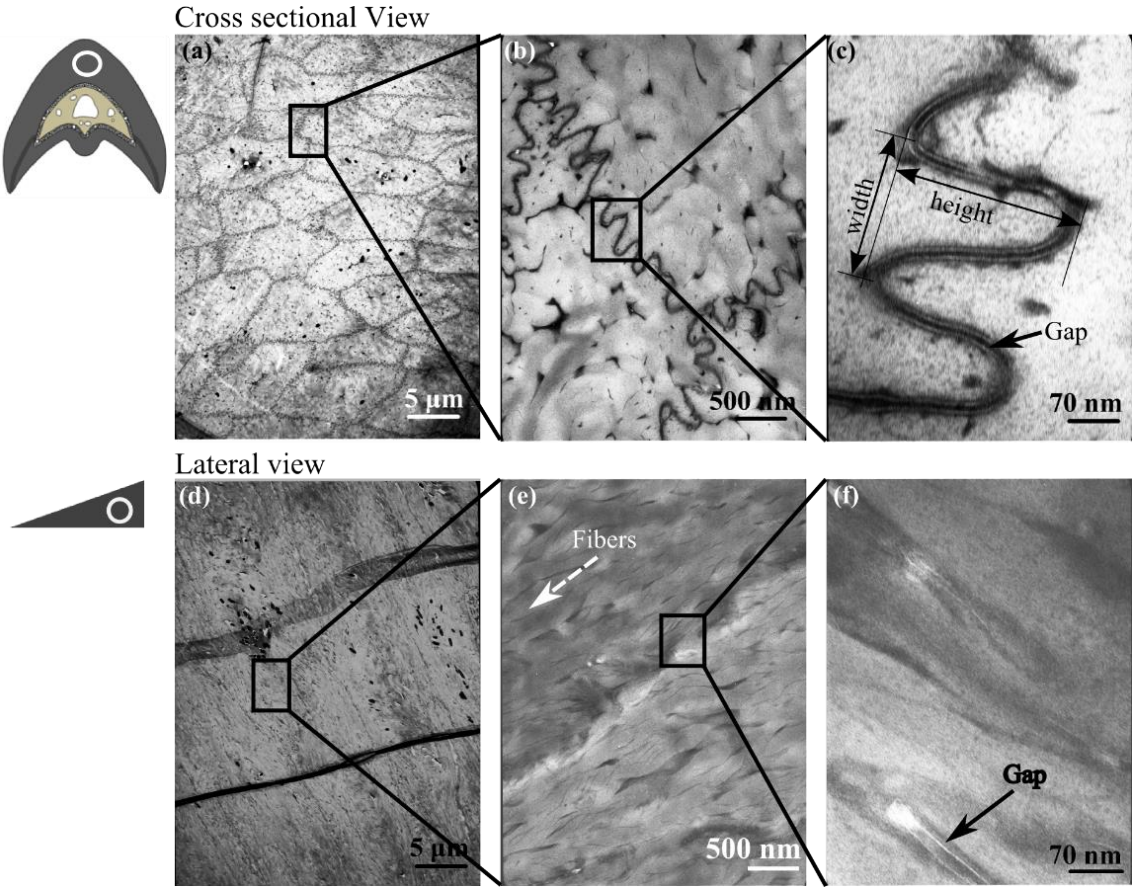

Figure 2.4 Transmission electron microscopic images on the rhamphotheca of woodpeckers' beaks shows the nanostructure

(a) A cross-sectional view reveals the keratin grains in the rhamphotheca; (b) a cross-sectional view that shows the wavy "suture" lines at the grain boundary; (c) a cross-sectional view that depicts a small gap in the wavy line; (d) a longitudinal view in the rhamphotheca; (e) a longitudinal view with the arrows indicating the running direction of the fiber; and (f) a longitudinal view showing the wavy line and gap.

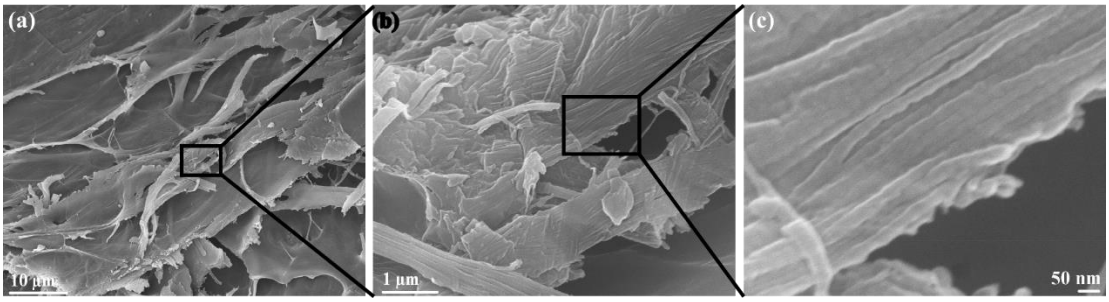

Figure 2.5 Nanostructure of the middle foam layer taken by scanning electron microscope.

(a) The cell walls of the foam layer, (b) the part of the cell wall is composed of fibers, and (c) the fiber have a D-period indicating that the fiber is collagen.

Figure 2.6, taken by TEM, shows the nanostructure of the bony layer. The bony layer contains round-shaped cells and fibers with an area fraction of the bone cells being approximately 37% (Figure 2.6(a)). Figure 2.6(b) shows that the running directions of the fibers are not uniform as both longitudinal (L1, L2) and the transverse (T) directions of the fibrils are observed within the same plane. Figure 2.6(c) shows the D-period of the fibers, which is an indication of collagen. The length of the D-period in Figure 2.6(c) ranged from 50~70 nm. From these different analyses, it is apparent that the core part of bird beak is bone, which consists of collagen and mineral.

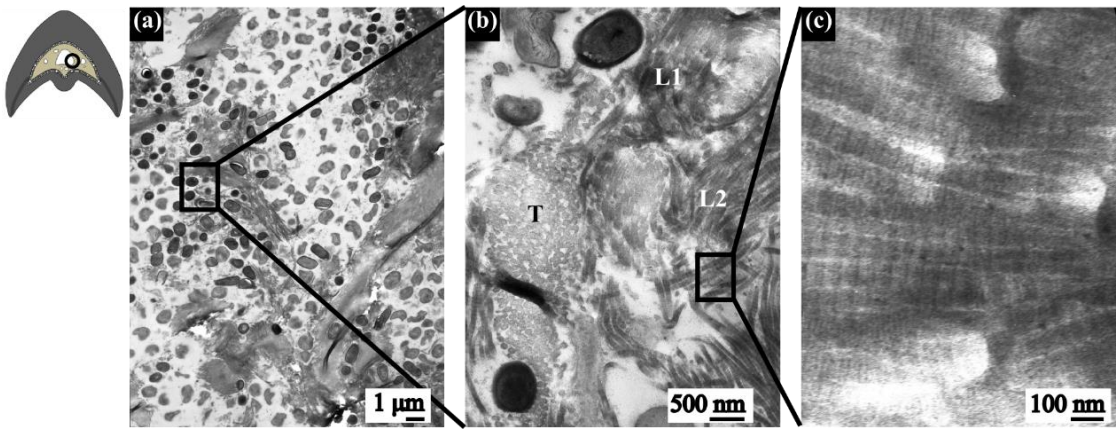

Figure 2.6 Images taken by transmission electron microscope illustrate the nanostructure of the bony layer of the woodpeckers' beaks.

(a) The distribution of the bone cells having round shapes and short fibrils (grey); (b) the fibrils are running in both longitudinal (L1, L2) and transverse directions (T); and (c) the fibers have a D-period that are indicative of collagen.

2.3.2 Chemical composition

The chemical composition of the rhamphotheca, foam, and bony layers were analyzed by the EDS technique. Figure 2.7(a) shows that the main constituents of the rhamphotheca are carbon (C), nitrogen (N), oxygen (O), and a small amount of sulfur (S), which are the main components of keratin in general. The chemical components of the foam layer are C, N, O, S, and a small amount of calcium (Ca) as shown in Figure 2.7(b). The chemical composition of the foam layer confirms that it is a graded material between the rhamphotheca and bony layer comprising protein and mineral. The chemical elements in the bony layer shown in Figure 2.7(c) are C, N, O, and various minerals such as Ca, sodium (Na), and magnesium (Mg), which are the main components of bone, thus, confirming the mineralized collagen fibers observed within the bony layer as shown in Figure 2.3(f).

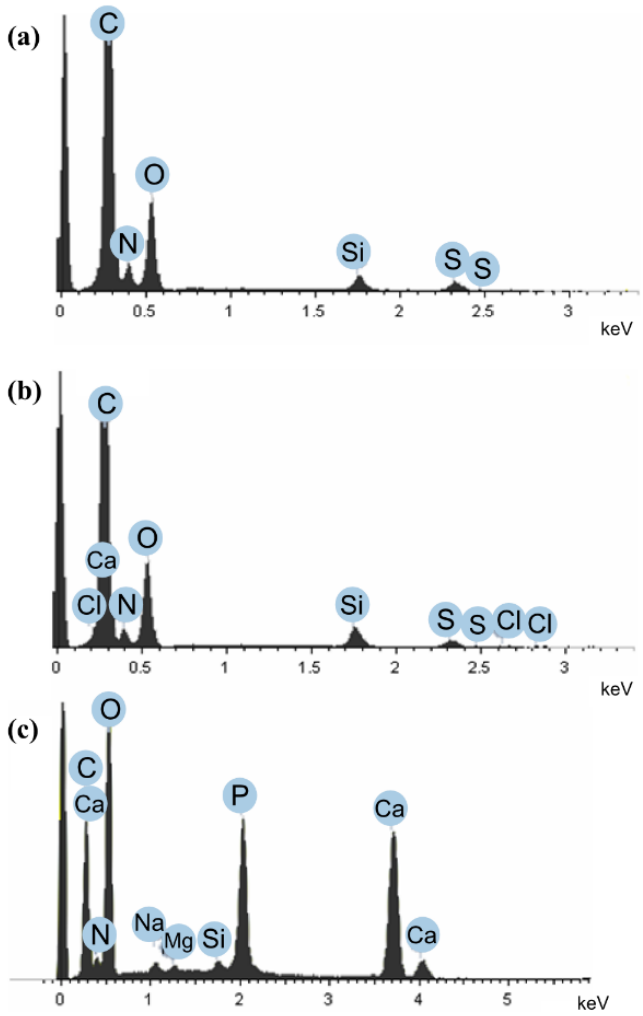

Figure 2.7 The results of Energy dispersive spectroscopy analysis.

(a) The outer rhamphotheca layer composed of carbon, nitrogen, oxygen, and sulfur; (b) middle foam layer composed of carbon, nitrogen, oxygen, sulfur, and calcium; and (c) inner bony layer composed of carbon, nitrogen, oxygen and several minerals such as calcium, sodium, magnesium, and phosphate.

2.3.3 Mechanical properties of the woodpecker beaks

The multiscale mechanical responses of the woodpeckers' beaks were also studied at the microscale and nanoscale under microindentation and nanoindentation tests, respectively.

Microindentation tests were performed to garner micromechanical properties. Indentation tests were conducted only on the rhamphotheca and bony layers, because the area of the foam layer was not large enough to conduct the tests. The average value of the microhardness was 0.32 ± 0.01 GPa for the rhamphotheca layer and 0.64 ± 0.07 GPa for the bony layer (Table 2.1).

The nanomechanical properties obtained from the nanoindentation tests were the nanohardness and the reduced elastic modulus. To examine the gradient of the nanomechanical properties, experiments were performed on four different beak locations from the tip to the root, and the results are depicted in Figure 2.8. The results show a decrease of the hardness as the location changes from the tip to the root of the beak for the rhamphotheca. The bony layer did not show a change with respect to location. The nanohardness was measured as 0.40 ± 0.08 GPa for the rhamphotheca, 0.24 ± 0.14 GPa for the foam layer, and 1.16 ± 0.19 GPa for the bony layer (Table 2.1). The relatively high mineral content of the bony layer was responsible for it being three times harder than the keratin part (rhamphotheca). The average measured values of reduced elastic moduli were 8.7 ± 1.1 GPa at the rhamphotheca, 6.5 ± 2.5 GPa at the foam layer, and 30.2 ± 3.6 GPa at the bony layer (Table 2.1).

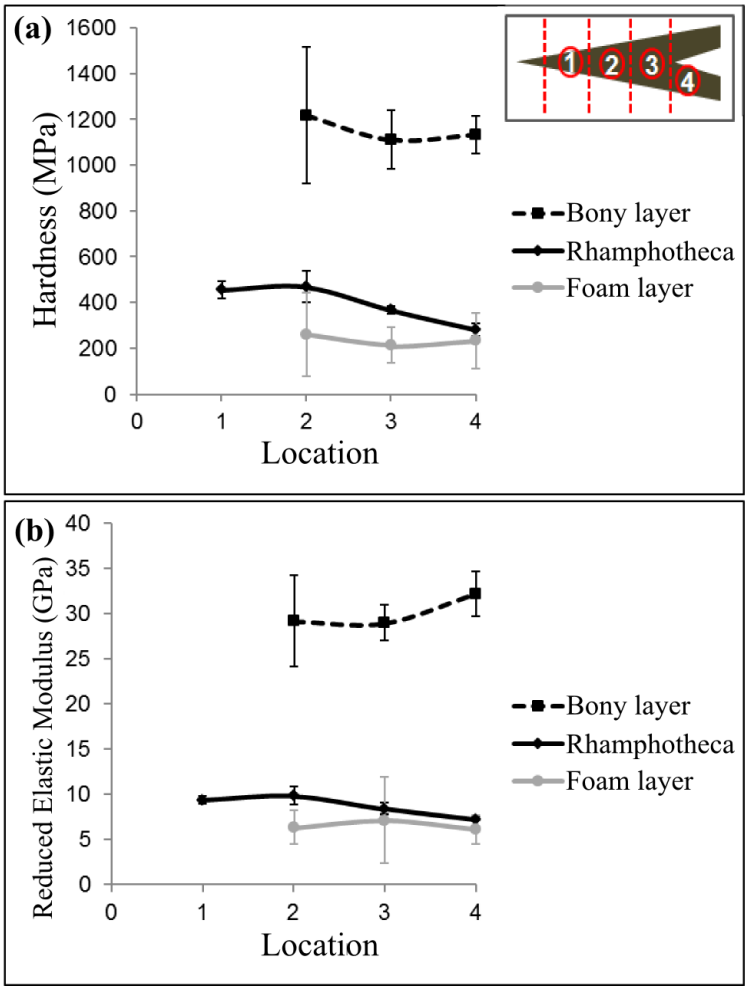

Figure 2.8 Nanomechanical properties of the rhamphotheca and bony layers obtained from nanoindentation tests.

(a) Nanohardness and (b) reduced elastic modulus.

2.4 Discussion

2.4.1 Macrostructure-mechanical property relations

The woodpeckers' beaks are functionally graded materials through the length of the beak from three perspectives: (1) the geometry of the cross-section of the beak changes as shown in Figure 2.2(a); (2) the area fractions of the rhamphotheca, foam, and bony portion change as shown in Figure 2.2(b); and (3) the associated mechanical

properties of the rhamphotheca, foam, and bony portion are different. According to the rule of mixtures, which was developed for composite materials and can be applied for layered materials, one can estimate the modulus and hardness at each point along the beak with the correlating area fractions and strength/hardness of each sample (Eq. (2.4) and Eq. (2.5)).

$$(E \cdot A)_{total} = (E \cdot A)_{rhamphothea} + (E \cdot A)_{foam} + (E \cdot A)_{bony} \quad (2.4)$$

$$(H \cdot A)_{total} = (H \cdot A)_{rhamphothea} + (H \cdot A)_{foam} + (H \cdot A)_{bony} \quad (2.5)$$

where A represents the area fraction, E represents elastic modulus, and H is the hardness value. The total strength of the composite increased from the beak tip to the root. This strength gradient arises because the modulus of the bony region (E_{bony}) was greater than that of the rhamphotheca region ($E_{rhamhotheca}$), and the area fraction of the bony layer increased from the beak tip to the root while the area fraction of the rhamphotheca decreased from the beak tip to the root. Table 2.2 organizes the geometrical, microstructural, and mechanical property information. With regard to the location on the beak, the geometry of the cross-section changes like similar to that of a shape of ∇ → V → U → ( ). The changed geometry of the cross-section results in a change in moment of inertia, and the changing moment of inertia allows for a changing flexural stiffness over the beak. Table 2.2 shows that the flexural stiffness from the tip to the root of the beak increases. This implies that the beak becomes stiffer and has a greater bending resistance when traversing from the tip to the root. Another important observation is that the overall aggregate modulus increases from the tip to the root according to the rule-of-mixtures. This not only increases the stiffness but also increases the speed of the stress wave, as the shock wave velocity is proportional to the modulus over the density.

Table 2.2 Summary of the structure-properties of the woodpeckers' beaks including area fraction, mechanical properties, aggregate modulus/hardness, and moment of inertia at each location along the beak.

Distance from the tip	Cross-section shape	Area (mm^2)	Rhampotheca (outer layer)				Foam (middle layer)			
			Area fraction (%)	Area (mm^2)	Hardness (MPa)	Modulus (GPa)	Area fraction (%)	Area (mm^2)	Hardness (MPa)	Modulus (GPa)
1	∇	0.47	95.5	0.4	457.5±38.1	9.4±0.4	0.0	0.0	-	-
2	V	12.4	72.9	9.0	470.2±68.9	9.9±1.0	3.9	0.4	262.2±12.1	6.4±1.9
3	U	27.1	46.5	12.6	396.4±34.3	8.4±0.4	4.8	1.3	215.6±76.0	7.1±4.8
4	I	24.5	37.9	9.3	284.0±27.8	7.3±0.5	6.0	1.5	234.9±12.3	6.1±1.6

Distance from the tip	Bone (inner layer)					Aggregate Hardness (MPa)	Aggregate Modulus (GPa)	I (mm^4)	Flexural Stiffness (GPa-mm^4)
	Area fraction (bone) (%)	Area fraction (void) (%)	Area (mm^2)	Hardness (MPa)	Modulus (GPa)				
1	0.0	4.5	0.0	-	-	436.9±36.4	9.0±0.4	0.0	0.18±0.01
2	7.1	16.1	2.9	1219.6±298.5	29.2±5.1	439.6±71.9	9.5±1.2	7.0	66.3±8.3
3	28.5	20.2	13.2	1111.5±128.0	29.0±2.0	511.4±56.1	12.5±1.0	42.0	527.2±40.9
4	40.5	15.6	13.7	1135.0±82.2	32.3±2.5	581.4±44.5	16.2±1.3	21.6	350.2±27.9

2.4.2 Microstructure-mechanical property relations

The microstructural observations revealed that the rhamphotheca layer is composed of overlapping scales. Overlapping keratin scales are a common structure observed in structural material made of keratin such as the exterior of skin, nail or avian beaks (35). The keratin scales create friction upon movement by their stacking morphology, thus functioning as a dissipating agent. In particular, the layout of keratin scales in woodpeckers' beaks is designed to maximize friction. The keratin scales' increasing number density within the beak creates more frictional area for shearing (Figure 2.3(b)). The keratin scales in the woodpecker's rhamphotheca are thinner than those of the toucan and hornbill. The thickness of a single keratin scale of the woodpeckers' beaks is 0.2~1 μm, whereas that of the toucan's beak is 2~10 μm (26). Due to the similar overall thicknesses of rhamphotheca (approximately 500 μm), the number of keratin scales in the woodpeckers' beaks is much greater than that of the toucan. As such, more keratin scales admit more frictional area thus inducing greater frictional dissipation via the shearing mechanism. In addition to the greater frictional shearing area, the rough surface area between the scales also assists with energy mitigation (Figure 2.3(c)). The way that the keratin scales are arranged is also efficient to block crack propagation. Figure 2.9 shows the transverse plane of the woodpecker rhamphotheca illustrating the overlapping pattern of the keratin scales. A similar overlapping structure has also been observed in some structural biological materials including nacre, bone, and dentine (36). The overlapping structure induces a physical restraint against free movement of the blocks, and hence it does not allow crack propagation, thus providing a greater fracture toughness and robustness to biological materials (36-38). As such, an

overlapping arrangement of keratin scales in the rhamphotheca also provides a greater fracture toughness to resist fracture during high speed pecking.

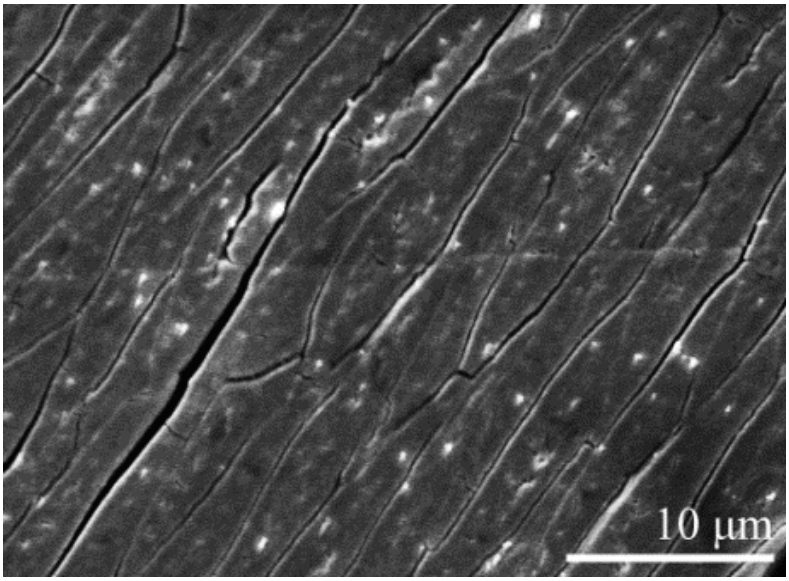

Figure 2.9 Overlapping pattern of keratin scales.

The scanning electron microscopic image on the polished rhamphotheca of the woodpecker's beak at the transverse plane shows the overlapping pattern of the keratin scales.

Micromechanically, the microhardness of the rhamphotheca of the woodpecker is about 50% greater than those of other birds such as the toucan, hornbill, and starling. It is reported that the dark-color beaks have a greater hardness than light-colored beaks, so the dark beaks are less susceptible to wear (29). Since the color of woodpeckers' beaks is predominantly black, then one would expect a greater hardness if the European starlings study (29) is consistent with woodpeckers' beaks. Our study also shows that the microhardness of the core part of the woodpeckers' beaks is indeed two to three times greater than those of the toucan and hornbill beaks (Table 2.1). Clearly, in terms of the structure-function relationship, hardness differences would be expected in the

woodpeckers' beaks versus the toucan and hornbill because the high rate shocks would be much greater for the woodpecker.

2.4.3 Nanostructure-mechanical property relations

From the nanostructure of the woodpeckers' beaks as shown in Figure 2.4(e), one can observe that mechanical anisotropy arises, because the fibers are oriented parallel to the pecking direction. Bonser et al. (39, 40) reported that ostrich claw and feather, composed of β-keratin, displays anisotropy in which the Young's modulus in the longitudinal direction of the claw was 28% greater than in the transverse direction, and the toughness of the feather also showed anisotropy according to the fiber direction. Likewise, the fibers in the rhamphotheca provide strong mechanical properties in the longitudinal direction. Since the mechanical stress exhibited in the woodpeckers' beaks are mostly realized along the longitudinal axis, this may provide an advantage to the functioning of the beaks.

Additionally, the results of nanoindentation tests and nanostructural analysis show that data from the bony part has a large standard deviation as shown in Figure 2.8. This is indicative of the heterogeneous nature of the bony layer, which comprises fibers and a mineral matrix. Various values were measured across the span of the bony layer. The hardness and reduced elastic modulus were greater at the location where there was mostly a mineral matrix, and they were lower where there was a greater fiber density but lower mineral content.

2.4.4 Comparison to other bird's beaks

The structure of the woodpeckers' beak is different from other birds' beaks such as the chicken and toucan. The micro and nano structure of chickens' beaks is compared here to the woodpeckers' beaks along with literature data on the structure of a toucan's beak. While the woodpeckers' beaks are used for penetrating and grabbing food deep within a tree, chickens' beaks are used for grabbing food from more shallow sources, and toucans' beaks are used for crushing fruits. The difference in function is related to the difference in multiscale structure and mechanical properties.

Woodpeckers' beaks show some meaningful multiscale structural differences compared to other birds' beaks such as those from chickens or toucans. First, keratin scales of the woodpeckers' rhamphotheca are more elongated than the two other birds' beaks as shown in Figure 2.10. The dimension of the keratin scales from the woodpecker is 55 x 15 x 0.2 μm, and the aspect ratio of the height over the width is about 3.67. The dimension of the chicken's keratin scale is 30 x 10 x 1 μm with an aspect ratio of the height over the width being about 3. The dimension of the toucan's keratin scale is 45 x 45 x 1 μm having an aspect ratio of about 1 (27). The keratin scales dissipate mechanical load by friction as one scale slides against another scale. Adams et al. (42) reported that the geometry of the scales generates anisotropy and the elongated direction of the scale can dissipate more energy than the shorter direction. This is called the differential friction effect. With respect to the differential friction effect, the large anisotropy in the longitudinal direction in the woodpeckers' beaks provides high friction to withstand the impact loading in the longitudinal direction.

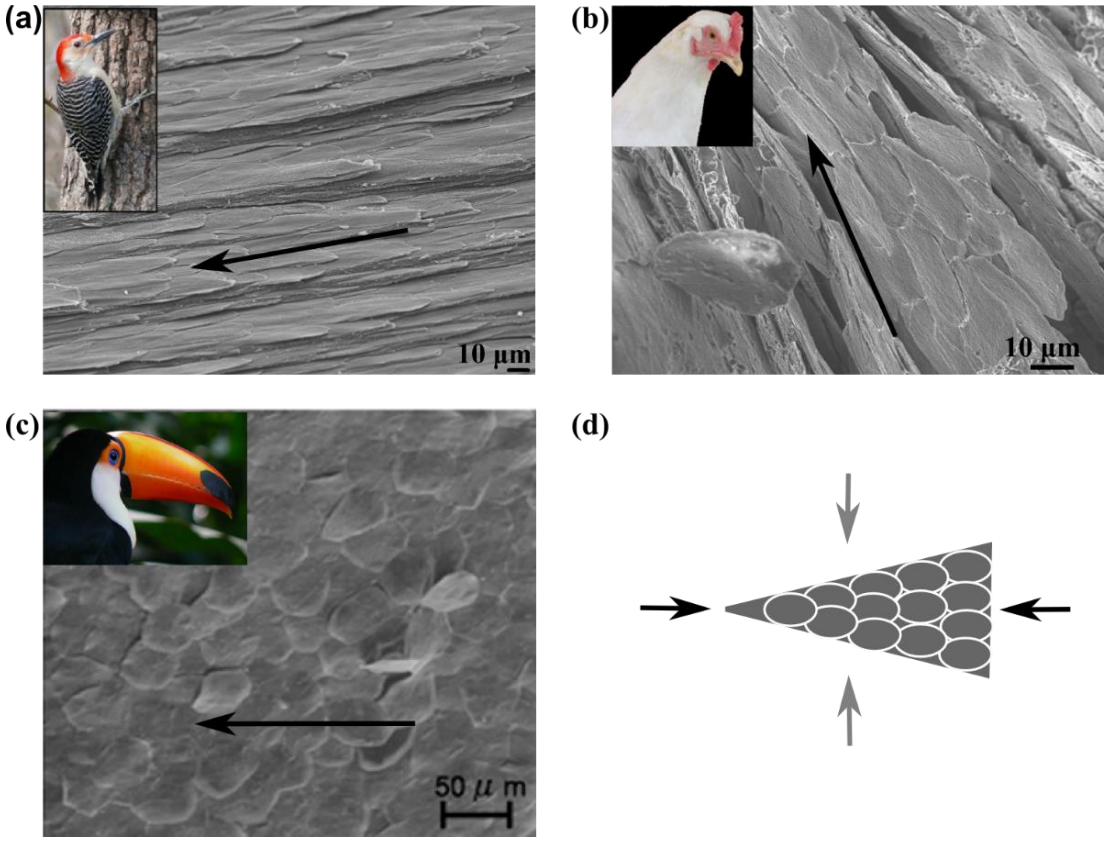

Figure 2.10 The dimensions and aspect ratios of the height over the width of a keratin scale from each bird are different according to their functions.

Dimensions and aspect ratio of the height over the width of each bird's beak are (a) 55 x 15 x 0.2 μm and 3.67 for woodpeckers, (b) 30 x 10 x 1 μm and 3 for chickens, and (c) 45 x 45 x 1 μm and 1 for toucans (26). (d) The geometry of keratin scales affects anisotropy of beaks. Black arrows indicate longitudinal direction, and grey arrows indicate transverse direction.

Secondly, the porosity of the woodpeckers' beaks is different than that of the chicken and toucan (figure 2.11). While the bony layers of the beaks from the chicken and the toucan have a closed-cell type foam with a membrane, the bony layer of the woodpecker's beak is not a foam material. The porosity of the woodpecker's bony layer is 9.9 ± 3.0 %, and the porosity levels of the bony layer of the chicken and the toucan are 42.3 ± 1.3 % and 61.5 ± 2.0 %, respectively. As the porosity increases, the bulk modulus

and the density of a material decrease. Therefore, the bulk modulus of the woodpecker's bony layer is greater than the chicken and toucans' bony layer if the moduli from the nanoscale are similar. This in turn has an effect on the stress wave moving through the beak as the wave speed increases as the moduli per density increases. Hence, the woodpeckers' beaks would propagate the shock wave faster than the two other birds' beaks and in doing so, guides the wave to the hyoid bone. Also in this context, Genbrugge et al. (24) showed a large difference when comparing the trabecular porosity in the beaks of Java and Darwin's finches thus relating their structure to their different feeding habits. When considering these different birds' beaks, one can assess that the porosity directly affects the light-weight of the beak, the wave speed, the strength, and the directionality and means of each bird's eating function.

Figure 2.11 The inner layers of the birds show various porosities according to their function.

(a) Woodpecker's bony layer having porosity of 9.9 ± 3.0 %, (b) chicken's beak having porosity of 42.3 ± 1.3 %, and (c) toucan's beak having porosity of 61.5 ± 2.0 % (27).

The next unique feature of the woodpeckers' beaks is the wavy structure (suture lines) as shown in Fig.12. The images taken via TEM from the rhamphotheca of the woodpecker, chicken, and toucan show the wavy structure. Although the beaks of the chicken and the toucan also show the wavy structure, the waviness (i.e., the ratio of

height to width) of those birds' beaks is less than that of woodpecker's beak. The waviness of the woodpeckers' beaks is approximately 1, while that of the chicken's beaks is approximately 0.3, and that of the toucan's beak is approximately 0.05. The geometry of the wavy structure also can be found in other biological materials such as a human skull and turtle shell, which both resist compressive loads (43-45). Typically, the suture lines have a space between them comprised of collagen. When a load is imposed on the suture line, shearing will result in which the collagen is compressed and frictional forces will result thus helping to dissipate the load. Li et al. (46, 47) also reported that the wavy structure's role is to provide extra stiffness and strength based on its geometry. Similarly, the wavy line in the woodpeckers' beaks is assumed to have the capability of withstanding compressive load.

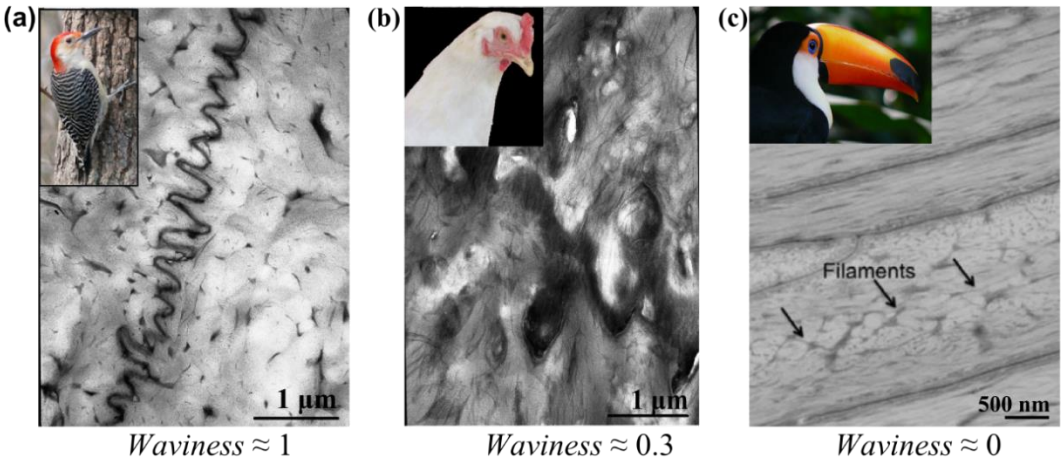

Figure 2.12 The wavy structure shown in the rhamphotheca.

(a) Woodpecker having waviness of 1, (b) chicken having waviness of 0.3, and (c) toucan having waviness of 0.05 (26).

2.5 Conclusions

In this study, we examined the complicated, multiscale heterogeneous structure and mechanical properties of Red-Bellied Woodpecker (*Melanerpes carolinus*) beaks. The woodpeckers' beaks are a structural biocomposite having three layers; rhamphotheca (outer keratin shell), middle foam layer, and inner bony layer. Along the beak from posterior to anterior, the area fraction of these three layers gradually changes, so the aggregate modulus and aggregate hardness are gradients. The rhamphotheca is made up of elongated keratin scales, and the microhardness of the rhamphotheca was measured to be ~323 MPa and the nanohardness ~470 MPa. The foam layer is a continuous unification of the rhamphotheca and bony layer, and the nanohardness of the foam layer was ~243 MPa. The bony layer consists of mineralized collagen with a big cavity, and the microhardness of the bony layer was measured to be ~636 MPa and the nanohardness ~2 GPa.

In summary the three structures found in woodpecker's beak could be used as design guidelines to lower the directional stress levels in structures, because of their geometric and material integration: an elongated geometry of keratin scales that can slide over each other, lower porosity, and a wavy structure with a small gap to admit local shearing. The results from this paper, in revealing the structure-properties of woodpeckers' beaks, can provide promising features for energy absorption in designing man-made devices.

2.6 References

1. May PRA, Fuster JM, Haber J, Hirschman A. Woodpecker drilling behavior. An endorsement of the rotational theory of impact brain injury. Archives of neurology. 1979;36(6):370.

2. Backhouse F. Woodpeckers of North America: Firefly Books Ltd; 2005.

3. Bock WJ. Functional and evolutionary morphology of woodpeckers. Ostrich: Journal of African Ornithology. 1999;70(1):23-31.

4. Kirby VC. An adaptive modification in the ribs of woodpeckers and piculets (Picidae). The Auk. 1980:521-32.

5. Spring LW. Climbing and pecking adaptations in some North American woodpeckers. The Condor. 1965;67(6):457-88.

6.Wygnanski-Jaffe T, Murphy C, Smith C, Kubai M, Christopherson P, Ethier C, et al. Protective ocular mechanisms in woodpeckers. Eye. 2005;21(1):83-9.

7. May PRA, Fuster JM, Newman P, Hirschman A. Woodpeckrs and head injury. The lancet. 1976;1(7957).

8. Schwab IR. Cure for a headache. British Journal of Ophthalmology. 2002;86(8):843.

9. Gibson L. Woodpecker pecking: how woodpeckers avoid brain injury. Journal of Zoology. 2006;270(3):462-5.

10. Oda J, Sakamoto J, Sakano K. Mechanical Evaluation of the Skeletal Structure and Tissue of the Woodpecker and Its Shock Absorbing System. JSME International Journal Series A. 2006;49(3):390-6.

11. Wang LZ, Zhang HQ, Fan YB. Comparative study of the mechanical properties, micro-structure, and composition of the cranial and beak bones of the great spotted woodpecker and the lark bird. Science China Life Sciences. 2011;54(11):1036-41.

12.Wang L, Cheung JTM, Pu F, Li D, Zhang M, Fan Y. Why do woodpeckers resist head impact injury: a biomechanical investigation. PLoS ONE. 2011;6(10):e26490.

13. Wang L, Fan Y, editors. Role of Mechanical Performance of Cranial bone in Impact Protection of Woodpecker Brain–A Finite Element Study. World Congress on Medical Physics and Biomedical Engineering May 26-31, 2012, Beijing, China; 2013: Springer.

14. Zhu ZD, Ma GJ, Wu CW, Chen Z. Numerical study of the impact response of woodpecker's head. AIP Advances. 2012;2(4).

15. Yoon SH, Roh JE, Kim KL. Woodpecker-inspired shock isolation by microgranular bed. Journal of Physics D: Applied Physics. 2009;42:035501.

16. Yoon SH, Park S. A mechanical analysis of woodpecker drumming and its application to shock-absorbing systems. Bioinspiration & Biomimetics. 2011;6:016003.

17. Horstemeyer MF, inventor; Horstemeyer, M. F., assignee. Shock mitigating material and method utilizing spiral shaped elements. United States patent US20140026279 A1. 2014 Jan 30.

18.Meyers MA, Lin AYM, Seki Y, Chen PY, Kad BK, Bodde S. Structural biological composites: an overview. Journal of the Minerals, Metals and Materials Society. 2006;58(7):35-41.

19. Sanchez C, Arribart H, Guille MMG. Biomimetism and bioinspiration as tools for the design of innovative materials and systems. Nature Materials. 2005;4(4):277-88.

20. Xia F, Jiang L. Bio Inspired, Smart, Multiscale Interfacial Materials. Advanced Materials. 2008;20(15):2842-58.

21. Lucas AM, Stettenheim PR. Avian anatomy: integument: U.S. Agricultural Research Service; 1972.

22. Ritchie BW, Hsarrison GJ, Zantop D, Harrison LR. Avian medicine: Principles and application; Abridged edition: Wingers Pub; 1997.

23. Stettenheim PR. The integumentary morphology of modern birds—An overview. American Zoologist. 2000;40(4):461-77.

24.Genbrugge A, Adriaens D, Kegel B, Brabant L, Hoorebeke L, Podos J, et al. Structural tissue organization in the beak of Java and Darwin's finches. Journal of Anatomy. 2012;221(5):383-93.

25.Fecchio R, Seki Y, Bodde S, Gomes M, Kolososki J, Rossi Jr J, et al. Mechanical behavior of prosthesis in Toucan beak (Ramphastos toco). Materials Science and Engineering: C. 2010;30(3):460-4.

26. Seki Y, Bodde SG, Meyers MA. Toucan and hornbill beaks: A comparative study. Acta Biomaterialia. 2010;6(2):331-43.

27. Seki Y, Kad B, Benson D, Meyers MA. The toucan beak: structure and mechanical response. Materials Science and Engineering: C. 2006;26(8):1412-20.

28. Seki Y, Schneider MS, Meyers MA. Structure and mechanical behavior of a toucan beak. Acta Materialia. 2005;53(20):5281-96.

29. Bonser RHC, Witter MS. Indentation hardness of the bill keratin of the European starling. Condor. 1993:736-8.

30. Roman P, Gutierrez-Zorrilla JM. A quick method for determining the density of single crystals. Journal of Chemical Education. 1985;62(2):167.

31. Bragulla HH, Homberger DG. Structure and functions of keratin proteins in simple, stratified, keratinized and cornified epithelia. Journal of anatomy. 2009;214(4):516-59.

32. Wainwright SA. Mechanical design in organisms: Princeton University Press; 1982.

33.Fratzl P, Gupta H, Paschalis E, Roschger P. Structure and mechanical quality of the collagen–mineral nano-composite in bone. J Mater Chem. 2004;14(14):2115-23.

34. Fung Y, Cowin S. Biomechanics: Mechanical properties of living tissues. Journal of Applied Mechanics. 1994;61(4):1007-.

35.McKittrick J, Chen PY, Bodde S, Yang W, Novitskaya E, Meyers M. The Structure, Functions, and Mechanical Properties of Keratin. JOM Journal of the Minerals, Metals and Materials Society. 2012:1-20.

36.Katti KS, Katti DR, Pradhan SM, Bhosle A. Platelet interlocks are the key to toughness and strength in nacre. Journal of materials research. 2005;20(05):1097-100.

37. Gao H, Ji B, Jäger IL, Arzt E, Fratzl P. Materials become insensitive to flaws at nanoscale: lessons from nature. Proceedings of the National Academy of Sciences of the United States of America. 2003;100(10):5597.

38. Jäger I, Fratzl P. Mineralized Collagen Fibrils: A Mechanical Model with a Staggered Arrangement of Mineral Particles. Biophysical Journal. 2000;79(4):1737-46.

39. Bonser RHC. The Young's modulus of ostrich claw keratin. Journal of materials science letters. 2000;19(12):1039-40.

40. Bonser RHC, Saker L, Jeronimidis G. Toughness anisotropy in feather keratin. Journal of materials science. 2004;39(8):2895-6.

41. Soons J, Herrel A, Aerts P, Dirckx J. Determination and validation of the elastic moduli of small and complex biological samples: bone and keratin in bird beaks. Journal of The Royal Society Interface. 2012;9(71):1381-8.

42. Adams M, Briscoe B, Wee T. The differential friction effect of keratin fibres. Journal of Physics D: Applied Physics. 1990;23:406.

43.Krauss S, Monsonego Ornan E, Zelzer E, Fratzl P, Shahar R. Mechanical Function of a complex three dimensional suture joining the bony elements in the shell of the red eared slider turtle. Advanced Materials. 2009;21(4):407-12.

44. Jaslow CR. Mechanical propertise of cranial sutures. J Biomechanics. 1990;23(4):313-21.

45. Curtis N, Jones M, Evans S, O'Higgins P, Fagan M. Cranial sutures work collectively to distribute strain throughout the reptile skull. Journal of The Royal Society Interface. 2013;10(86).

46. Li Y, Ortiz C, Boyce MC. Bioinspired, mechanical, deterministic fractal model for hierarchical suture joints. PHYSICAL REVIEW E Phys Rev E. 2012;85:031901.

47. Li Y, Ortiz C, Boyce MC. Stiffness and strength of suture joints in nature. 2011.

CHAPTER III

THE GEOMETRIC EFFECTS OF A WOODPECKER'S HYOID APPARATUS IN STRESS WAVE MITIGATION

3.1 Introduction

The speed of a woodpecker's peck is approximately 6~7 m/s (1). In spite of the high speed and high frequency impacts, a woodpecker head remains intact by efficiently dissipating the impact energy. Research shows that the primary features protecting the woodpecker's head from high impact include the beak with elongated keratin scales and a wavy suture, the spongy bone in the upper beak, the small brain being tightly enclosed within the skull, and the cranial bone shaped like a plate with high strength (2-6).

Another unique feature found in the woodpecker's head is an extended hyoid apparatus. The hyoid apparatus consists of the bones of the tongue and associated connective tissues in the upper throat of a bird. The hyoid apparatus is small and short in most species but is greatly elongated in woodpeckers. As shown in Figure 3.1, the hyoid apparatus of a woodpecker starts at the beak tip, surrounds the skull, and ends at the upper beak/front head intersection. Anatomically, the hyoid has no bony connections to the skull but is slung by muscles, which allow it to move forward during probing and backward during closing of the beak. One of the purposes of the elongated hyoid is for effectively obtaining food. Bock (5) mentioned that the amount of extension of a woodpecker's tongue depends on the forage types. Sapsuckers eat sap and cannot extend

their tongue as far as flickers and woodpeckers, which forage for insects and larvae in trees. On the other hand, some researchers considered that the hyoid apparatus acts as a shock absorber or would serve to distribute the forces (7, 8). One study (9) argued that the hyoid apparatus was a safety belt for the woodpecker's head after impact, and another study (10) reported that most of the high-value stress waves goes into the hyoid apparatus during impact. Liu et al. (11) performed a simulated comparative study between woodpecker head models with and without a hyoid apparatus. They found that the hyoid apparatus reduced the maximum shear stress by 20% to 30% thus giving an indication that the amount of energy absorbed by the hyoid apparatus dissipates approximately that amount. Liu et al. (11) also argued that the hyoid apparatus may play a role as a safety belt as well.

Here, we focus on the role of the hyoid apparatus as a shock absorber. Since the tongue, which is at the tip of the hyoid apparatus, contacts the lower beak (Figure 3.1(c)) when it is impacted, a portion of the impact pressure will propagate through the hyoid apparatus. The propagated stress waves can be amplified, reduced, canceled, or distorted by reflecting or refracting at the boundaries. In a previous work (12), we evaluated the geometric effects of stress wave propagation. The following four different geometries were used in the analysis (12): 1. a straight cylinder, 2. a straight cylinder that was tapered to a point, 3. a cylinder that was spiraled in a two dimensional plane, and 4. a cylinder that was tapered and spiraled in a two dimensional plane. The geometric effects on the stress wave propagation were investigated by several other researchers as well (13-14). The results from our geometric effects study showed that the tapered spiral geometry mitigated the greatest amount of pressure independent of material type. Taking into

consideration these results, we hypothesized that the spiral geometry observed from the lateral view of the hyoid as shown in Figure 3.1 and the tapered geometry, which is formed by the changing diameter from thick to thin, will play a critical role in dissipating shock energy. In our study, the FE model of the hyoid apparatus was developed using Abaqus/Explicit (15) to analyze the impact wave propagation and damping effects.

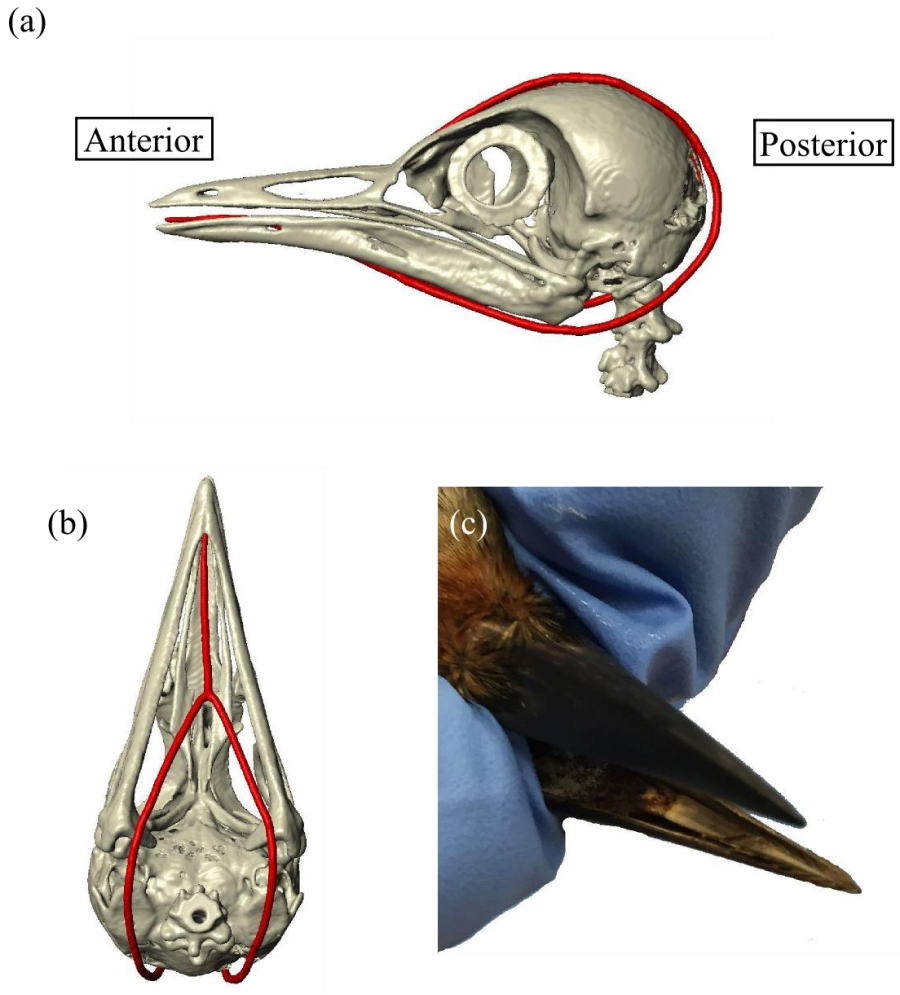

Figure 3.1 Hyoid apparatus in a Red-bellied woodpecker, *Melanerpes carolinus*.

Hyoid apparatus surrounding a skull in (a) Lateral view and (b) inferior view. (c) The tip of the hyoid (paraglossum) contacts to the beak at inside of the lower beak.

3.2 Materials and methods

The hyoid apparatus was dissected from the adult Red-bellied Woodpecker, *Melanerpes carolinus*, which lives in the Southern United States. Deceased woodpeckers were obtained from the collections of the Department of Wildlife, Fisheries and Aquaculture (Mississippi State University). The hyoid apparatus, which comprises a bone encapsulated by muscle tissue, was separated from the body of woodpecker as shown in Figure 3.2(a). The cross-sectional structure of the hyoid apparatus was characterized by using an optical microscope. Mechanical experiments were conducted using nano-indentation at room temperature and ambient relative humidity. For nano-indentation testing, samples were mounted into epoxy by using a cold mount technique and then thoroughly polished. The tests were conducted by using a Triboindenter® (Hysitron Incorporated, Minneapolis) with a tip of a Berkovich type indenter. The loading condition was controlled as follows: 15 s loading segment, a 45 s unloading segment, and 2000 μN applied maximum load. The reduced elastic modulus was derived from the initial unloading contact stiffness (Equation 3.1),

$$S = \frac{dP}{dH} = \frac{2}{\pi} E_r \sqrt{A} \tag{3.1}$$

where S is the stiffness, P is the maximum applied load (N), A is the loaded area, and the H is the maximum displacement. The reduced elastic modulus, E_r, is also derived from the displacement from both the specimen and the indenter. From the reduced elastic modulus, Young's modulus is given by the following,

$$E_{specimen} = \frac{E_{indenter} \times E_r}{(E_{indenter} - E_r)} \times \frac{(1-\nu_{specimen}^2)}{(1-\nu_{indenter}^2)} \tag{3.2}$$

where E and ν are the elastic modulus and Poisson's ratio of the specimen and the indenter, respectively.

3.3 Experimental measurements and finite element set up

Using optical microscopy, we observed the microstructure of the cross-section. As shown in Figure 3.2(a), the length of the hyoid apparatus of the Red-bellied Woodpecker is about 110 mm. The diameter of the core bone is approximately 1~3 mm and changes gradually from being thick at the tip to being thin and flexible at the end. In Figure 3.2(b), it is shown the muscle fully encasing the bone which diameter is approximately 1 mm at the back part of the hyoid. The thickness of the muscle surrounding the bone is about 0.3 mm. The muscle tissue was not active but dead and passive and was the only muscle from the head that was used in our simulations. Figure 3.2(c) is the muscle, and Figure 3.2(d) is the bone having a small pore at its center (16).

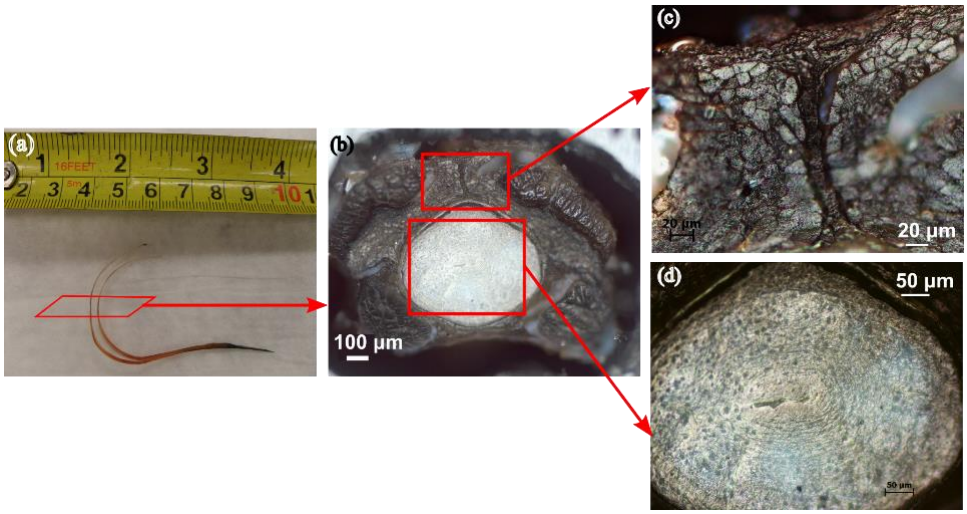

Figure 3.2 Micrographs of the hyoid apparatus.

(a) A dissected hyoid apparatus from a red-bellied woodpecker followed by optical microscope images of (b) the cross-section of the hyoid apparatus, (c) the adjacent muscle, and (d) the inner bone.

Nano-indentation tests were conducted at twelve locations (n=12) along the cross-section of the hyoid bone. The nanohardness was quantified as 692.9±170.1 MPa, and the reduced elastic modulus was 17.49±3.17 GPa. The value of reduced elastic modulus of the hyoid bone measured here is in the range of literature values of bones (17) . Using Eq. (2) with material properties of the diamond tip E = 1220 and ν=0.2, the elastic modulus of the bone part of the hyoid was quantified as 16.13 GPa**.**

Based on the structure observed under the microscope, the hyoid apparatus finite element mesh was built as the natural structure comprising interior bony material and exterior muscle. In the simulation, the materials were assumed to be homogeneous and isotropic solids. For the bone, the elastic modulus was 16.13 GPa; the density was 1850 kg/m3; and the Poisson's ratio was 0.3 (18). Hyperelastic and viscoelastic properties were used for the muscle with a density of 1100 kg/m3. We employed the Ogden model and Prony series expansion to describe the passive muscle behavior and viscoelasticity, respectively. The elastic parameters, μ and α, were 15.6 KPa and 21.4, and the viscoelastic parameters, δ and τ, were 0.549 and 6.01s, which were determined from rat muscle (19,20) . The muscle was constrained in all of the x, y, and z directions reflecting that the movement of the muscle is constrained by skull, but the bone was not assigned boundary conditions, since it was adjacent to the outer muscles. In addition, we considered that there were no gaps between the bone and muscle as an assumed perfect adhesion; this a good assumption, since it was very difficult to tear the muscle away from the bony part in the real material.

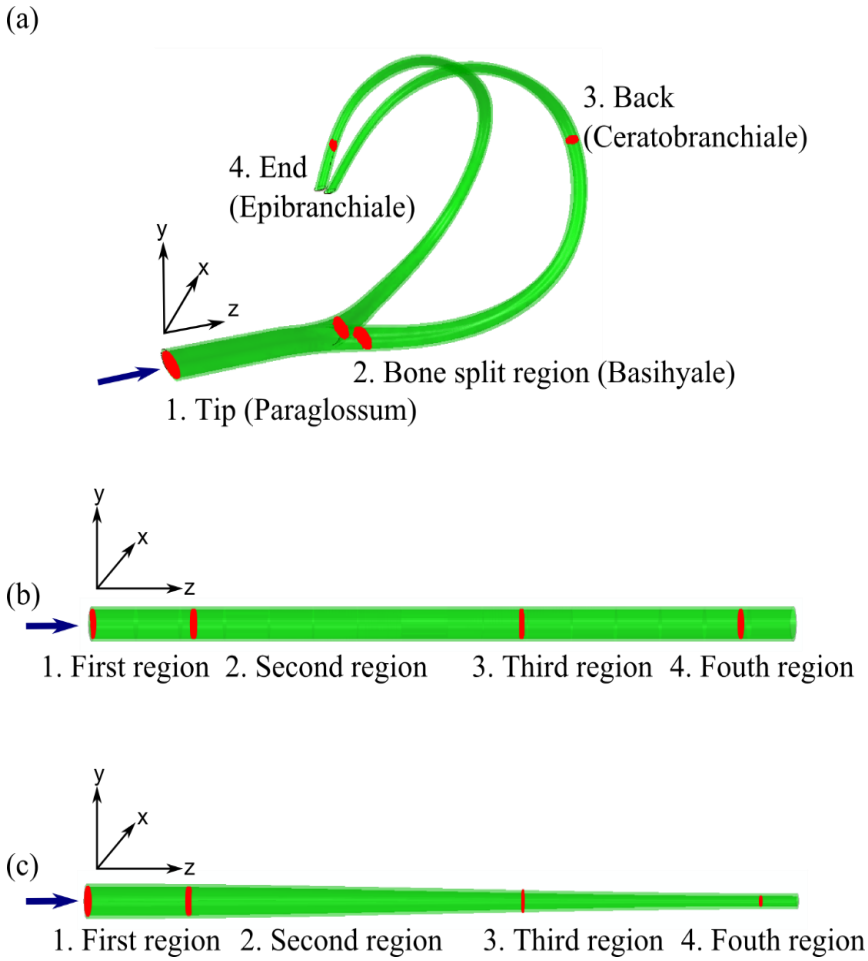

Figure 3.3 The finite element structures of the hyoid apparatus, the straight cylinder, and the tapered cylinder.

(a) The Finite Element (FE) geometry of the hyoid apparatus (including bone and muscle throughout the cross section) of a woodpecker. The anatomical terminology indicating the four regions are paraglossum (tip), basihyale (where the bone splits), ceratobranchiale (back), and epibranciale (end), respectively. (b) The straight cylindrical FE model and (c) the tapered cylindrical FE models (which also include bone and muscle) are also shown with the same distance markers used in the hyoid apparatus. The applied compressive load at the tip of the model (arrow) occurred into the z-direction, and the results were analyzed at the four different locations indicated by the red markings.

As shown in Figure 3.3(a), the impact was applied at the hyoid tip once. The impact pressure was 0.15 MPa, which was calculated from the force of a woodpecker pecking. The force of pecking was 3.108 N approximately since the mass, m, of the

woodpecker head was measured as 11.1 ± 6 g, and the acceleration, a, of pecking a tree was 280 m/s2. The acceleration was calculated from the velocity (7 m/s) and time (25 ms) of pecking a tree (8, 9). Then the force applied on to the woodpecker beaks is 3.108 N. Some part of the force will travel into the lower and upper beak, and the other portion will go through the hyoid apparatus (11). The cross-section of the beak and hyoid shows that the area of the hyoid is approximately one third of the total area, which consists of the upper beak, lower beak, and hyoid. The area where the force was applied to the hyoid is 3 mm. Therefore, the applied pressure that arose from the force over tip area of the bone portion was 0.15 MPa.

3.4 Results and discussion

3.4.1 Attenuation of pressure in the hyoid apparatus

Nature has many structures that are valuable for engineering-based bio-inspiration. In this context, the spirally shaped hyoid apparatus of the woodpecker is relevant for bio-inspired design of impact mitigating structures. As the first wave passed the four regions (tip, split, back, and end), the pressure and impulse as shown in Figure 3.4 were captured. The impulse is defined as the following,

$$J = \int_{t1}^{t2} \Delta p \, dt \tag{3.3}$$

where J is impulse per unit area, t is time, and p is pressure. The peak pressure decreased 75.00 % as the wave traveled along the hyoid apparatus from the anterior to the posterior end, and the impulse decreased 84.81 % suggesting that the hyoid had a good capability of impact attenuation. The mechanism that mitigates the impact pressure is discussed in the next section with regard to transferring a longitudinal wave into a shear wave and is

explained in the context of comparing the hyoid geometry to the SC geometry and TC geometry as shown in Figure 3.3.

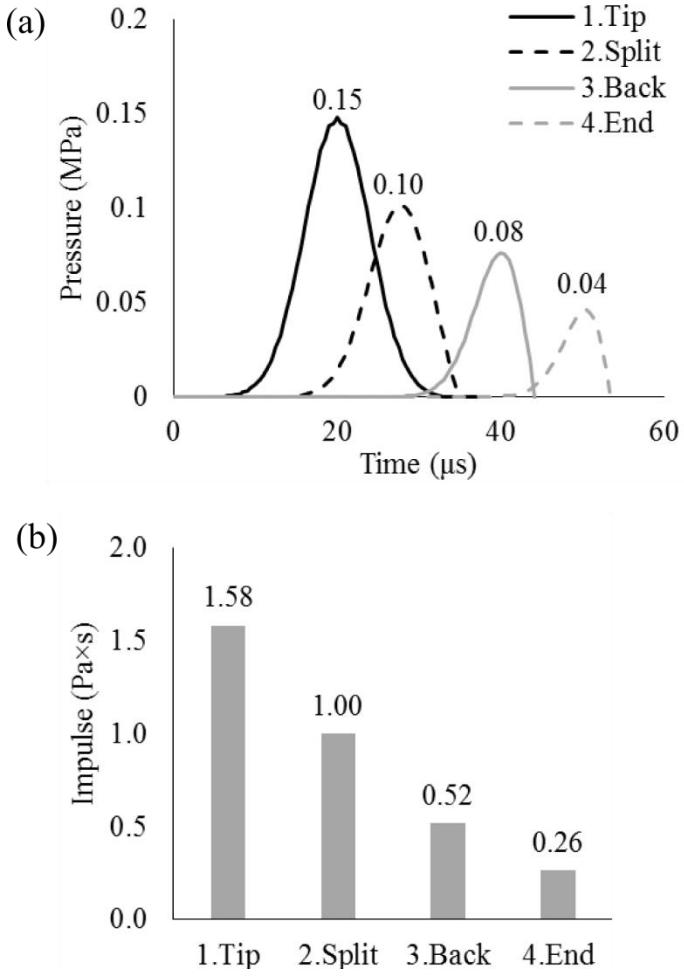

Figure 3.4 Pressure decay occurring at the hyoid apparatus.

(a) The pressure (of the first wave) versus time history at the four regions of the hyoid model. The number on the top of the curve indicates the peak pressure. (b) The impulse at the four regions of the hyoid model shows a decrease as a function of hyoid length.

3.4.2 Comparative study to the straight cylindrical (SC) geometry and tapered cylindrical (TC) geometry

There are several kinds of waves, but in the interest of this study, we will discuss longitudinal and transverse waves. In a longitudinal wave, displacements occur in a

parallel direction to the traveling wave; in a transverse wave, displacements occur in the perpendicular direction to the wave propagation. Longitudinal waves include sound and compressional elastic waves, while transverse waves include string waves, membrane waves, electromagnetic waves, and shear waves (14). Both longitudinal and transverse waves resulted from the hyoid, SC, and TC geometries following a compressive impact. The longitudinal impulse was calculated from the normal stress components (S11, S22, and S33), and the transverse impulse was calculated from shear stress components (S12, S23, and S31).

FE studies showed that the hyoid apparatus was more effective in mitigating a longitudinal wave when compared to the SC or TC geometry. Figure 3.5 shows the longitudinal impulse at the four different locations of the hyoid apparatus, SC geometry, and TC geometry with regard to the axial direction. The total longitudinal impulse of the pressure wave traversing the hyoid bone decreased 84% from tip to end. In contrast, at the SC geometry longitudinal impulse decreased 14%, and at the TC geometry the longitudinal impulse increased 45% from the tip to the end because the effect of the diameter decrease in the cross section that generated greater stresses (and hence impulses). Only the hyoid apparatus induced a longitudinal impulse decrease as the pressure wave travelled. Nature has many structures that are valuable for engineering-based bio-inspiration.

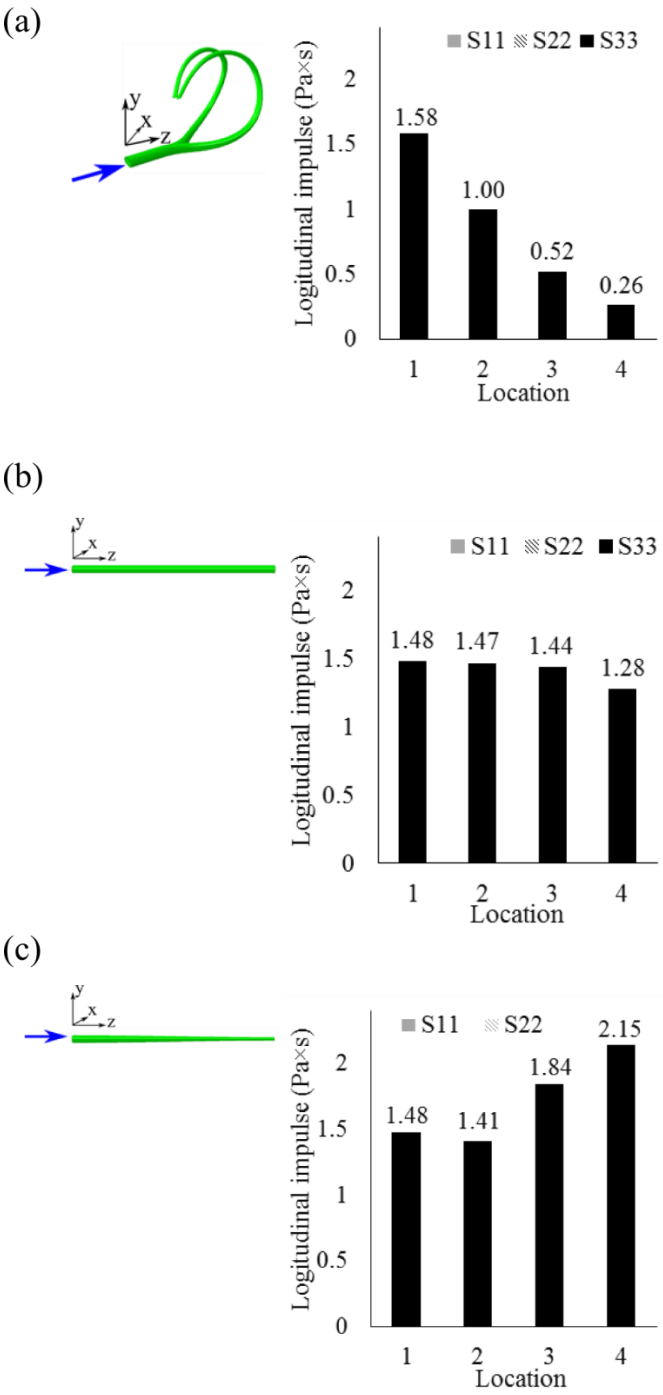

Figure 3.5 Longitudinal impact at three different geometries; hyoid, straight cylinder, and tapered cylinder.

The plots illustrate the longitudinal impulse for each normal stress component of S11, S22, and S33 at the four regions of (a) the hyoid apparatus, (b) straight cylinder, and (c) the tapered cylinder. S33 is in the loading direction, and it follows the axis of the hyoid structure. The wave propagates from the Location 1 to Location 4.

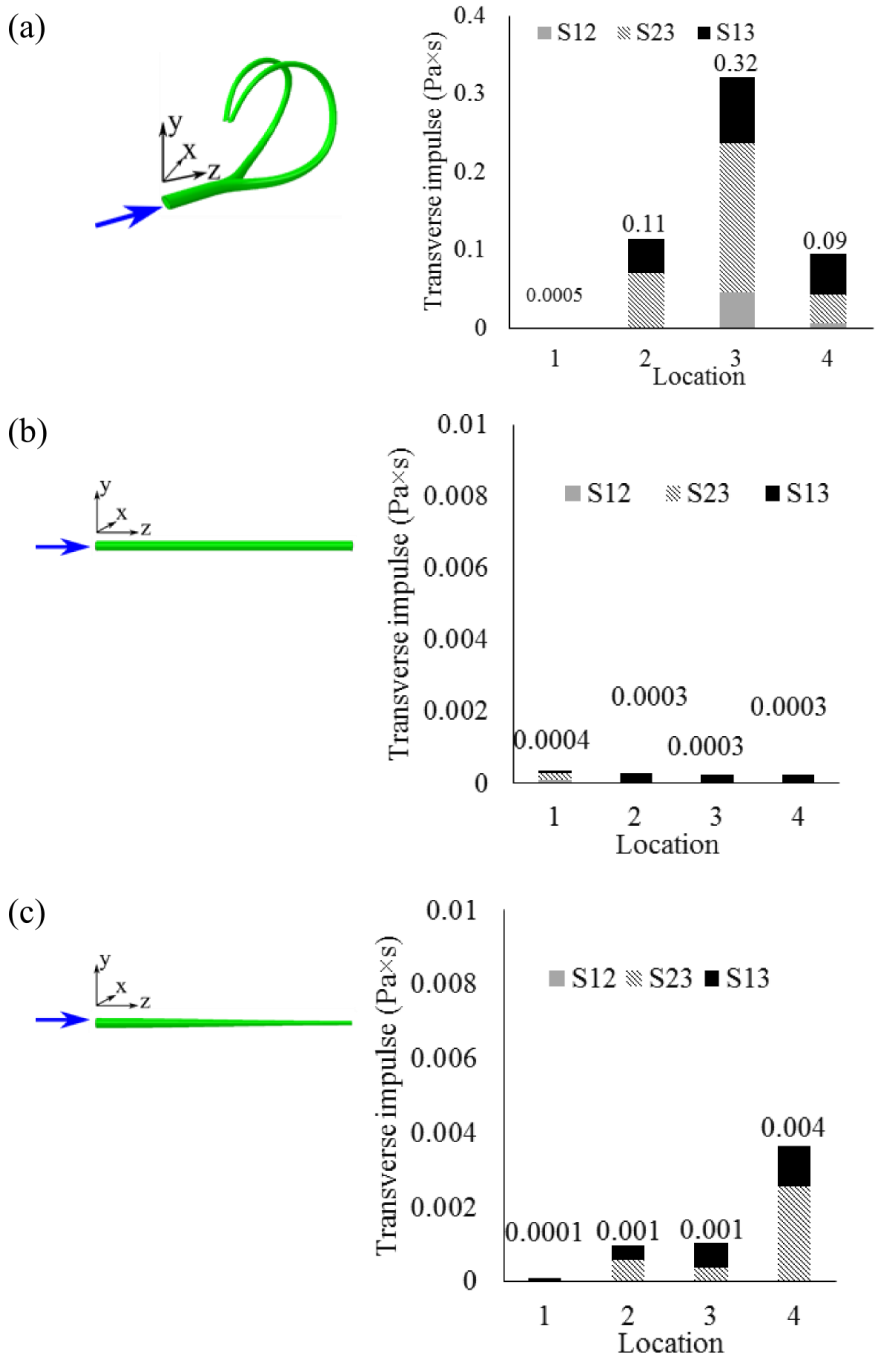

Figure 3.6 Transverse impact at three different geometries; hyoid, straight cylinder, and tapered cylinder.

The plots illustrate the transverse impulse for each shear stress component of S12, S23, and S13 at the four regions of (a) the hyoid apparatus, (b) the straight cylinder, and (c) the tapered cylinder. S33 is the loading direction. The wave propagates from the Location 1 to Location 4.

Figure 3.6 shows the transverse wave impulses for the hyoid geometry, SC geometry, and TC geometry for each of the shear stress components. For the hyoid geometry, S12 and S13 shearing was introduced at the bone split region due to the extension of the two arms in the x and y direction. At the back region of the hyoid apparatus, the intense shearing of S12, S23, and S13 induced from decreasing cross sectional area and the spiral geometry in which the stress wave shifted continuously by the angular change. When comparing the results of the hyoid geometry versus the SC and the TC results in Figure 3.6, one can observe that the shearing at the hyoid geometry was much greater than the other two geometries. When comparing the SC to the TC results, one can understand the difference that the reduced cross section makes. Because of the thinning geometry, a small amount of S23 and S13 were generated in the TC geometry. When comparing the hyoid to the TC results, one can compare the difference that the spiral and split geometry makes. The tapered (reduced cross section) geometry does help in reducing the longitudinal wave pressure and increases the shear stresses in the research of Johnson et al. (12).

As a result of the longitudinal-to-transverse wave transformation, the transverse waves led to displacement of the hyoid end in the lateral direction. Figure 3.7 shows the maximum transverse displacements found 10 mm away from the end of each geometry, and the value is 1.80 μm for the hyoid apparatus, 8.43e-8 μm for the SC, and 2.03e-5 μm for the TC. Note that the hyoid geometry produced the greatest amount of lateral displacements contrasted to the straight geometries, which produced minimal lateral displacements.

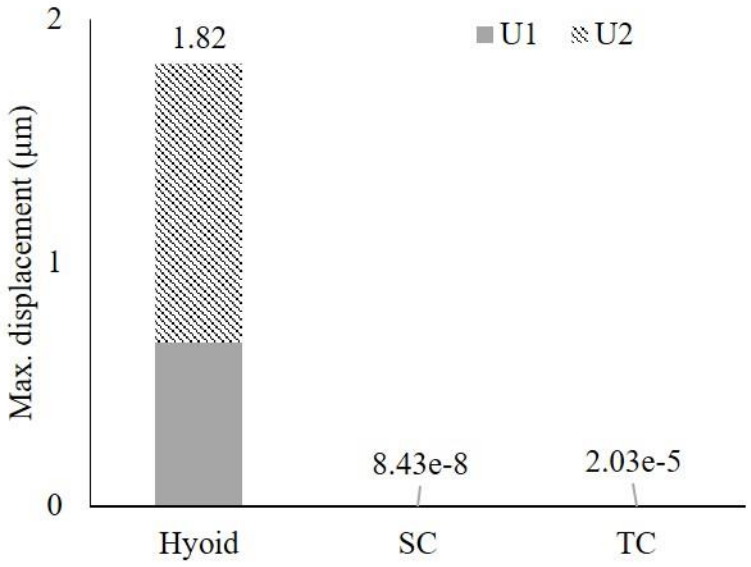

Figure 3.7 The maximum lateral displacements for the hyoid apparatus, the Straight Cylinder (SC), and the Tapered Cylinder (TC).

3.4.3 The role of the muscle on damping

The muscle can absorb energy via heat while it is loaded because of its viscoelastic behavior. Since the amount of energy dissipated in viscoelastic material is proportional to the damping coefficient multiplied by the strain energy stored in the component, increasing total strain energy in a muscle increases the system damping (21). Figure 3.8 shows that the strain energy of the muscle of the hyoid apparatus, SC geometry, and TC geometry. The muscle and bone were adhered perfectly in the FE model. As a result, the load transferred to the muscle, which is primarily caused by the movement of the bone. The complex wave interaction within the muscle surrounding the bone of the hyoid apparatus arose as a mixture of the initially induced longitudinal compression wave, but as the wave met the taper, fork, and spiral added shear waves arose. Figure 3.6 showed that the different shear components of the stress tensor were

induced in a complex manner. This complex wave interaction introduced greater strains within the muscle region, and as a result the hyoid muscle incurred much greater strain energy as illustrated in Figure 3.8. When the first stress wave reached to the end, the strain energy stored in the hyoid muscle was 1.10 mJ, and those in the SC muscle and TC muscle were 0.04 mJ and 0.08 mJ respectively. TC geometry resulted in two times greater strain energy than the SC geometry, which means two times more damping. Likewise, hyoid muscle caused approximately fourteen times greater strain energy than that of TC geometry, which is due to the existence of the fork region and curved shape of the hyoid geometry.

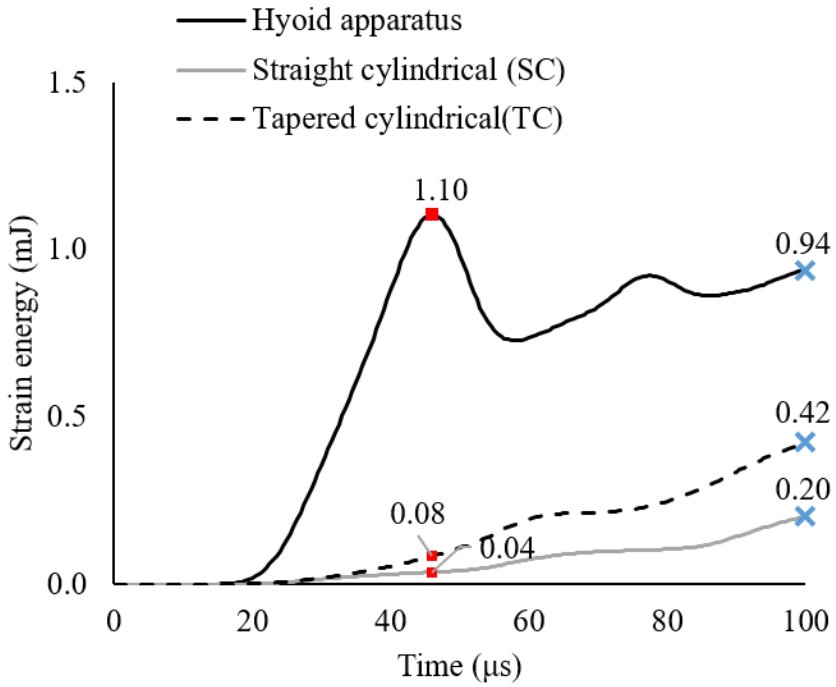

Figure 3.8 Strain energy of the muscle surrounding the bone of the hyoid apparatus, Straight Cylinder (SC), and the Tapered Cylinder (TC).

The red rectangle points indicate the strain energy level when the first wave reached the end, and the blue cross points indicates the strain energy level at the end of the simulations.

3.5 Conclusions

The woodpecker's hyoid apparatus is an effective device in mitigating pressure waves and transferring the energy to adjacent muscle for energy dissipation. Although it is a small component of the woodpecker's skeletal system, its role is critical for the woodpecker's safety. Here, we show that the spiral and tapered structure of the hyoid apparatus redistributed a uniaxial impact to shearing and lateral displacements as a longitudinal wave would strike the bony free surface and transform into a transverse wave. As the wave moved into the muscle, the energy efficiently dissipated because of the muscle's viscoelasticity.

- Because of the hyoid apparatus' structure, the initial impulse from the strike into a tree decreased 84% when it arrived at the hyoid end.
- Normal (longitudinal) impact waves transformed to transverse waves because (1) the cross-sectional area decreases and (2) the structure's curvature from the tip to the end thus inducing shear stresses to the lateral displacements into the dissipating muscle.
- The force exerted into the muscle caused by the hyoid bone motion generated a strain energy within the viscoelastic muscle, which then dissipated the impact energy.

The results of this work demonstrate a new understanding of energy dissipation mechanisms in biological materials such as the hyoid apparatus that can be implemented for the development of future bio-inspired material systems.

3.6 References

1. May PR, Fuster JM, Haber J, Hirschman A. Woodpecker drilling behavior: an endorsement of the rotational theory of impact brain injury. Archives of Neurology. 1979 Jun 1;36(6):370-3.

2. Gibson LJ. Woodpecker pecking: how woodpeckers avoid brain injury. Journal of Zoology. 2006 Nov 1;270(3):462-5.

3. Oda J, Sakamoto J, Sakano K. Mechanical evaluation of the skeletal structure and tissue of the woodpecker and its shock absorbing system. JSME International Journal Series A Solid Mechanics and Material Engineering. 2006;49(3):390-6.

4. Wang L, Zhang H, Fan Y. Comparative study of the mechanical properties, micro-structure, and composition of the cranial and beak bones of the great spotted woodpecker and the lark bird. Science China Life Sciences. 2011 Nov 1;54(11):1036-41.

5. Bock WJ. Functional and evolutionary morphology of woodpeckers. Ostrich. 1999 Mar 1;70(1):23-31.

6. Lee N, Horstemeyer MF, Rhee H, Nabors B, Liao J, Williams LN. Hierarchical multiscale structure–property relationships of the red-bellied woodpecker (Melanerpes carolinus) beak. Journal of The Royal Society Interface. 2014 Jul 6;11(96):20140274.

7. Schwab IR. Cure for a headache. British Journal of Ophthalmology. 2002 Aug 1;86(8):843.

8. May PRA, Fuster JM, Newman P, Hirschman A. Woodpeckers and head injury. The lancet. 1976;1(7957).

9. Wang L, Cheung JT, Pu F, Li D, Zhang M, Fan Y. Why do woodpeckers resist head impact injury: a biomechanical investigation. PloS one. 2011 Oct 26;6(10):e26490.

10. Zhu ZD, Ma GJ, Wu CW, Chen Z. Numerical study of the impact response of woodpecker's head. AIP Advances. 2012 Dec 1;2(4):042173.

11. Liu Y, Qiu X, Zhang X, Yu TX. Response of Woodpecker's Head during Pecking Process Simulated by Material Point Method. PloS one. 2015 Apr 22;10(4):e0122677.

12. Johnson KL, Trim MW, Horstemeyer MF, Lee N, Williams LN, Liao J, Rhee H, Prabhu R. Geometric effects on stress wave propagation. Journal of biomechanical engineering. 2014 Feb 1;136(2):021023.

13. Horstemeyer MF, inventor. Shock Mitigating Materials and Methods Utilizing Spiral Shaped Elements. United States patent application US 13/469,172. 2012 May 11.

14. Graff KF. Wave motion in elastic solids. Courier Corporation; 1975.

15. Manual AU. V6. 11. Dassault Systèmes Simulia Corp., Providence, RI, USA. 2011.

16. Zhou P, Kong XQ, Wu CW, Chen Z. The novel mechanical property of tongue of a woodpecker. Journal of Bionic Engineering. 2009 Sep 30;6(3):214-8.

17. Currey JD. The effect of porosity and mineral content on the Young's modulus of elasticity of compact bone. Journal of biomechanics. 1988 Jan 1;21(2):131-9.

18. Zysset PK, Guo XE, Hoffler CE, Moore KE, Goldstein SA. Elastic modulus and hardness of cortical and trabecular bone lamellae measured by nanoindentation in the human femur. Journal of biomechanics. 1999 Oct 31;32(10):1005-12.

19. Tham LM, Lee HP, Lu C. Cupping: from a biomechanical perspective. Journal of biomechanics. 2006 Dec 31;39(12):2183-93.

20. Bosboom EM, Hesselink MK, Oomens CW, Bouten CV, Drost MR, Baaijens FP. Passive transverse mechanical properties of skeletal muscle under in vivo compression. Journal of biomechanics. 2001 Oct 31;34(10):1365-8.

21. Plunkett R. Damping analysis: an historical perspective. InM 3 D: Mechanics and Mechanisms of Material Damping 1992 Jan. ASTM International.

CHAPTER IV

STRESS WAVE DISSIPATION AT SUTURE INTERFACES

4.1 Introduction

Biological materials are remarkably designed for efficient mechanical behavior. One elegant example is a suture joint, which is a simple geometry yet multifunctional. In biological structures, suture joints are commonly found where two stiff components interlock each other. For example, within the microstructure of the woodpecker beak, a wavy sinusoidal-geometry was observed under the transmission electron microscope (Figure 4.1(a)). Compared to other birds, whose beaks' impact is less than that of woodpeckers, the waviness of suture shown in woodpecker beaks is higher (1). As shown in Figure 4.1(b), the ammonoid fossil also shows a wavy structure with a fractal pattern on its shell. The suture of the ammonoid fossil has been studied to investigate its mechanical role and relation between hierarchical structures of sutures and function (2-4). Blasio (5) reported that complex suture lines dramatically diminished the strain and the stress in the phragmocone such that suture fluted septum reinforced the shell against hydrostatic pressure. The turtle shell also has suture joints in their carapace as shown in Figure 4.1(c). Krauss et al. (6) conducted three-point bending tests on the suture-contained turtle bony shell and reported that the turtle shell withstands small loads by low-stiffness deformation and becomes much stiffer when the external load increases beyond a certain threshold. The suture of the leatherback turtle was also studied and

revealed that the suture caused the balance between tension and shear, and brought structural flexibility by causing angular displacement (7). Figure 4.1(d) shows a suture in a human skull. This cranial suture has been researched extensively. Researchers reported that cranial sutures provide flexibility for growth, movement and strain due to masticatory, and impact energy dissipation (8-17).

Mechanically, the wavy suture can greatly enhance the strength of materials. Jaslow (13) experimentally studied mechanical properties of sutures and reported that the suture increased bending strength. Similar results on the tensile strength and bending strength have been reported as the suture plays a key role as an additive to increase strength (18-22). In addition, a study of an interfacial crack with hierarchical sinusoidal suture found that sutures enhance interfacial fracture toughness at mode-I and mode-II loadings (23).

Although sutures often found in the spot that dynamic responses occur, mechanisms of aforementioned properties of sutures during impact loading have not been extensively studied. Jaslow (13) studied energy absorption using pendulum at the cranial sutures of head-butting goats. Using finite element analysis, the role of cranial sutures was investigated. Maloul et al. (24) reported that sutures redistributed stress, and stress distribution was altered depending on impact loading directions. Zhang and Yang (25) pointed out that hierarchical design of cranial sutures benefited the stress attenuation and energy absorption.

The main objective of the present study is to investigate the geometrical effects of sinusoidal sutures on the stress wave mitigation by using FE models with elastic material properties.

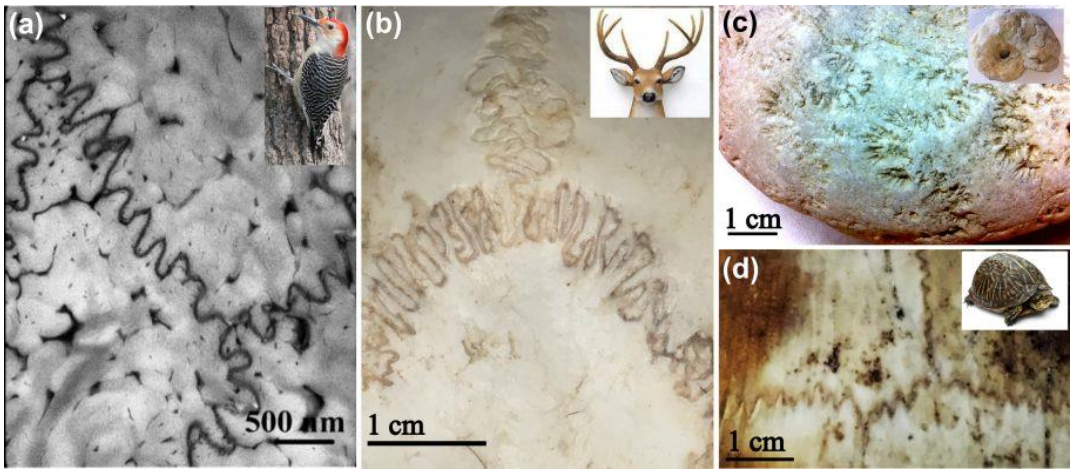

Figure 4.1 Suture lines from the biological materials.

(a) Suture line shown at the tip of woodpecker beaks (keratin); (b) cranial suture in a bison skull (bone); (c) wavy line in a surface of an ammonoid fossil (calcium carbonate), and; (d) suture at a box turtle (bone).

4.2 Materials and methods

An idealized bar with both a sutured interface (i.e., sutured bar) and an idealized bar with a flat interface (i.e., un-sutured bar) were created and analyzed using a two dimensional FE model in Abaqus/Explicit to run dynamic calcuations. As shown in Figure 4.2(a-b), the dimension of the full complex is 32mm×1000 mm (one side of the bar is 15mm×1000 mm with a gap thickness of 2mm). The wall was treated as an elastic and isotropic material with Young's modulus E = 8 GPa, Poisson's ratio ν=0.3, and density ρ=2000 kg/m3. The sutured and un-sutured gap was treated as a viscoelastic material, and it was assigned hyperelastic by employing the Ogden model with the elastic parameters, μ and a, were 15.6 KPa and 21.4 (26). The impact load was a Gaussian impulse and applied on one side of the bar (left side of the bar in Figures 2(a) and 2(b)) with the end nodes, on the same side, fully constrained to the y direction. The viscoelastic properties were assigned by Prony series with the viscoelastic parameters, d and t, were

0.549 and 6.01s, which were determined from rat muscle (27). For meshing, plane stress 4-noded element (CPS4R) was used, and the approximate element size was 0.5 mm generating about 100,000 number of elements in the entire structure. Then, a parametric study was performed to understand the dependency of the mitigation on suture geometric variations and external impact load. The seven factors are; (1) suture waviness, (2) Rsuture (ratio of the suture height to the entire bar thickness), (3) suture gap thickness, (4) elastic modulus of the wall, (5) geometry of the bar boundary walls, (6) amplitude of external impact load, and (7) impact duration, which are illustrated in Figure 4.3. The detail of the experimental case is described in Table 1. While examining one factor, the other factors were fixed.

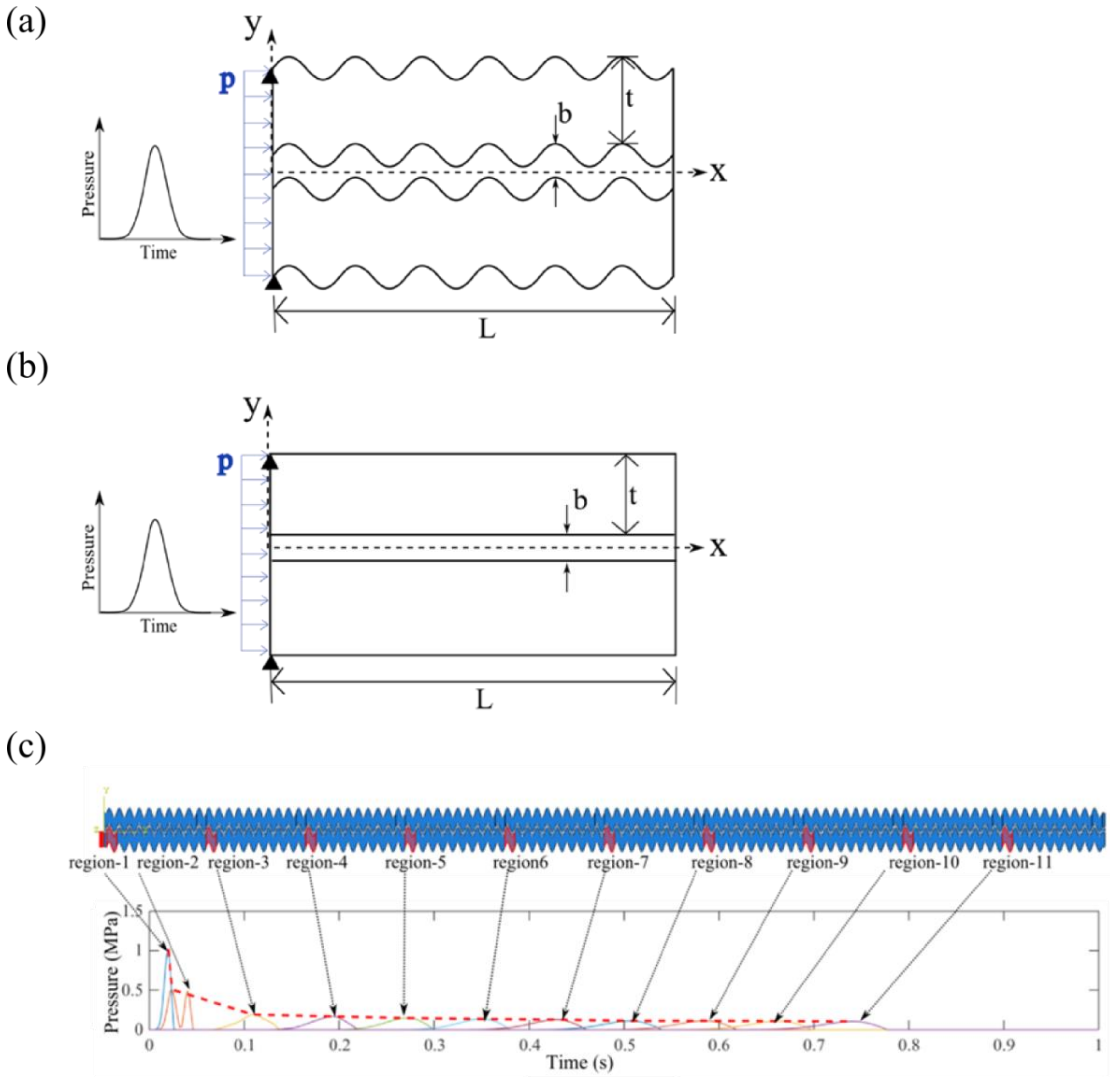

Figure 4.2 Idealized 2-D bars with interfaces of suture and non-suture.

(a) Idealized two dimensional bar with a suture interface of gap thickness of b. The dimension of the bar is L = 1000 mm, t = 15 mm, and b = 2 mm. The pressure impinged on the lefts side of the bar. (b) Idealized bar with a flat interface. (c) Following an initial impact pressure applied in Region-1, the pressure data were recorded at the eleven regions where indicated by the red regions at the bar. Then, the peak pressures were connected by red dotted line at the graph. As the pressure wave propagates the bar, the peak pressure was reduced.

In order to measure the extent of dissipation in the sutured bar, pressure-time history data were recorded at eleven regions along the bar, indicated by red regions in Figure 4.2(c). The damping capability of the sutured bar was then evaluated through the

damping quotient, which is the ratio of the pressure decay from the 'region-1' compared to 'region-11' as following:

$$Damping\ quotient = \frac{Pressure_{region-1} - Pressure_{region-11}}{Pressure_{region-1}} \quad (4.1)$$

Further, normalized phase velocity was also analyzed to investigate the influence of sutures to wave dispersion.

$$Normalized\ velocity = \frac{Phase\ velocity\ at\ a\ current\ bar}{Phase\ velocity\ at\ an\ un-sutured\ bar} \quad (4.2)$$

Table 4.1 Seven factors examined their influences on stress wave mitigation.

Factors	**Cases**
Waviness (height/width)	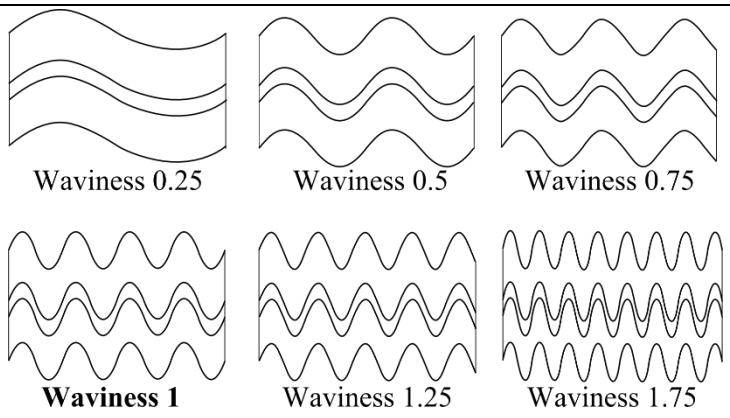
R_{suture} (suture height/ bar thickness)	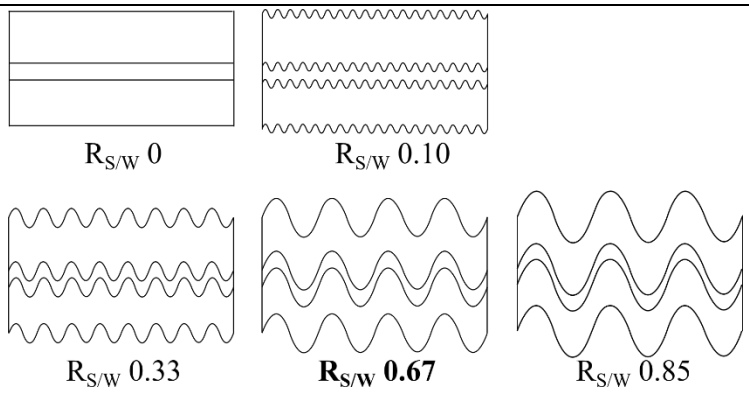

Table 4.1 (continued)

<table>
<tr><td>Thickness of the gap</td><td> 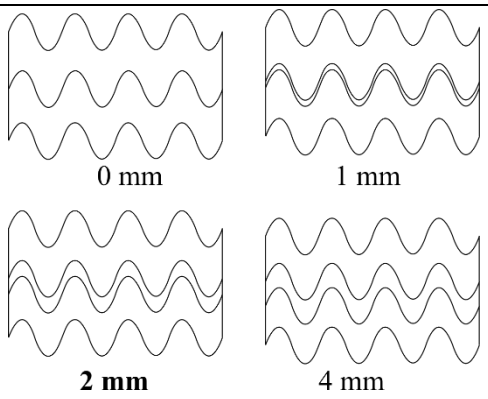
</td></tr>
<tr><td>Material properties of the wall</td><td>
<table>
<tr><th>Elastic modulus (GPa)</th><th>Wave speed, c_0 (m/s)</th></tr>
<tr><td>2</td><td>1000</td></tr>
<tr><td>8</td><td>2000</td></tr>
<tr><td>18</td><td>3000</td></tr>
<tr><td>32</td><td>4000</td></tr>
<tr><td>50</td><td>5000</td></tr>
</table>
</td></tr>
<tr><td>Type of the wall boundary</td><td> 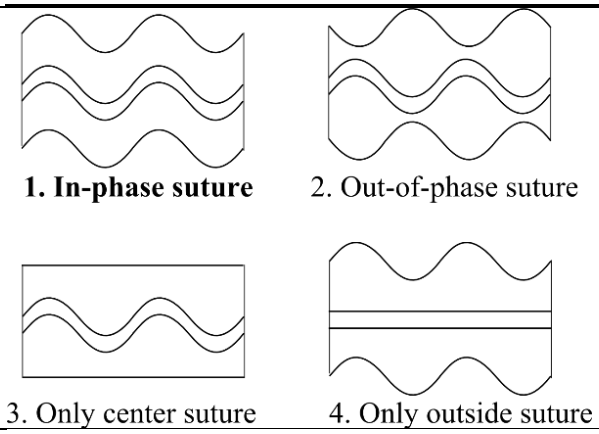
</td></tr>
<tr><td>Impulse amplitude</td><td> 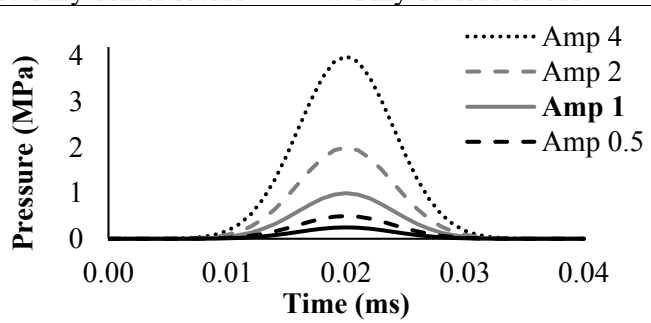
</td></tr>
</table>

Table 4.1 (continued)

Impulse duration	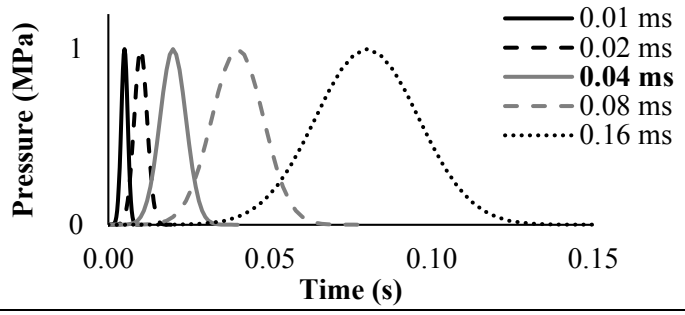

Design factors of suture interfaces and boundary conditions to evaluate their effects on damping; 1. Waviness of the suture 2. R_{suture}, the ratio of the suture height over the bar thickness, 3. Thickness of the gap, 4. Material properties of the elastic wall, 5. Type of the boundary, 6. Amplitude of the impact, and 7. Impact duration. The default values are in bold font.

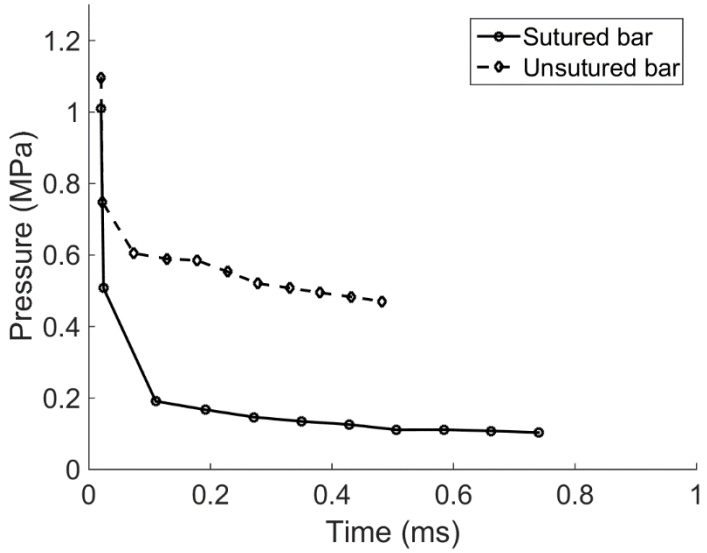

Figure 4.3 Pressure decay at the sutured and un-sutured bars.

Comparison of pressure recorded along the sutured bar and un-sutured bar. Each point is the peak pressure at the eleven regions. The initial impact was 1 MPa, and the pressure when stress waves reached to the end was 0.47 MPa at the un-sutured bar, and 0.1 MPa at the sutured bar.

4.3 Results and discussion

FE simulations were carried out by applying external mechanical loads to produce stress wave propagating in continuum media. We examined the damping capability of suture interfaces by comparing to un-sutured interfaces. Then, the design factors of suture interfaces such as geometric variations and boundary conditions were assessed for their influence in stress wave mitigation by parametric analyses.

4.3.1 Dissipation of stress waves at the sutured bar

A sutured bar was able to dissipated stress wave effectively compared to an un-sutured bar. Figure 4.3 shows the peak pressure decay in sutured vs. un-sutured bar. The peak pressure when the stress wave reached to the end of the bar was 0.47 MPa at the un-sutured bar, and 0.1 MPa at the sutured bar. The sutured bar response was 78.72 % less than that of the un-sutured bar.

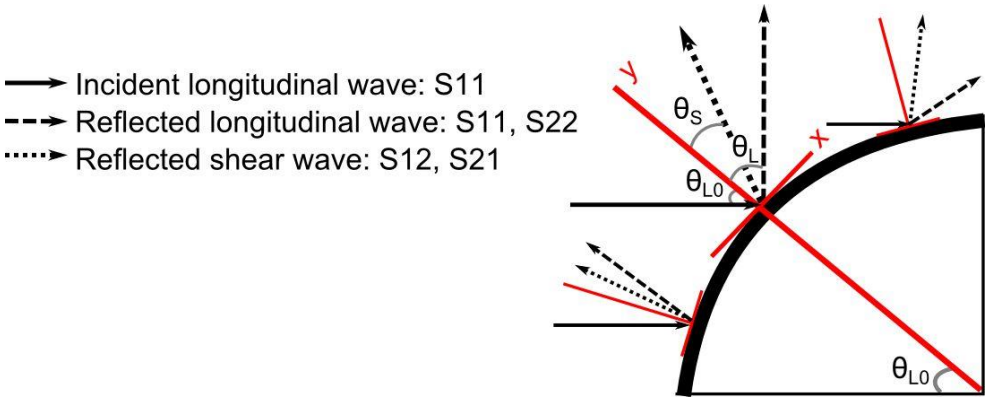

Figure 4.4 Wave reflection at boundary.

Reflection of compressive incidence at a curved boundary. Incident longitudinal wave with an angle of θ_{L0} reflected to a longitudinal wave with an angle of θ_L and a shear wave with an angle of θ_S.

There were two mechanisms associated with the sutured bar for stress wave mitigation as compared to the un-sutured bar. First, stress wave scattering occurred at the boundary of the sutured bar, in which compressive waves (S11) were converted into shear waves (S12) and into flexural waves (S22). In wave perspective, there are two basic types of wave motion for mechanical waves: longitudinal waves and shear waves (also called transverse waves). Displacements in longitudinal waves occur in a parallel direction to the wave propagation, and in transverse waves, displacements occur in a perpendicular direction (28). The waves to S11 and S22 are longitudinal waves, and the waves to S12 are shear waves.

Wave scattering is an interaction of waves with a boundary or obstacles in a medium resulting in wave reflection, transmission, or refraction (29). Since the compressive incidence impinged the sinusoidal interfaces, wave scattering can be considered reflection at a curved surface as described in Figure 4.4. The reflected waves consist of longitudinal and shear waves with an angle of θ_L and θ_S, respectively. According to DasGupta and Hagedorn (30) the wave scattering at boundaries can be defined as followed numerical expressions. Total wave field can be represented as following:

$$u(x,y,t) = A_{L0}\hat{n}_{L0}e^{i\kappa_{L0}\{x\ \sin\theta_{L0}+y\ \cos\theta_{L0}-C_L t\}} + A_L\hat{n}_L e^{i\kappa_L\{x\ \sin\theta_L-y\ \cos\theta_L-C_L t\}} + A_S\hat{a}\times\hat{n}_S e^{ik_S\{x\ \sin\theta_S-y\ \cos\theta_S-C_S t\}} \quad (4.3)$$

where u is displacement, t is the time, A is the amplitude, κ is the wave number, and θ is the angle between the waves and y axis in the Figure 4.4. L0, L, S are the incident waves,

reflected longitudinal waves, and reflected shear waves, respectively. The directions of waves are

$$\hat{n}_{L0} = \left(\sin\theta_L,\ \cos\theta_L\right)^T$$

$$\widehat{n}_L = \left(\sin\theta_L,\ -\cos\theta_L\right)^T$$

$$\widehat{n}_S = \left(\sin\theta_S,\ -\cos\theta_S\right)^T \tag{4.4}$$

Also, wave speed of longitudinal wave and shear wave are

$$C_L = \sqrt{\frac{E}{\rho(1+\gamma)}\left(\frac{1-\gamma}{1-2\gamma}\right)}$$

$$C_S = \sqrt{\frac{E}{2\rho(1+\gamma)}} \tag{4.5}$$

where E is a Young's modulus, γ is a Poisson ratio, and ρ is a density.

For given material properties in this study, C_L=2320.3 m/s, C_S=1240.3 m/s. With an assumption that a reflecting surface is a free surface, then the boundary conditions are as follows:

$$\sigma_{12}|_{y=0} = 0, \sigma_{22}|_{y=0} = 0 \tag{4.6}$$

The boundary conditions produce the following relationships.

$$\kappa_{L0}\sin\theta_{L0} = \kappa_L\sin\theta_L = \kappa_S\sin\theta_S$$
$$\mathrm{C_L\kappa_{L0}} = \mathrm{C_L\kappa_L} = \mathrm{C_S\kappa_s} \tag{4.7}$$

Then,

$$\theta_L = \theta_{L0},\ \theta_S = \frac{C_S}{C_L}\theta_{L0} \tag{4.8}$$

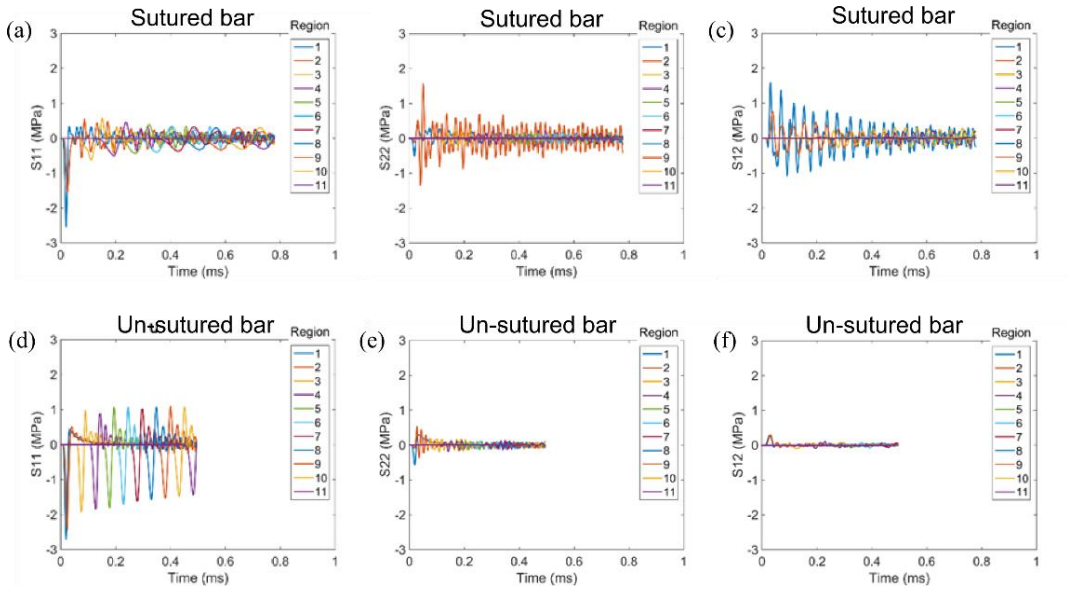

Figure 4.5 Stress at the sutured and un-sutured bar.

Stress waves at the eleven regions along the sutured bar of stress components of (a) S11, (b) S22, (c) S12, and along the un-sutured bar of stress components of (d) S11, (e) S22, and (f) S12. The stress wave graphed until the wave reached to the end of the structure. 0.78 ms for the sutured bar and 0.55 ms for the un-sutured bar.

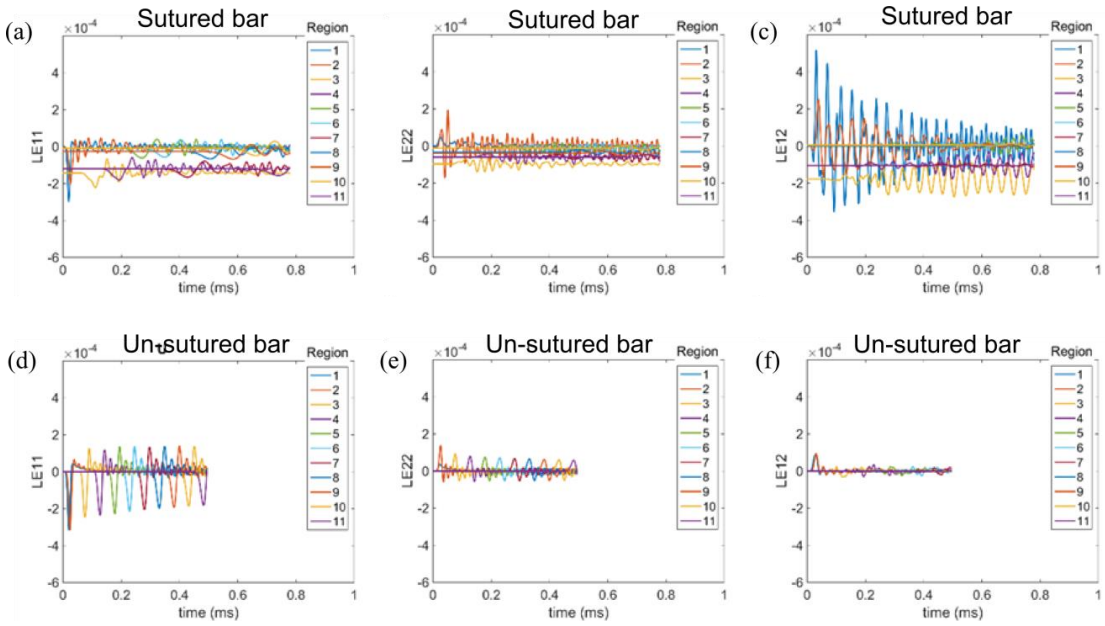

Figure 4.6 Strain at the sutured and un-sutured bar.

Strain at the eleven regions along the sutured bar of stress components of (a) LE11, (b) LE22, (c) LE12, and along the un-sutured bar of stress components of (d) LE11, (e) LE22, and (f) LE12.

For given conditions of this study, the angle of reflected longitudinal waves is the same as the angle of incident longitudinal waves. On the other hand, the angle of reflected shear waves are the 0.53 times of the angle of incident longitudinal waves.

As a result of wave scattering, at the suture interfaces, the magnitude of S11 decreased, and that of S12 and S22 increased in the sutured bar (Figure 4.5). The maximum S22 generated in the sutured bar is 1.58 MPa while that of the un-sutured bar is 0.54 MPa, and the maximum S12 generated in the sutured bar is 1.59 MPa while that of the un-sutured bar is 0.29 MPa. Not only does one see decay, but also wave dispersion due to the wave scattering. As shown in Figure 4.6, in the sutured bar, the pressure wave arrived to the free end at 0.78 ms while that of the un-sutured bar arrived at 0.55 ms. Accordingly, the sutured bar induced strain to the y direction (LE22) and shear strain (LE12). Figure 4.6 showed that the sutured bar induced strains to the y direction and shear direction, and decreasing a strain to the x direction. Figure 4.7 shows the maximum strain energy density at the sutured and un-sutured bar in Region-2 (near-front region) where the sinusoidal pattern begins so that the wave scattering occurred first. The peak strain energy was 0.09 J at the sutured bar, and 0.03 J at the un-sutured bar. The results in the sutured bar was about 3 times greater than that of un-sutured bar. Specifically, in the sutured bar, strain energy was stored in all directions of xx (17.73 %), yy (45.59), and xy (36.68 %) due to reflected stress waves, while in the un-sutured bar most of the strain energy stored only in xx direction (86.43 %).

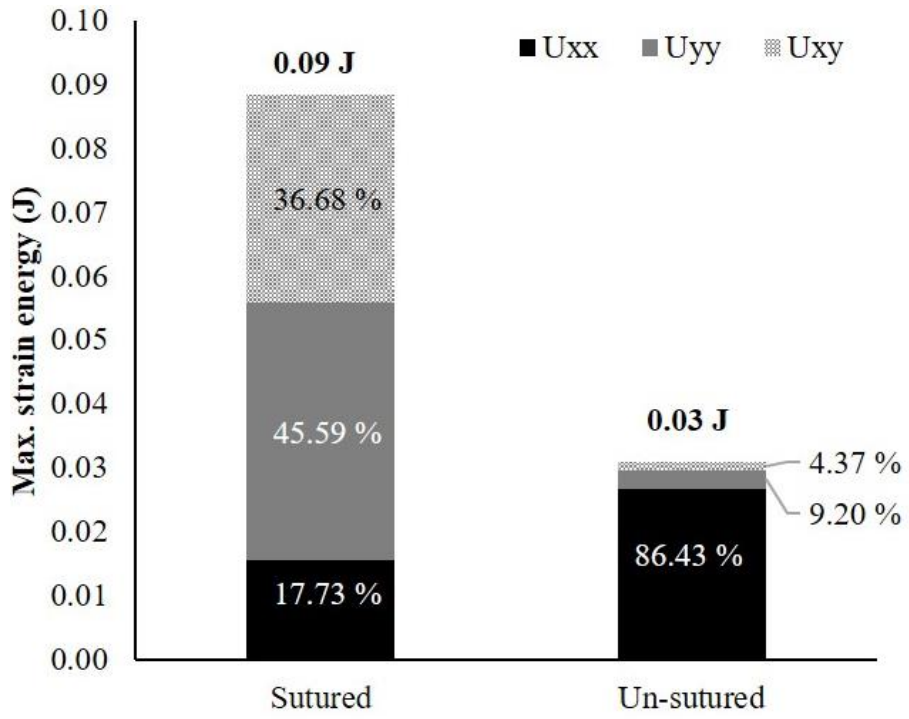

Figure 4.7 Maximum strain energy density

Maximum strain energy density in the region-2 (indicated in Figure 2(c)) which is near-front at the sutured and un-sutured bar. The total strain energy is greater at the sutured bar than that of the un-sutured bar.

Second, the mechanism of pressure decaying at the sutured bar was strain energy being stored in a viscoelastic suture gap. It is common to interweave viscoelastic layers between hard and stiff material to increase the damping of the structure (31-33), and biological material design has used the same strategy. Figure 4.8 shows the comparison of the strain energy of the gap between sutured and un-sutured bar. The viscoelastic gap material of the sutured bar allowed for strain energy to be stored, and it contributed to energy dissipation since the strain energy in viscoelastic material is proportional to the damping (34).

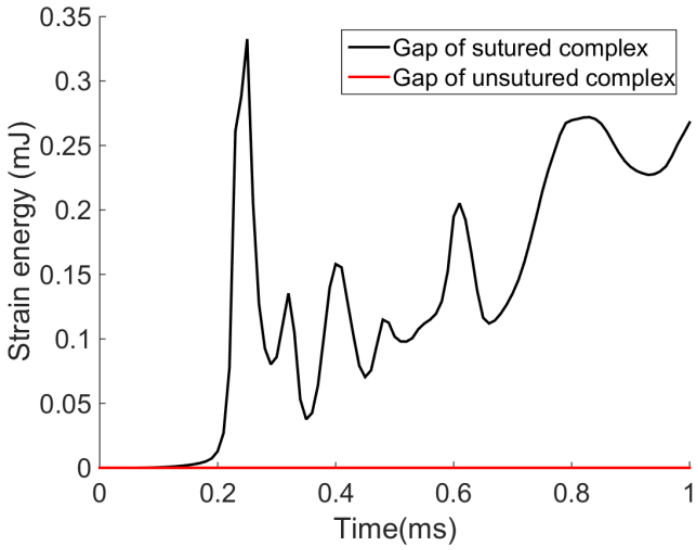

Figure 4.8 Strain energy of the gap

Strain energy occurring at the gap of the sutured bar (black) and of the un-sutured bar (red).

4.3.2 Design factors affecting to stress wave mitigation

A sinusoidal patterned interface caused stress redistribution, which led to wave attenuation, and wave dispersion. In order to examine design factors regarding a sinusoidal pattern and boundary conditions, the seven factors shown in Table 1 were investigated using finite element analysis. At each case, pressure decay as stress waves propagated along the bar was recorded. Also, compressive waves (S11), flexural waves (S22), and shear waves (S12) were plotted to evaluate the transformation of compressional stress into shear stress and flexural stress. Compressional waves were recorded when stress waves reached to the end, and both of maximum flexural waves and maximum shear waves were recorded while pressure traveled the structure. Generally, as flexural waves and shear waves increased, compressive waves decreased. As one factor changed, the other six factors were fixed with the default value indicated in Table 1.

4.3.2.1 The effect of the suture waviness

Waviness was varied in six cases of 0.25, 0.5, 0.75, 1, 1.25, and 1.5, in which the waviness height was fixed and the waviness width was changed. As the pressure waves travelled the sutured bar from the loading region to the free end, the magnitude of the pressure dropped when a suture was introduced (Figure 4.3). However, with a suture, there were minimal relationship between waviness and damping as shown in Figure 4.9(a). Figure 4.9(b) showed that generated shear stress had the highest value at waviness 0.5 and the generated flexural wave had the highest value at waviness 1. The highest conversion to shear stress and flexural stress led to less compressional stress at waviness 0.5 and 1.

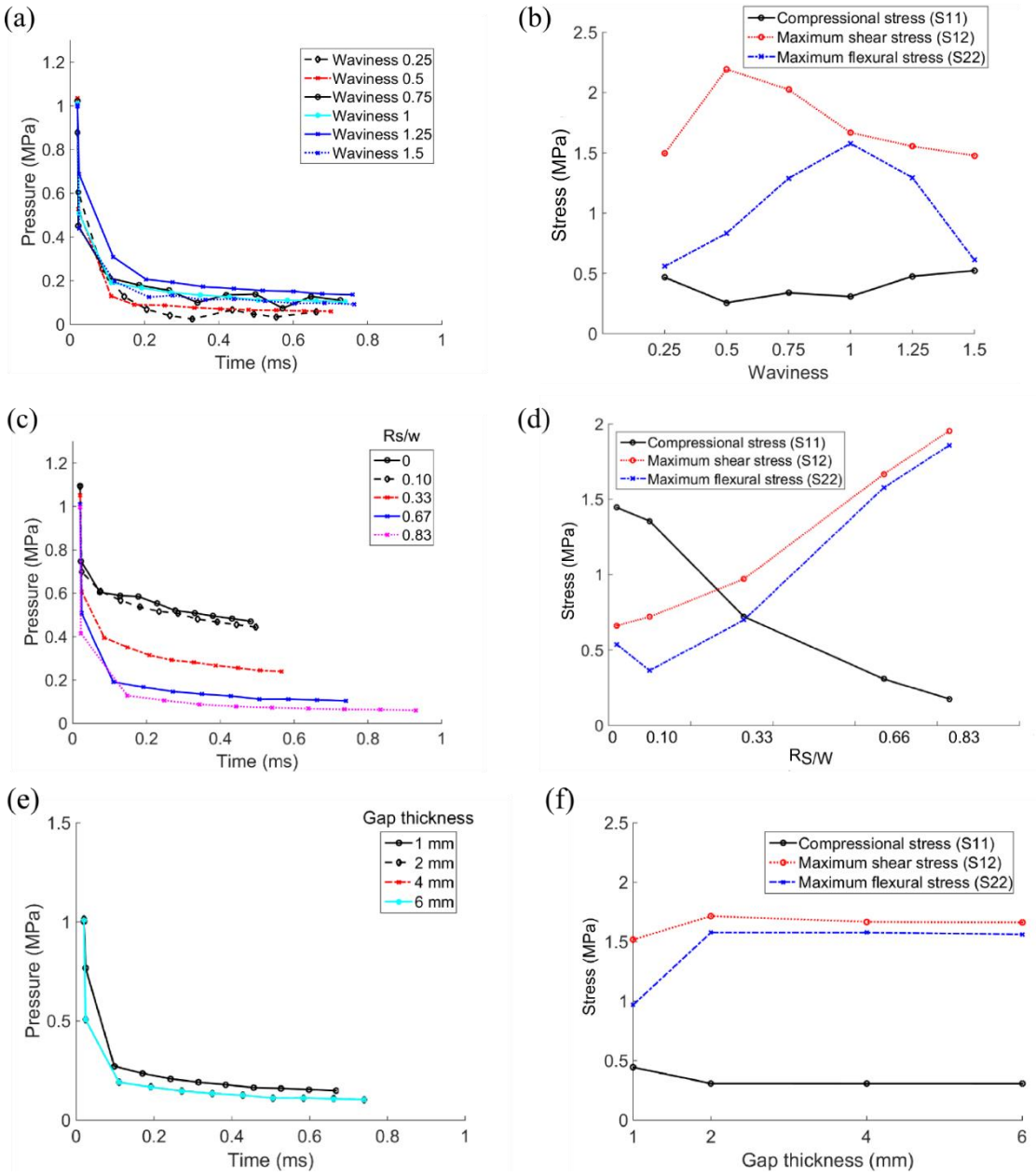

Figure 4.9 The effect of geometric factors and boundary conditions on stress wave dissipation

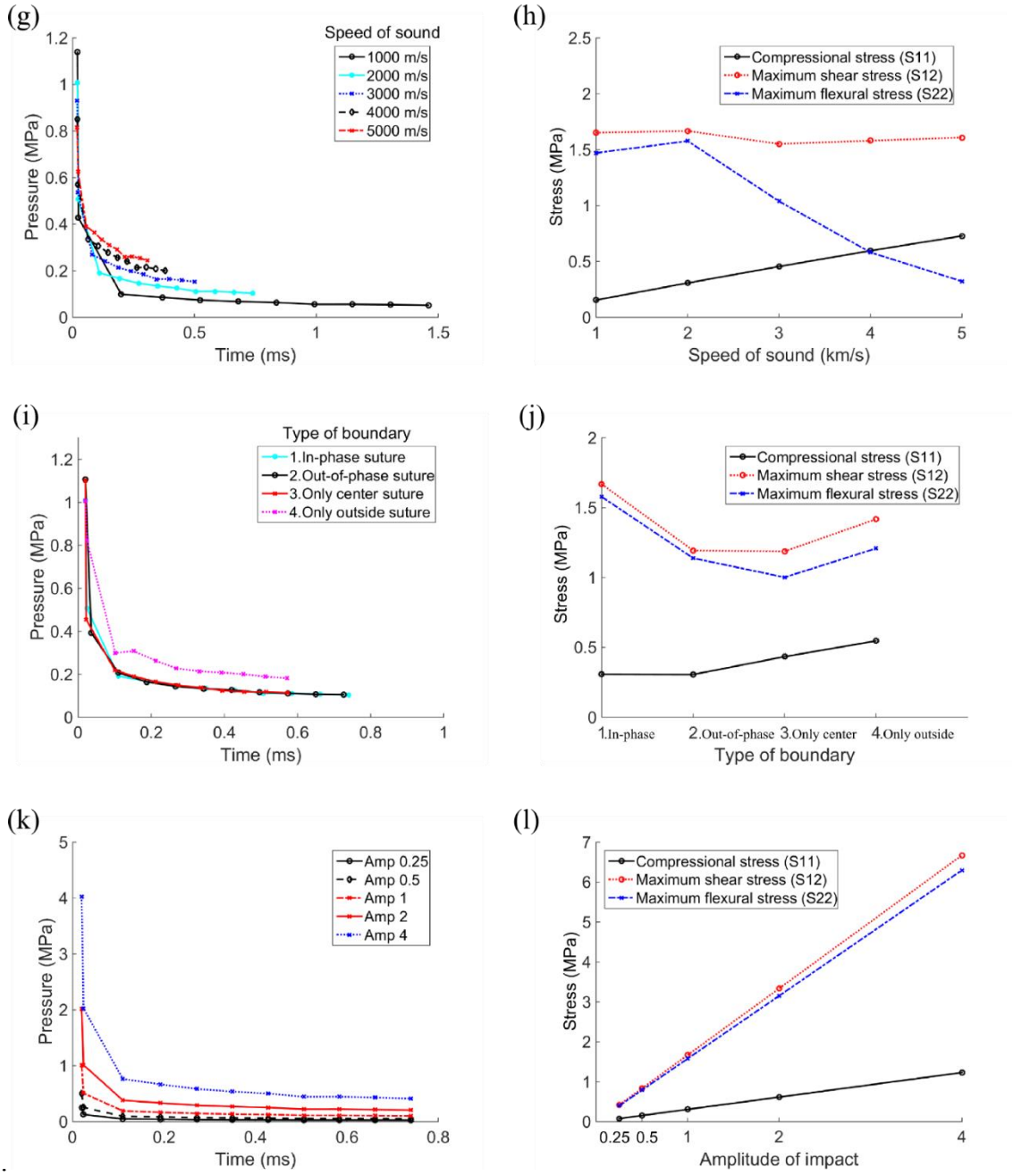

Figure 4.9 (continued)

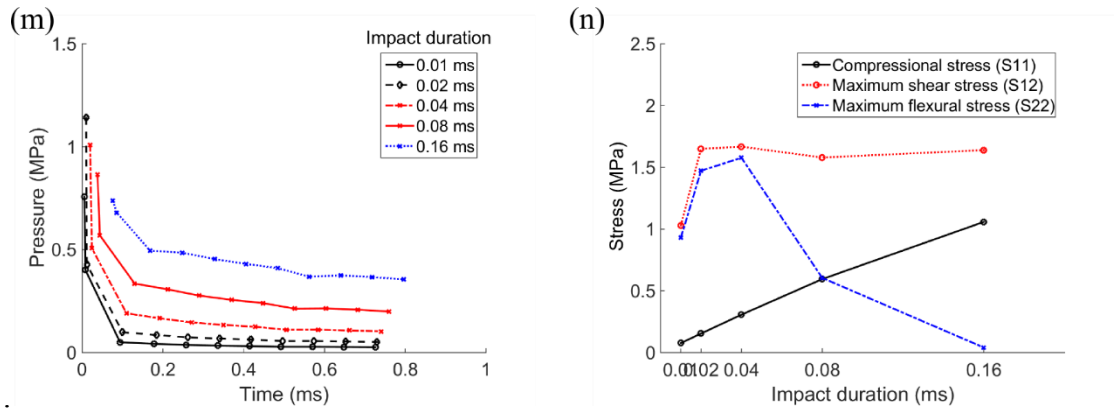

Figure 4.9 (continued)

Pressure wave decay as pressure waves traveled from the load applied region to the free end at the idealized bar with a suture interface, and compressional stress when the stress wave reaches to the free end, maximum shear stress and maximum flexural stress while pressure wave traveling at seven variables of (a), (b) waviness, (c), (d) R_{suture} which is the ratio of the suture height to the bar thickness, (e),(f) thickness of the gap, (g), (h) material properties, (i), (j) type of the wall boundary, (k), (l) amplitude of the loading, and (m), (n) impact duration.

4.3.2.2 The effect of the R_{suture}

The R_{suture} was changed as 0, 0.10, 0.33, 0.67, and 0.83. The height of the suture was changed as 0 mm, 1.5 mm, 5 mm, 10 mm, 12.5 mm while the bar thickness was fixed at 15 mm. As the R_{suture} increased, the pressure when the stress wave reached to the end of the bar decreased as shown in Figure 4.9(c). Figure 4.9(d) showed that higher R_{suture} induced more flexural stress and more shear stress so that compressional stress decreased.

4.3.2.3 The effect of the thickness of the gap

The sutured bars varied as gap thickness changed from 1 mm, 2 mm, 4 mm, and 6 mm. The thickness of the gap did not effect to the amount of the stress dissipation (Figure 4.9(e)) and did not show a big difference in inducing shear stress and flexural stress

(Figure 4.9(f)) although the 2 mm, 4 mm, 6 mm of the gap thickness had slightly more dissipation than the 1 mm gap.

4.3.2.4 The effect of the material properties

Material properties of the waveguide determines the sound speed as following:

$$c_0 = \sqrt{\frac{E}{\rho}} \tag{4.9}$$

In this study, five different elastic moduli were simulated; 2 GPa, 8 GPa, 18GPa, 32 GPa, and 50 GPa resulting in wave speeds of 1000 m/s, 2000 m/s, 3000 m/s, 4000 m/s, and 5000 m/s accordingly. The dissipation occurred greater as the wave speed decreased (Figure 4.9(g)), and also the time arriving at the end of the structure decreased. Figure 4.9(h) showed that the generation of shear wave was not affected by the wave speed while the generated flexural wave decreased as the wave speed increased. The compressional stress when the stress wave reached to the end of the bar increased proportionally with the wave speed.

4.3.2.5 Type of the wall boundary

The effect of the boundary was examined in-phase, out-of-phase, only center, and only outside boundaries. Figure 4.9(i) showed that there was no difference in damping amount and wave speed between in-phase and out-of-phase boundary. However, the substitution of the suture boundary to straight boundary increased wave speed no matter the center-line or outside edge. Also, the result showed that there was an interaction between suture and the gap for damping. Suture interfaces brought greater strain energy to the gap compared to flat interfaces as discussed in Figure 4.8. Hence, the damping of the bar with an only-outside-suture in which the suture-gap interaction was absent was

smaller than the other models. Figure 4.9(j) showed the stress transformation at the four types of boundary. Although the damping amount and the wave speed were similar in in-phase and out-of-phase, the maximum shear stress and the maximum flexural stress were greater at the in-phase boundary than those of out-of-phase boundary.

4.3.2.6 The effect of the amplitude of the impulsive loading

The amplitude of the impact loading was changed as 0.25, 0.5, 1, 2, and 4 to investigate the damping effects caused by an input condition of amplitudes. As the amplitude of impact increased, the pressure also increased. However, the damping amounts remained the same regardless of the amplitude of the loading as shown in Figure 4.9(k). Figure 4.9(l) showed that as the amplitude of the loading increased, the S11, S12, and S22 also increased.

4.3.2.7 The effect of the impact duration

The impact duration was changed as 0.01 ms, 0.02 ms, 0.04 ms, 0.08 ms, and 0.16 ms to investigate the damping effects resulted by an input condition of frequencies. Results showed that as the impact duration increased, lesser dissipation of the pressure waves occurred (Figure 4.9(m)), and the compressional stress converted less to the flexural stress (Figure 4.9(n)).

4.3.3 Damping quotient and phase velocity

The damping quotient and normalized phase velocity were evaluated to pick up variables affecting to the mitigation. Figure 10 showed correlation of each factor to the attenuation and dispersion of pressure waves.

Figure 4.10(a) and 4.10(b) showed the relationships between waviness and damping quotient/phase velocity. Because there was little relationship between waviness and damping quotient with a slope value of 0.04 (R2:45), and between waviness and phase velocity with a slope value of 0.07 (R2:91), the waviness was not considered as a factor affecting damping. R_{suture} versus damping quotient was illustrated in Figure 4.10(c) to show that the damping quotient was proportional to the R_{suture}. The damping quotient increased from 0.57 to 0.94 as the R_{suture} increased from 0 to 0.83. Also, the normalized phase velocity proportionally decreased as R_{suture} increased (Figure 4.10(d)). Jaslow (13) reported that the amount of energy absorbed may depend on the morphology of the suture, and our findings indicated that the amount of energy mitigation was more related to the R_{suture} rather than the waviness. Figure 4.10(e) and 4.10(f) showed that the thickness of the gap did not substantially affect to wave dissipation and dispersion. Figure 4.10(g) and 4.10(h) showed that the speed of sound determined by material properties resulted in changes in damping quotient and phase velocity proportionally. Regarding a type of boundary, there was no difference in damping quotient and phase velocity between in-phase suture and out-of-phase suture while absent of suture line led less attenuation and dispersion as shown in Figure 4.10(i) and 4.10(j). Figure 4.10(k) and 4.10(l) showed that the amplitude of the impact did not correlate to the damping quotient and phase velocity. Figure 4.10(m) and 4.10(n) indicated that the wave attenuation through the wavy geometry affected by impact duration, however the wave dispersion was not affected by it.

As a result, the three factors including R_{suture}, speed of sound, and impact duration affected to the damping quotient, and two factors including R_{suture}, speed of sound related to normalized phase velocity.

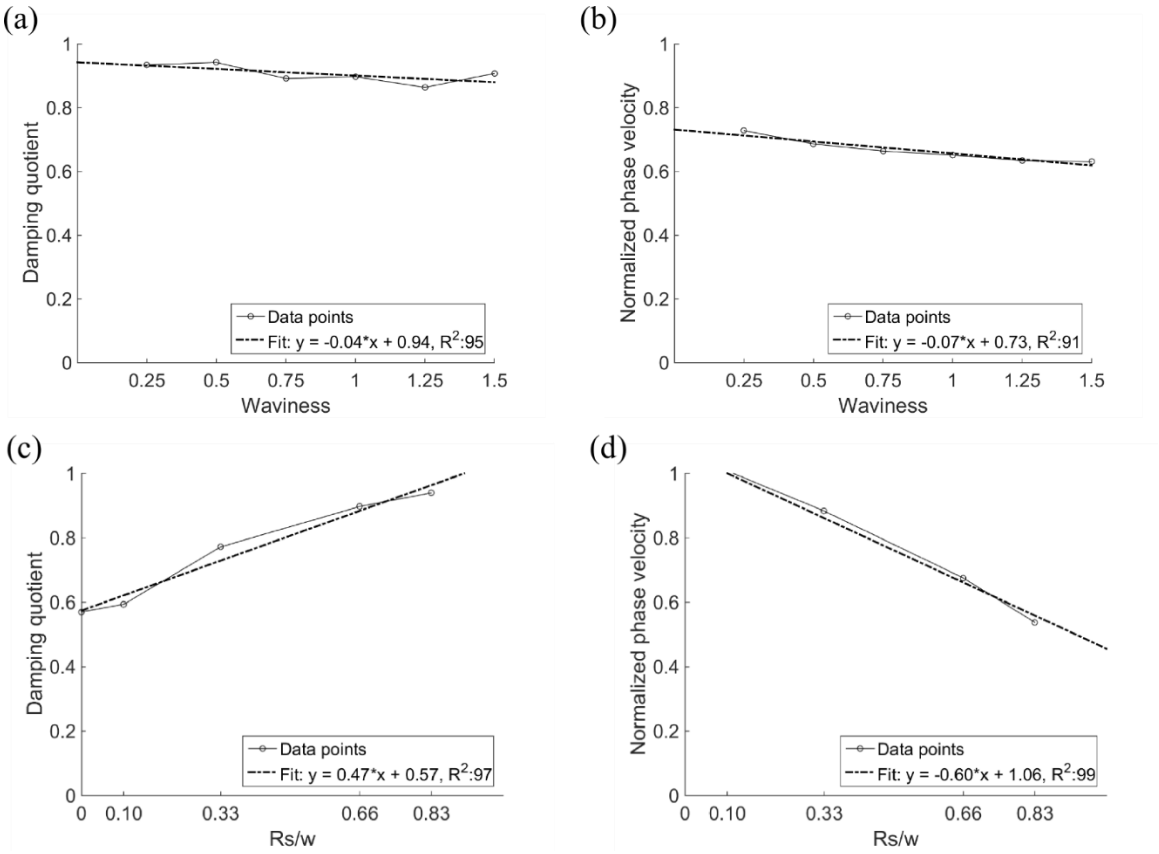

Figure 4.10 Damping quotient and normalized phase velocity at seven design factors

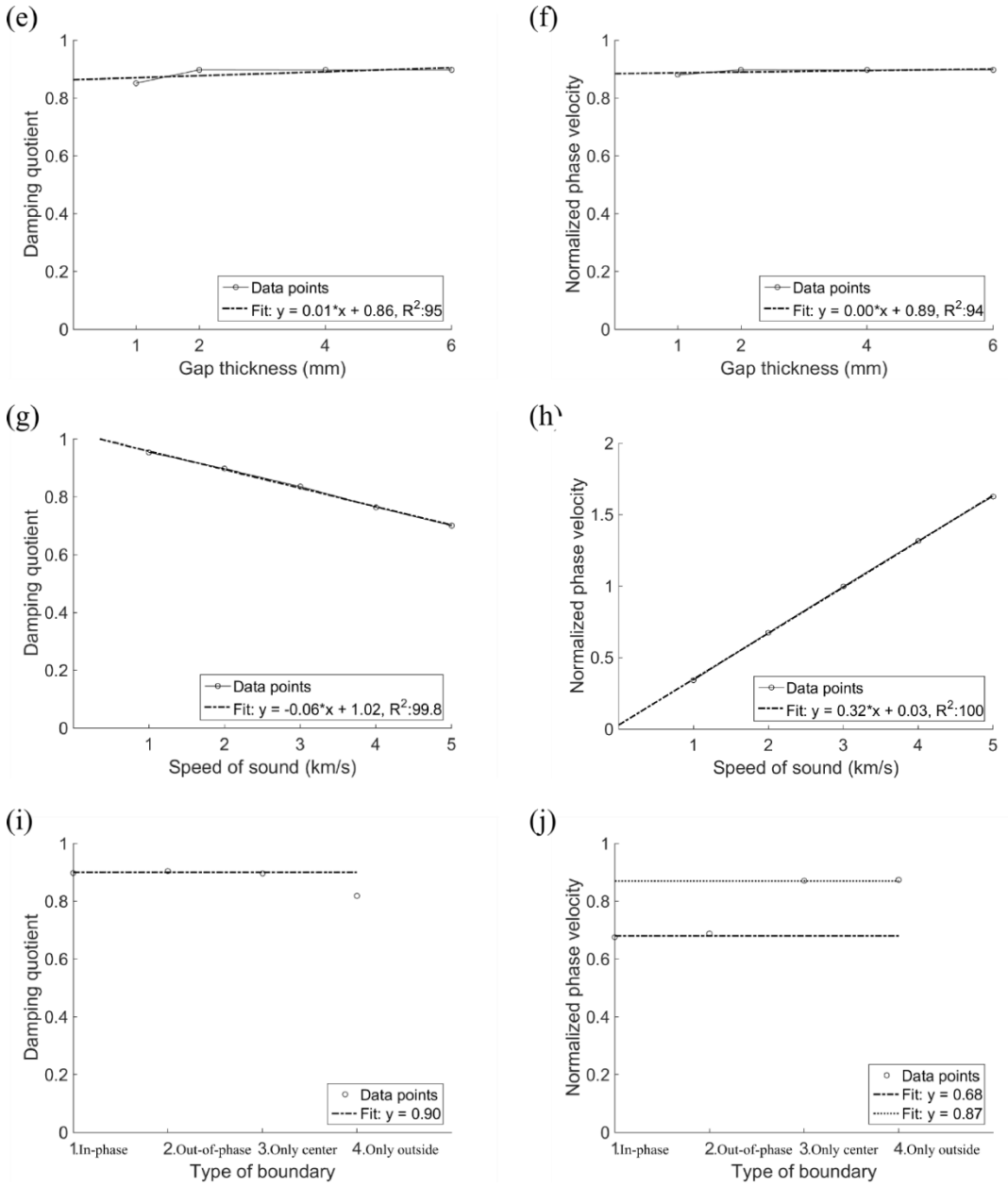

Figure 4.10 (continued)

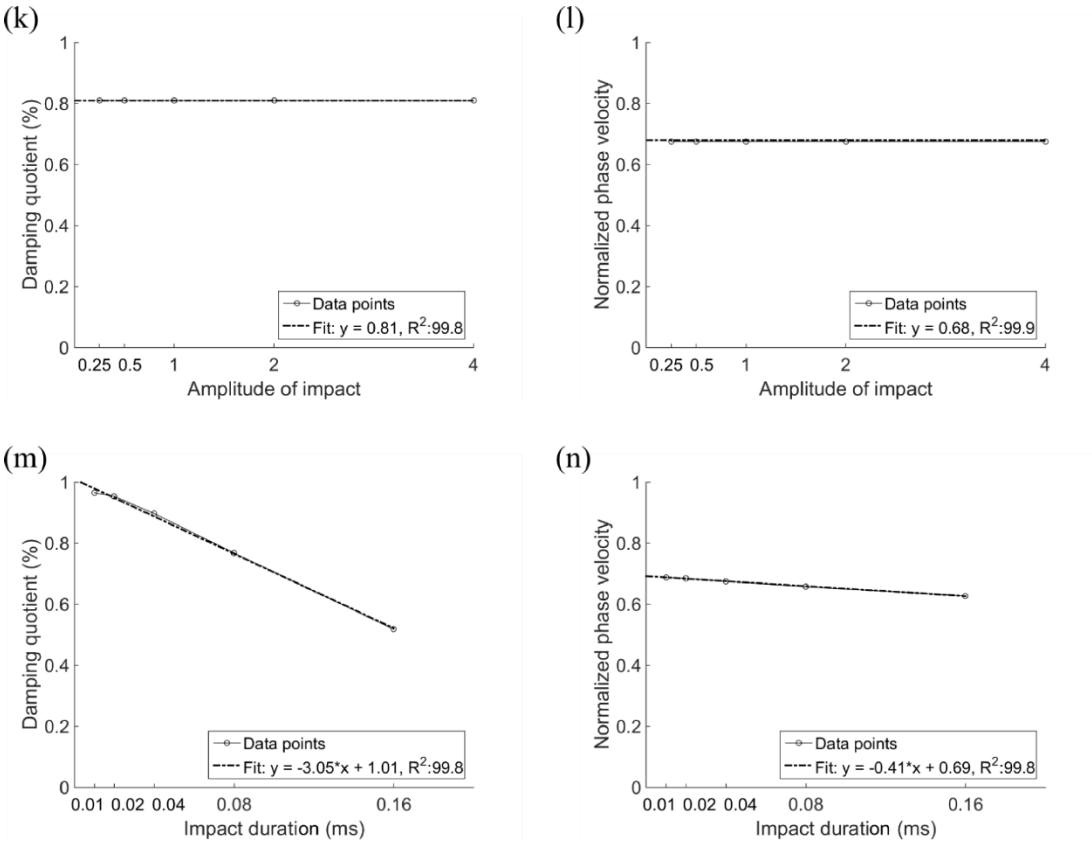

Figure 4.10 (continued)

The data points of the damping quotient with its associated the curve fit and the data points of the normalized phase velocity and the curve fitting at seven variables of (a), (b) waviness, (c), (d) R_{suture} (ratio of the suture height to the bar thickness), (e), (f) thickness of the gap, (g), (h) material properties, (i), (j) type of wall boundaries, (k), (l) loading amplitude, and (m), (n) impact duration.

4.4 Conclusions

One unique characteristic of biological materials is the effective use of elasticity for mitigating and dissipating energy. Although shock absorbers such as car bumper or guard rails are designed to absorb impact energy through plastic deformation, biological materials cannot use this strategy for absorbing the energy because severe plastic deformation could cause fatal damage. To keep structural integrity, biological material use elastic behavior effectively to mitigate stress wave, and sutures play a role to adopt

this strategy in biological materials: 1. suture interfaces induced shear waves and flexural waves from compressional waves so that elastic deformation occurs to the not only xx direction but yy and xy directions. 2. The interaction between viscoelastic material in the gap and suture geometry led to stress wave damping.

In addition, we investigated design variations of suture interfaces and boundary conditions to evaluate their correlation to damping. As a result, there were three factors increasing wave attenuation; high ratio of the suture height to the bar thickness, low sound speed determined by material properties, and short external impact duration. The factors causing wave dispersion were high ratio of the suture height over the bar thickness, and low sound speed. The ratio of the suture height over the bar thickness was the only design factor to consider in cases where the material properties and impact duration could not be controlled.

The results of this work demonstrate a biological design of energy dissipation mechanisms in sutures that can be applied for the development of vibration isolation methods.

4.5 References

1. Lee N, Horstemeyer M, Rhee H, Nabors B, Liao J, Williams LN. Hierarchical multiscale structure–property relationships of the red-bellied woodpecker (Melanerpes carolinus) beak. Journal of The Royal Society Interface. 2014;11(96):20140274.

2. Allen E. Understanding Ammonoid Sutures: New Insight into the Dynamic Evolution of Paleozoic Suture Morpholog. Cephalopods Present and Past: New Insights and Fresh Perspectives. 2007:159-80.

3. Allen EG. New approaches to Fourier analysis of ammonoid sutures and other complex, open curves. Paleobiology. 2006;32(2):299.

4. Ubukata T, Tanabe K, Shigeta Y, Maeda H, Mapes RH. Eigenshape analysis of ammonoid sutures. Lethaia. 2010;43(2):266-77.

5. De Blasio FV. The role of suture complexity in diminishing strain and stress in ammonoid phragmocones. Lethaia. 2008;41(1):15-24.

6. Krauss S, Monsonego Ornan E, Zelzer E, Fratzl P, Shahar R. Mechanical Function of a complex three dimensional suture joining the bony elements in the shell of the red eared slider turtle. Advanced Materials. 2009;21(4):407-12.

7. Chen IH, Yang W, Meyers MA. Leatherback Sea Turtle Shell: A Tough and Flexible Biological Design. Acta biomaterialia. 2015.

8. Behrents RG, Carlson DS, Abdelnour T. In vivo analysis of bone strain about the sagittal suture in Macaca mulatta during masticatory movements. Journal of Dental Research. 1978;57(9):904-8.

9. Byron CD. Role of the osteoclast in cranial suture waveform patterning. The Anatomical Record Part A: Discoveries in Molecular, Cellular, and Evolutionary Biology. 2006;288A(5):552-63.

10. Curtis N, Jones M, Evans S, O'Higgins P, Fagan M. Cranial sutures work collectively to distribute strain throughout the reptile skull. Journal of The Royal Society Interface. 2013;10(86).

11. Herring SW, Teng S. Strain in the braincase and its sutures during function. American Journal of Physical Anthropology. 2000;112(4):575.

12. Hubbard RP, Melvin JW, Barodawala IT. Flexure of cranial sutures. Journal of biomechanics. 1971;4(6):491-2, IN1-IN3, 3-6.

13. Jaslow CR. Mechanical propertise of cranial sutures. J Biomechanics. 1990;23(4):313-21.

14. Opperman LA. Cranial sutures as intramembranous bone growth sites. Developmental dynamics. 2000;219(4):472-85.

15. Seimetz CN, Kemper AR, Duma SM. An investigation of cranial motion through a review of biomechanically based skull deformation literature. International Journal of Osteopathic Medicine. 2012;15(4):152-65.

16. Sun Z, Lee E, Herring SW. Cranial sutures and bones: growth and fusion in relation to masticatory strain. The Anatomical Record Part A: Discoveries in Molecular, Cellular, and Evolutionary Biology. 2004;276(2):150-61.

17. Yu JC, Borke JL, Zhang G. Brief synopsis of cranial sutures: Optimization by adaptation. Seminars in Pediatric Neurology. 2004;11(4):249-55.

18. Li Y, Ortiz C, Boyce MC. Stiffness and strength of suture joints in nature. 2011.

19. Lin E, Li Y, Ortiz C, Boyce MC. 3D printed, bio-inspired prototypes and analytical models for structured suture interfaces with geometrically-tuned deformation and failure behavior. Journal of the Mechanics and Physics of Solids. 2014;73:166-82.

20. Lin E, Li Y, Weaver JC, Ortiz C, Boyce MC. Tunability and enhancement of mechanical behavior with additively manufactured bio-inspired hierarchical suture interfaces. Journal of Materials Research. 2014;29(17):1867-75.

21. Li Y, Ortiz C, Boyce MC. A generalized mechanical model for suture interfaces of arbitrary geometry. Journal of the Mechanics and Physics of Solids. 2013;61(4):1144-67.

22. Li Y, Ortiz C, Boyce MC. Bioinspired, mechanical, deterministic fractal model for hierarchical suture joints. PHYSICAL REVIEW E Phys Rev E. 2012;85:031901.

23. Li B-W, Zhao H-P, Qin Q-H, Feng X-Q, Yu S-W. Numerical study on the effects of hierarchical wavy interface morphology on fracture toughness. Computational Materials Science. 2012;57:14-22.

24. Maloul A, Fialkov J, Wagner D, Whyne CM. Characterization of craniofacial sutures using the finite element method. Journal of biomechanics. 2014;47(1):245-52.

25. Zhang Z, Yang J. Biomechanical Dynamics of Cranial Sutures during Simulated Impulsive Loading. Applied Bionics and Biomechanics. 2015;2015.

26. Cheng T, Gan RZ. Mechanical properties of stapedial tendon in human middle ear. Journal of Biomechanical Engineering. 2007;129(6):913-8.

27. Bosboom E, Hesselink M, Oomens C, Bouten C, Drost M, Baaijens F. Passive transverse mechanical properties of skeletal muscle under in vivo compression. Journal of biomechanics. 2001;34(10):1365-8.

28. Graff KF. Wave motion in elastic solids: Courier Dover Publications; 1975.

29. Brekhovskikh LM, Goncharov V. Mechanics of continua and wave dynamics: Springer Science & Business Media; 2012.

30. DasGupta A, Hagedorn P. Vibrations and waves in continuous mechanical systems. Wiley, New York; 2007.

31. Berthelot J-M, Assarar M, Sefrani Y, El Mahi A. Damping analysis of composite materials and structures. Composite Structures. 2008;85(3):189-204.

32. Saravanos D, Pereira J. Effects of interply damping layers on the dynamic characteristics ofcomposite plates. AIAA journal. 1992;30(12):2906-13.

33. Cupiał P, Nizioł J. Vibration and damping analysis of a three-layered composite plate with a viscoelastic mid-layer. Journal of Sound and Vibration. 1995;183(1):99-114.

34. Plunkett R. Damping analysis: an historical perspective. ASTM special technical publication. 1992 (1169):562-9.

CHAPTER V

CONCLUSIONS

This study examined the structure-properties relationships of a woodpecker's beak and stress wave mitigation at woodpecker's hyoid apparatus and suture interfaces in order to find engineering principles that woodpeckers use for stress wave dissipation. The beaks of the Red-Bellied Woodpecker (*Melanerpes carolinus*) shows complicated multiscale heterogeneous structure. The woodpeckers' beaks are a structural biocomposite having three layers; rhamphotheca (outer keratin shell), middle foam layer, and inner bony layer. Along the beak from posterior to anterior, the area fraction of these three layers gradually changes, so the aggregate modulus and aggregate hardness are gradients. Additionally, the three main design factors associated with stress wave dissipation were pointed out. First, a woodpecker's beak has wavy lines inside of the beak to admit local shearing. The waviness of wavy lines found in the woodpecker's beaks was 1, which is higher than one in chicken (0.3) and one in toucan (0.05). Second, the woodpecker showed elongated the keratin scales to the pecking direction that can slide over each other to generate friction. The dimension ratio of a woodpecker's keratin scales is 3.67 (width/height) while chicken's and toucan's were 3 and 1, respectively. Third, a woodpecker's beak bone was less porous to maintain structural strength. The porosity of a woodpecker's beak bone was about 9.9 % while chicken's and toucan's were 42.3 % and 61.5 %, respectively.

A hyoid apparatus, one of the unique anatomical features found in a woodpecker's head, was examined for its damping capacity. The results of the study show that the woodpecker's hyoid apparatus is an effective device in mitigating pressure waves and transferring the energy to adjacent muscle for energy dissipation. Although it is a small component of the woodpecker's skeletal system, its role is critical for the woodpecker's safety. Because of the geometrical structure of a hyoid apparatus, the initial impulse from the strike into a tree decreased 84% when it arrived at the hyoid end. Normal (longitudinal) impact waves transformed to transverse waves because (1) the cross-sectional area decreases and (2) the structure's curvature from the tip to the end thus inducing shear stresses to the lateral displacements into the dissipating muscle. The force exerted into the muscle generated strain energy within the viscoelastic muscle, which then dissipated the impact energy.

Another unique geometry found in woodpecker's beak is a suture-like wavy structure. This wavy structure has a sinusoidal pattern, and it is found in other biological materials such as skull, turtle shell, box fish, and ammonoid fossil, where two stiff components contact. This study found that sutures use the following strategies for stress wave dissipation: 1. inducing shear waves and flexural waves from compressional waves by wave scattering, and 2. damping caused by the interaction between viscoelastic material in the suture gap and wavy geometry led to. Then, design factors and boundary conditions were analyzed for their correlations to damping. The results of the parametric study show that there were three factors that affects to wave attenuation; high ratio of the suture height over the bar thickness, slow sound speed determined by material properties, and short impact duration. For wave dispersion, there were two factors; high ratio of the

suture height over the bar thickness, and short speed of sound. In the case the material properties and impact duration cannot be controlled, then ratio of the suture height over the wall thickness was the only design factor to consider.

As a result, it is concluded that woodpeckers use elasticity efficiently for mitigating and dissipating stress wave. Although shock absorbers such as car bumpers or guard rails are designed to absorb impact energy through plastic deformation, biological materials cannot use this strategy for absorbing energy because severe plastic deformation causes fatal damages. Keeping structural integrity, woodpeckers uses elastic deformation effectively to lower the directional stress level in structures by using viscoelastic material properties or using local shearing.

The results of this work demonstrate a biological design of energy dissipation mechanisms that can be implemented for developing vibration isolation method. In particular, the principles found in woodpeckers can be applied for some electronic devices being sensitive to mechanical impact such as smartphones or laptops, which are used repeatedly on daily basis and cannot have plastic deformable energy absorbing part.

CHAPTER VI

FUTURE WORKS

6.1 Whole head simulation of a woodpecker

The speed of a woodpecker's peck is approximately 6~7 m/s (1). In spite of the high speed and high frequency impacts, a woodpecker head remains structurally intact by efficiently dissipating the impact energy. Research shows that the primary features protecting the woodpecker's head from high impact include the beak with elongated keratin scales, wavy suture-like structure, and the spongy bone in the upper beak, the small brain being tightly enclosed within the skull, and the cranial bone shaped like a plate with high strength (2-6).

Along with unique physical features of a woodpecker head, in order to investigate how the stress waves propagate and dissipate at the woodpecker skull to protect the brain, a 3D finite element model of the woodpecker head was built. From this study, some mechanisms for reducing a stress wave can be learned.

6.1.1 Simulation setup

The DICOM image volume was imported into ScanIP (Simpleware Ltd, United Kingdom), which yielded a voxel size of 0.089468 mm x 0.089468 mm and slice spacing of 0.089468 mm. The ScanIP thresholding algorithm generated an initial mask of the entire woodpecker head and neck. However, most of the cervical vertebrae and surrounding neck tissue were removed manually in order to reduce the mesh size.

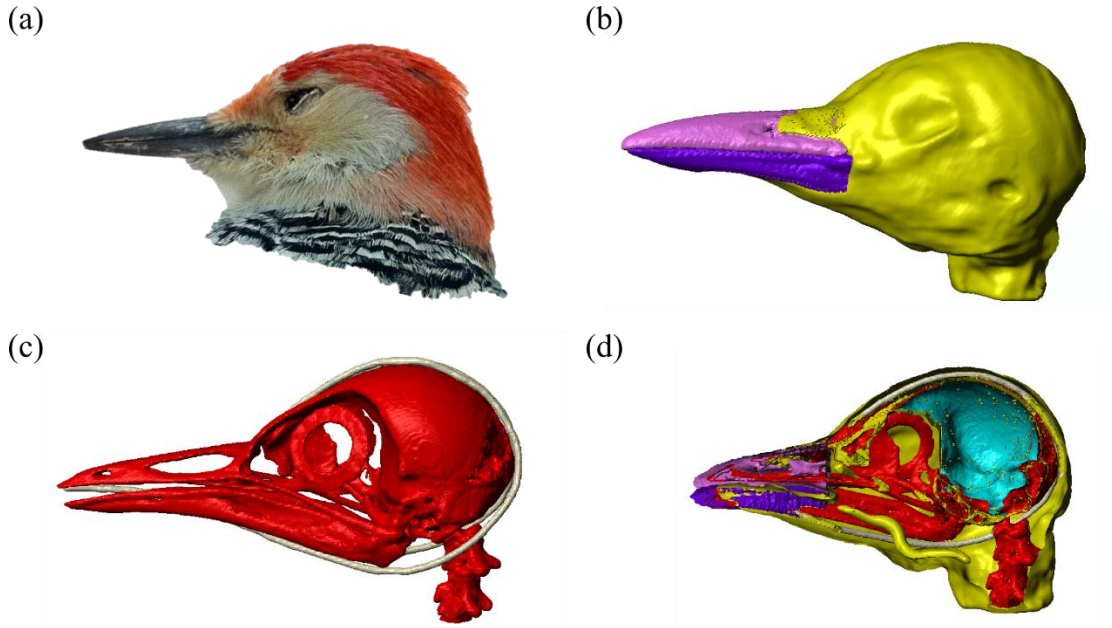

Figure 6.1 3D model of the woodpecker's head reconstructed from the Red-Bellied woodpecker's head.

(a) The woodpecker's head used for three-dimensional reconstruction. (b) The external of the woodpecker head model in mid-sagittal view generated in the software of ScanIP. (c) Skeletal system of the woodpecker's head including a skull (red) and a hyoid bone (white). (d) The internal structure includes the brain (cyan), bone (red), beak (light/dark purple), and scalp/muscle (yellow).

Furthermore, the recursive Gaussian filter smoothed the mask by subsequently removing any remaining imaging artifacts. The head comprised multiple layers that included the brain, bone, beak, and scalp/muscle. The beaks consisted of exterior keratin and inner bone. Figure 6.1(a) shows a real woodpecker head, and Figure 6.1(b-d) shows the different layers that constitute the woodpecker head generated in ScanIP. Figure 6.1(b) shows exterior of the woodpecker's head, Figure 6.1(c) shows skeleton structure of the woodpecker head with skull bone and a hyoid bone, and Figure 6.1(d) shows the internal structure with a brain.

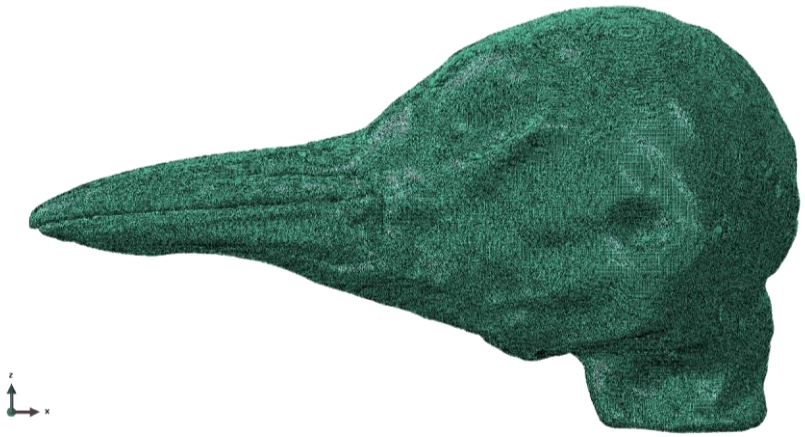

Figure 6.2 The mesh of the woodpecker's head.

Tetrahedral and quadratic elements were used for meshing to simulate pressure wave propagation in the woodpecker's head.

The woodpecker head model was meshed using approximately four million quadratic tetrahedral elements. The meshed woodpecker head model imported into Abaqus/cae is shown in Figure 6.2.

6.1.2 Anticipated results

The micro-CT images of the woodpecker's head shows that there are a lot of porous structures in the skull (Figure 6.3). Figure 6.4 shows that the micrographs of the porous area is a type of closed-cell foam. Hypothetically, the computational simulation will show stress re-distribution or pressure decay at this porous region.

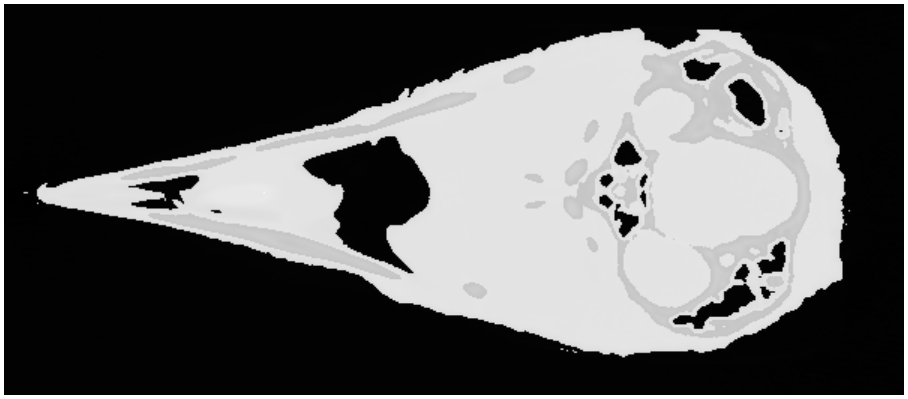

Figure 6.3 Micro-CT image of a woodpecker's head.

Micro-CT image shows that there are lots of porous areas inside of a woodpecker's skull.

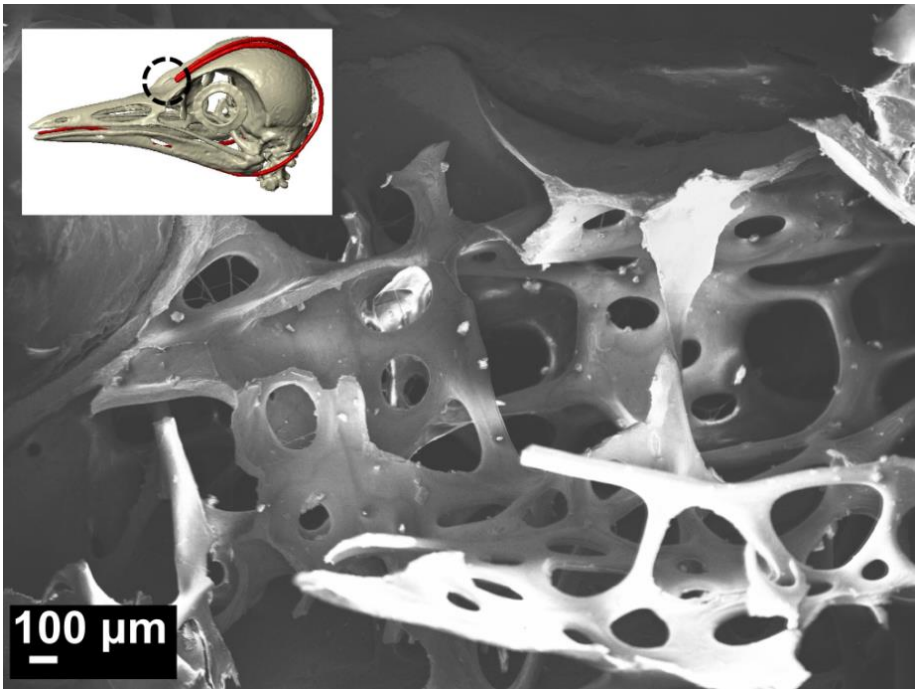

Figure 6.4 SEM image of the porous bone near root of a woodpecker's upper beak

SEM graph shows that the bone near upper beaks' root consists of closed-cell type of foam structure.

6.2 Friction coefficient of keratin scales of a woodpecker's beaks

A woodpecker's beaks are constituted of three layers; outmost keratin layer which anatomical name is rhamphotheca, middle foam layer, and innermost bony layer. This study pays attention to the outermost keratin layer. The keratin layer is composed of keratin scales which is made of β-keratin. The thin keratin scales with thickness is about 0.2 μm stacks up. The surface of the keratin scales is rough as shown in Figure 6.5.

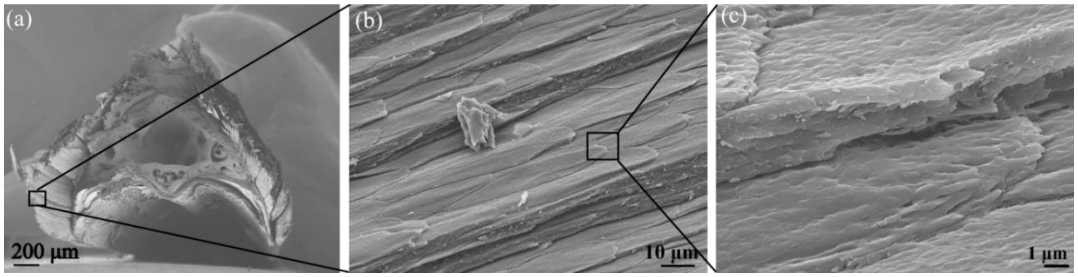

Figure 6.5 The outer layer of a woodpecker's beaks, rhamphotheca, composed of keratin scales

(a) Fractured surface of a woodpecker's beak. (b) Keratin scales placed in staggered pattern and stacks up. (c) The rough surface of keratin scales enhancing friction between scales.

The hypothesis of this research is that a woodpecker's beak dissipates the energy by friction between keratin scales. To examine this working hypothesis, one can use micro-tribometer to measure a friction coefficient between keratin scales. Also, by using micro-impact testers, one can measure how stress waves generate, propagate, and dissipate at rhamphotheca.

One of the expected result is anisotropy of friction coefficient of a keratin scale. Since the keratin fiber's running direction is to the longitudinal direction as shown in Figure 6.6, and the stress in the direction of pecking(longitudinal) is much higher than

transverse, the keratin scale would have different friction coefficient between longitudinal and transverse direction. Additionally, the elongated geometry of a keratin scale would bring more efficient friction to the pecking direction.

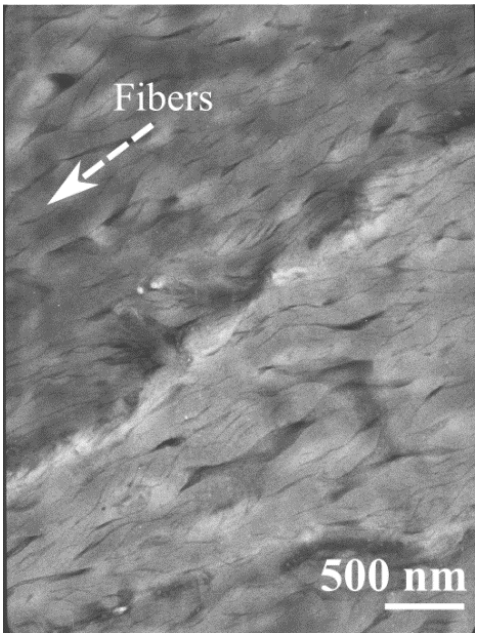

Figure 6.6 TEM image of keratin fibers in a woodpecker's beaks

TEM image of keratin fibers shows its running direction.

After obtaining experimental data, the friction coefficient of a woodpecker's beak keratin can be incorporated possibly for modeling using Coolong friction which is a standard friction. When a solid material undergoes deformation, internal friction occurs which is the force resisting motion between the grain boundaries. In the beak of a woodpecker, the keratin scales can act like a grain boundary while generating internal friction.

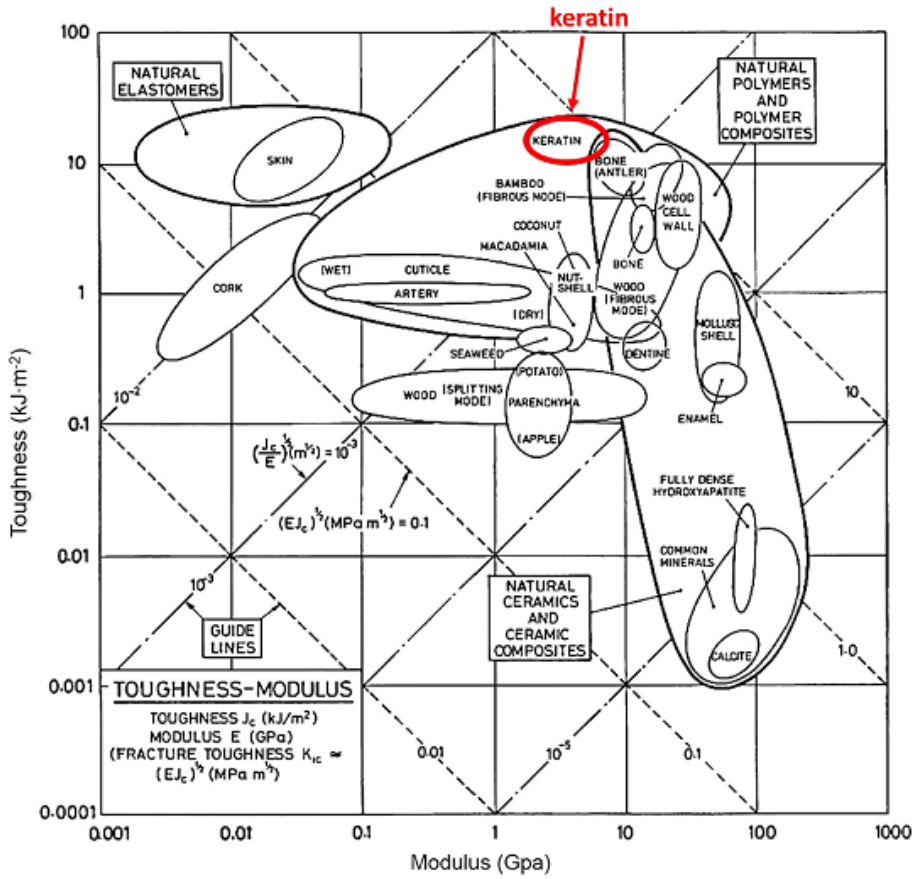

Figure 6.7 Toughness versus Young's modulus for biological materials (9).

This chart shows that the keratin is one of the material having both of high modulus and high toughness.

6.3 Keratin for bio-inspiration of covering coating

Keratin is one of the most common protein found in biomaterials (7). In particular, keratin is usually found at the solid shell-like part of living creatures' exterior. For example, keratin consists of a ram horn, bird beaks, a horse hoof, skin, and hair. Keratinous material covering a bone or skin plays roles to protect inner structures from not only moisture but also mechanical fragmentation (8). Although mechanical properties of keratin are affected by moisture, keratin is hydrophobic material to protect inner

structures from water. Also, the keratin having viscoelastic material behavior has high fracture toughness resisting crack propagation (Figure 6.7).

For the beak keratin, the microstructure of keratin is designed for prohibiting crack propagation. The staggering and stacking placement of keratin scales in avian beaks enhances its toughness and enables it to resist flaws. Also, the structure of keratin scales has a function of mitigate the stress wave energy.

A study of hierarchical structure-properties relationships of keratin would contribute to developing future covering materials for sensitive electronic devices.

6.4 Wave reflection and Fibonacci structure

One of the famous numbers is 1.618, known as Golden number or Fibonacci number. The Fibonacci sequence is the series of numbers: 0, 1, 1, 2, 3, 5, 8, 13, 21, 34... The next number is found by adding up the two numbers before it. 1.68 is the ratio between one number and the next number in Fibonacci sequence. Using Fibonacci number, the Fibonacci spiral can be drawn, and nature includes many examples following the Fibonacci spiral such as seashell or pine cone. As shown in Figure 6.9, a woodpecker's hyoid bone also interestingly follows the Fibonacci spiral.

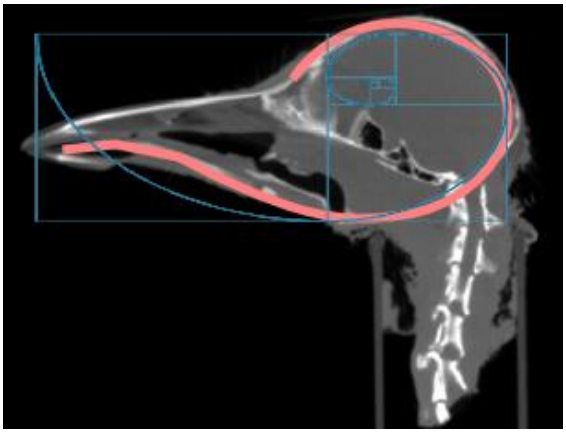

Figure 6.8 A woodpecker's hyoid bone and Fibonacci spiral.

The ram's horn also follows the Fibonacci number. The analysis of the tapered structure of horn shows that its cross-sectional area follows the rule of Fibonacci. The dimensions of regions shown in Figure 6.10 were measured and the ratio calculated. Figure 6.11 illustrates that the cross-sectional area of the ram's horn is increased proportionally, and Table 6.1 shows the ratio of the increasing cross-sectional area is about 1.6, which is close to Fibonacci number.

Since both of woodpecker's hyoid and ram's horn are involved in stress wave dissipation, a hypothesis can be built that the Fibonacci number is related to wave damping. However, additional studies are warranted in this area.

Figure 6.9 Ram's horn and numbering for dimension analysis

The cross-sectional dimension of the ram's horn was analyzed at the spot of numbering.

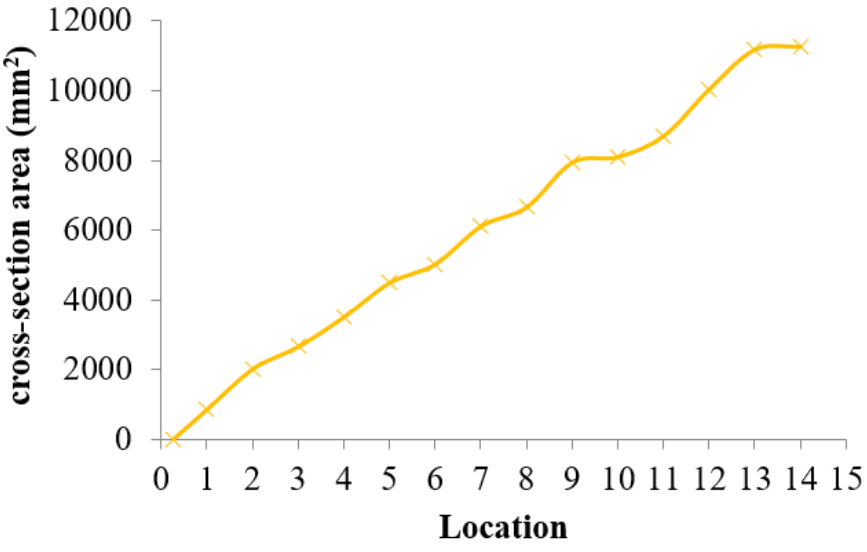

Figure 6.10 Analysis the cross-sectional area of a ram's horn

Tapering structure of a ram's horn was analyzed. The cross-sectional area of the ram's horn increases proportionally.

Table 6.1 The analysis of the cross-sectional area of a ram's horn

Location	1	2	3	4	5	6	7	8	9
Major axis	25.72	35.75	40.35	45.4	51.08	55.06	63.7	65.74	69.58
Minor axis	10.74	18.02	21.02	24.65	28	29.07	30.56	32.25	36.35
Area	867.81	2023.86	2664.57	3515.79	4493.24	5028.42	6115.66	6660.55	7945.83
Fibonacci location ratio(area)		2.33	1.32		**1.68**				**1.76**
Fibonacci location ratio (Maj axis)		1.39	1.13		1.27				1.36
Fibonacci location ratio (Min axis)		1.68	1.32		1.33				1.29

The ratio of the changed cross-sectional area of the ram's horn is closed to the Fibonacci number, 1.618.

6.5 References

1. May PRA, Fuster JM, Haber J, Hirschman A. Woodpecker drilling behavior. An endorsement of the rotational theory of impact brain injury. Archives of neurology. 1979;36(6):370.

2. Backhouse F. Woodpeckers of North America: Firefly Books Ltd; 2005.

3. Bock WJ. Functional and evolutionary morphology of woodpeckers. Ostrich: Journal of African Ornithology. 1999;70(1):23-31.

4. Kirby VC. An adaptive modification in the ribs of woodpeckers and piculets (Picidae). The Auk. 1980:521-32.

5. Spring LW. Climbing and pecking adaptations in some North American woodpeckers. The Condor. 1965;67(6):457-88.

6.Wygnanski-Jaffe T, Murphy C, Smith C, Kubai M, Christopherson P, Ethier C, et al. Protective ocular mechanisms in woodpeckers. Eye. 2005;21(1):83-9.

7. Feughelman M. Mechanical properties and structure of alpha-keratin fibres: wool, human hair and related fibres: UNSW press; 1997.

8. Soons J, Herrel A, Genbrugge A, Adriaens D, Aerts P, Dirckx J. Multi-layered bird beaks: a finite-element approach towards the role of keratin in stress dissipation. Journal of the Royal Society Interface. 2012.

9. Wegst U, Ashby M. The mechanical efficiency of natural materials. Philosophical Magazine. 2004;84(21):2167-86.